ISSN:2661-4448(online)
2661-443X(print)
Volume 3 No.2 2021

MECHANICAL ENGINEERING SCIENCE

VISER
www.viserdata.com

COMPANY INTRODUCTION

Viser Technology Pte. Ltd. was founded in Singapore with branch offices in both Hebei and Chongqing, China. Viser focuses on publishing scientific and technological journals and books that promote the exchange of scientific and technological findings among the research community and around the globe. Despite being a young company, Viser is actively connecting with well-known universities, research institutes, and indexation database, and has already established a stable collaborative relationship with them. We also have a group of experienced editors and publishing experts who are dedicated to publishing high-quality journal and book contents. We offer the scholars various academic journals covering a variety of subjects and we are committed to reducing the hassles of scholarly publishing. To achieve this goal, we provide scholars with an all-in-one platform that offers solutions to every publishing process that a scholar needs to go through in order to show their latest finding to the world.

Mechanical Engineering Science

Publisher: Viser Technology Pte. Ltd.

ISSN: 2661-4448(online)

2661-443X(print)

Frequency: Semi-annual

Add.:21 Woodlands Close, #08-18

Primz Bizhub SINGAPORE (737854)

https://www.viserdata.com/

Mechanical Engineering Science

Volume 3 No.2 (2021)

CONTENTS

VISER

Message for the Special Issue of Advanced Supercritical CO_2 Power Cycles

Supercritical carbon dioxide (SCO_2) power cycles, which uses CO_2 as the working medium to realize thermal power conversion and output electric energy, was first proposed in the 1950s, but has not attracted widespread attention. At the beginning of this century, with the urgent need to reduce greenhouse gas emission and slow down the global warming trend, SCO_2 power generation started to attract extensive interest. Compared to traditional water steam Rankine cycles, the SCO_2 Brayton cycles have higher efficiency, more compact system to allow quick response to load variations, and better safety. Therefore, SCO_2 power generation has the potential to replace the traditional steam power generation technology, and is considered a transformative power generation technology.

SCO_2 cycle can adopt various types of energy including nuclear energy, solar energy, fossil fuel, and waste heat. Numerous experimental and computational studies have been carried out on the mechanism of thermal power conversion, heat transfer of SCO_2, and flow characteristics in the rotating machinery components. Progress has been made in theoretical innovation, equipment development, and system integration. In recent years, SCO_2 power generation technology gradually starts to be developed and tested in the 10 MW scale. However, efforts are still needed to further advance this technology. For examples, for SCO_2 cycle driven by different heat sources, the principle methods for system design and analysis are needed under different working conditions and transient operation; extensive investigations need to be carried out to improve the design accuracy of key components such as intermediate heat exchanger, regenerator and turbine machinery.

In order to report the recent progress made by researchers in the topic of advanced SCO_2 power cycles, this special issue on Mechanical Engineering Science is organized. We are very honored to be invited as the guest editors for this special issue. We have received strong support from leading scientists in universities and research institutes. This special issue contains a total of 6 publications, covering performance analysis and optimization design of the key components in SCO_2 cycles such as coal-fired boilers, turbines, compressors, and heat exchangers.

We would like to express our heartfelt gratitude to the authors for their strong support for this special issue, to the reviewers for their hard work, and to the editorial group of Mechanical Engineering Science for their tremendous efforts.

Jinliang Xu, Qingyang Wang

Planner Author

Jinliang Xu is a professor in the School of Energy Power and Mechanical Engineering, North China Electric Power University. He is the founder and director of Beijing Key Laboratory of Multiphase Flow and Heat Transfer for Low Grade Energy Utilization. His research interests include multiphase flow and heat transfer in micro/nano systems, advanced power generation system, and low-grade energy and renewable energy utilization. He has published more than 200 journal papers and co-authored two books. He is the editor of Energies, Thermal Science and Engineering Progress, Frontiers in Heat pipe, and Alternative Energy. He was the guest editor for the special issues of Applied Thermal Engineering and Energy. He received the Natural Science Award of the Ministry of Education, China (first grade). He is a recipient of the National Science Fund for Distinguished Young Scholars in 2008, has been the "973" project chief scientist, Ministry of Science since 2011, and is awarded the "Yangtze River Scholar" Professor by the Ministry of Education in 2013.

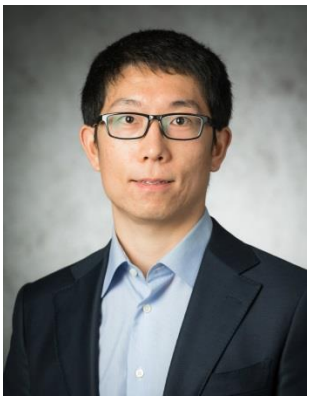

Qingyang Wang joined the School of Energy Power and Mechanical Engineering, North China Electric Power University in 2020 as an associate professor. He received his PhD in mechanical engineering from University of California, San Diego in 2020 and his B.S. in thermal engineering from Tsinghua University in 2015. He has received the 2021 Beijing Rising Star in Science and Technology Award, 2019 Chinese Government Award for Outstanding Self-Financed Students Abroad, the ASME 2019 IMECE Society-Wide Micro/Nano Technology Forum Best Poster Oral Presentation Award, and the IEEE ITHERM 2018 Outstanding Poster Award. His research interests include phase change heat transfer using micro/nanostructures, advanced materials for thermal transport, and supercritical heat transfer.

About the author

Xiaokai Liu (1998—), male, master student, research direction is supercritical fluid flow heat transfer performance and high-efficiency compact heat exchanger.

Wen-Li Ye (1998.5—) Man, Master,Main research work is optimization of boiler tail flue in supercritical carbon dioxide power generation system.

Lehao Hu is a Ph.D. candidate at Shaanxi Engineering Laboratory of Turbomachinery and Power Equipment, Institute of Turbomachinery, Xi'an Jiaotong University, China, under the supervision of Associate Prof. Qinghua Deng. His research topic is focused on the aerothermodynamic of turbomachinery, especially the optimization design of supercritical CO_2 turbine.

About the author

Yueming Yang (1997.10—) Male, Master degree candidate, Educational Experience: 2016—2020: Shandong University of Science and Technology / College of Mechanical and Electronic Engineering / Bachelor's Degree in Engineering, 2020- -now: Shandong University / School of Energy and Power Engineering / Master's Degree in Engineering, Yueming Yang research interests are the design and optimization of supercritical CO_2 radial inflow turbines; turbomachinery (axial and radial) for energy conversion and propulsion; modeling of fluid- and thermo- dynamic systems (mainly the SCO_2 Brayton cycles); and physical properties of working fluid in circulation system (mainly the SCO_2 power cycles).

Guihua Tang is a full Professor in the Department of Thermo-Fluid Science and Engineering, School of Energy and Power Engineering at Xi'an Jiaotong University, China. He received his Ph.D. in Engineering Thermo-physics from Xi'an Jiaotong University in 2004. He worked as the Higher Scientific Officer in STFC Daresbury Laboratory, UK from April 2007 to August 2009. His research interests include the micro/nanoscale heat and mass transfer, photo-thermo-electric coordinated conversion, and thermal design and management. He is the recipient of National Talent Plan, and co-recipient of National Science and Technology Awards and National Teaching Award.

Peipei Wang, male, born in 1994, graduate student of Anhui University of Technology. The research area is focused on the clean combustion of pulverized coal and the control of pollutants.

Viser Technology Pte. Ltd.
Mechanical Engineering Science
DOI: 10.33142/mes.v3i2.6726

Research Article Open Access

Numerical Investigation on Flow and Heat Transfer Performance of Supercritical Carbon Dioxide Based on Variable Turbulent Prandtlnumber Model

Xiaokai LIU[1,2,3], Haiyan ZHANG[1,2], Keyong CHENG[1,2,3*],Xiulan HUAI[1,2,3*], Haiyan LIAO[4],Zhongmei ZHANG[4]

1. Institute of Engineering Thermophysics, Chinese Academy of Sciences, Beijing 100190, China
2. University of Chinese Academy of Sciences, Beijing 100049, China
3. Nanjing Institute of Future Energy System, Nanjing 210000, China
4. CHN Energy New Energy Technology Research Institute CO., LTD., Beijing 102206, China

***Corresponding Author:** Keyong CHENG, E-mail: chengkeyong@iet.cn, Xiulan HUAi, hxl@iet.cn*

Abstract:
Flow and heat transfer characteristic of supercritical carbon dioxide (SCO_2) are numerically investigated in the horizontal and vertical tubes. TWL turbulent Prandtl number model could well describe the behavior of SCO_2 affected by the buoyancy. Under the cooling condition, the heat transfer performance of SCO_2 along the upward direction is best and that along the downward direction is worst when bulk fluid temperatures are below the pseudocritical temperature. Reducing the ratio of heat flux to mass flux could decrease the difference of convective heat transfer coefficient in three flow directions. Under the heating condition, heat transfer deterioration only occurs in vertical upward and horizontal flow directions. Heat transfer deterioration of SCO_2 could be delayed by increasing the mass flux and the deterioration degree is weakened in the second half of tube along the vertical upward flow direction. Compared with the straight tube, the corrugated tube shows better comprehensive thermal performance.
***Keywords:** Supercritical carbon dioxide; Turbulent Prandtl number; Flow and heat transfer; Field synergy principle; Numerical investigation*

Table 1 Nomenclature

c_p	Specific heat at constant pressure, J/(kg Ƙ)
d	Diameter, mm
g	Gravity, m/s^2
G	Mass flux, kg/(m s)
h	Heat transfer coefficient, kw/(m Ƙ)
P	Pressure, mpa
q	Heat flux, kw/m
Re	Reynolds number
T	Temperature, K
T_{pc}	Pseudocritical temperature, K
v	Velocity, m/s
Greek	
λ	Thermal conductivity, W/(m Ƙ)
μ	Dynamic viscosity, Pa s
ρ	Density, kg/m^3
τ	Shear stress, Pa
ϕ	Energy dissipation, W/m^3
Subscripts	
ave	Average
b	Bulk
i, j, k	Tensor index symbols
w	Wall

1 Introduction

Carbon dioxide (CO_2) is widely used in advanced energy power systems due to its excellent characteristics of wide sources, non-toxic and environmental protection.Since the supercritical CO_2 (SCO_2) Brayton cycle system can significantly reduce system size, improve system efficiency and decrease investment cost, the SCO_2 power generation technology has attracted wide attentions [1-3]. Under supercritical pressure, the thermophysical properties of SCO_2 are changed dramatically around the pseudocritical point (the peak point of specific heat at constant pressure corresponds to the pseudocritical temperature (T_{pc}), which is called pseudocritical point.), which wouldinduce the various heat transferbehavior. Therefore, it is very important to further explore flow and heat transfer behaviors of SCO_2 under supercritical pressure.

In recent years, many researchers have studied flow and heat transfer characteristics of SCO_2 by numerical and experimental methods. Liu et al. [4] studied the Nusselt number and pressure loss of SCO_2 in a large diameter tube through the experiments, and they

Received on October 17, 2021; Accepted on December 12, 2021

summarized the empirical correlation. Jiang et al. [5] conducted experiment study on the effects of flow direction, heat flux and buoyancy effect. Xu et al. [6] studied the thermal performance of SCO_2 in serpentine tubes. The buoyancy and centrifugal force in different flow directions were investigated. Zhu et al. [7] obtained the criterion of heat transfer deterioration by experiments. Liu et al. [8] introduced the influence of buoyancy effectand centrifugal force on SCO_2 in helical tubes.

Due to only limited temperature data can be obtained from the experiment, the flow field in the tube cannot be analyzed in detail. To understand the heat transfer mechanism of SCO_2, numerical methods have been widely used.Liu et al. [9-10] numerically studied the effects of pipe cross-section shapes and diameters on SCO_2. They found that the pipe shape and pipe diameter have great influence on the secondary flow strength of SCO_2. The performance of SCO_2 in straight and helical tubes is compared by Liu et al. [11]. They stated that the centrifugal force could make the heat transfer capacity of the spiral tube stronger than that of the straight tube, but the centrifugal force in thepseudocriticalregion can cause more serious deterioration. Eze et al. [12] found that the heat transfer deterioration of SCO_2 could be effectively reduced by adding spoilers in the pipe. The effects of heat and mass flux on the comprehensive mechanism of SCO_2 are explored by Yan et al [13].

In this study, flow and heat transfer of SCO_2 in straight and corrugated tubes are presented. During the simulations, different mass flux, heat flux, and flow direction are analyzed and discussed. This research may be helpful for the understanding of SCO_2 heat transfer.

2 Numerical Model

2.1 Physical model and simulation conditions

The physical models of straight and corrugated tubes are established in the present work and the orthographic view of the geometry model isshown in Figure 1. The heated length of two tubes is set to 900 mm. The tube diameter is 6 mm, and the adiabatic sections are arranged at the inlet and outlet of the tube respectively. The inlet pressure is fixed to 8 MPa.

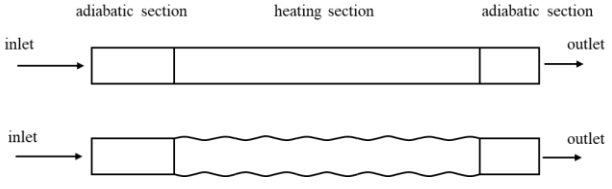

Figure 1 Physical model and simulation conditions

2.2 Governing equations

The software ANSYS FLUENT 19.2 is employed for the calculations. The steady-state equations are listed in Eqt. (1)-(3):

Continuity equation:

$$\frac{\partial(\rho u_j)}{\partial x_j}=0 \tag{1}$$

Momentum equation:

$$\frac{\partial(\rho u_i u_j)}{\partial x_j}=-\frac{\partial P_i}{\partial x_j}+\rho g_i+\frac{\partial}{\partial x_j}\left[(\mu+\mu_t)(\frac{\partial u_i}{\partial x_j}+\frac{\partial u_i}{\partial x_j}-\frac{2}{3}\frac{\partial u_k}{\partial x_k})\right] \tag{2}$$

Energy equation:

$$\frac{\partial(\rho u_j c_p T)}{\partial x_j}=\frac{\partial}{\partial x_j}(\lambda\frac{\partial T}{\partial x_j})+\phi \tag{3}$$

The Shear Stress Transport (SST) model is employed in the present work, which has been proved accurately to calculate the heat transfer behavior of SCO_2 [14-15]. The equations of the turbulence kinetic energy k and the specific dissipation rate ω are listed in Eqt. (4) and (5), respectively:

$$\frac{\partial(\rho k)}{\partial t}+\frac{\partial(\rho k u_i)}{\partial x_i}=-\frac{\partial}{\partial x_j}(\Gamma_k\frac{\partial k}{\partial x_j})+G_k-Y_k+S_k \tag{4}$$

$$\frac{\partial(\rho \omega)}{\partial t}+\frac{\partial(\rho \omega u_i)}{\partial x_i}=-\frac{\partial}{\partial x_j}(\Gamma_\omega\frac{\partial \omega}{\partial x_j})+G_\omega-Y_\omega+S_\omega \tag{5}$$

2.3 Turbulent Prandtl number model

The Pr_t is set to 0.85 or 0.9, which is obtained at atmospheric pressure and it is not applicable to supercritical fluids with severe physical changes. Li et al. [16] claimed that the turbulent kinetic energy of the buffer layer decreased for the deterioration and the appropriate Pr_t model is crucial to describe the heat transfer characteristics of SCO_2.

In 1993, Kays and Crawford [17] launched the KC model of turbulent Prandtl number as shown in Eqt. 6.

$$Pr_t=\begin{cases}1.07, & y^+\le 5\\ \dfrac{1}{0.5882+0.228\dfrac{\mu_t}{\mu}-0.0441\left(\dfrac{\mu_t}{\mu}\right)^2\left[1-exp\left(-\dfrac{5.165}{\mu_t/\mu}\right)\right]}, & y^+>5\end{cases} \tag{6}$$

Kays proposed the K model in 1994, and this turbulent Prandtl number model agrees well with the experiment of Buhret al [18].

$$Pr_t=\begin{cases}1.07, & y^+\le 5\\ 0.85+\dfrac{2}{Pe_t}, & y^+>5\end{cases} \tag{7}$$

Where $Pe_t=\mu_t/\mu$ Pr.

For the flow of SCO_2 under high Reynolds number conditions, the turbulence is a key parameter. Therefore, Pr_t tends to be constant. In the viscous bottom, the Pr_t effect is limited due to the leading role of the molecular heat conduction. However, u and u_t are in the same magnitude orderfor the transition region. Tang et al.[19] proposed TWL model of turbulent Prandtl number as shown in Equation 8.

$$Pr_t=\begin{cases}1.0, & \mu_t/\mu<0.2\\ 0.85+\dfrac{Pr}{15}, & 0.2\le\mu_t/\mu\le 10\\ Pr=10, & \mu_t/\mu>10\end{cases} \tag{8}$$

2.4 Grid number independence and model validation

Considering the influence of grid number on the calculation results, four groups of grid numbers generated by ANSYS ICEM 19.2 are selected for grid independent verification. The grid numbers and calculation results are shown in Table 2. The maximum relative error of the h between Case 3 and Case 4 is only about 2.8%. Take into account both calculation accuracy and cost, grid number in Case 3 is selected for the calculation in following calculations.

Table 2 The grid number independence test

Case	Grid number	h (kW/(m^2 K))	Relative error
1	695656	1.077	9.7%
2	1226960	1.019	3.8%
3	1576248	1.009	2.8%
4	2113160	0.982	-

The reliability of simulation is further verified by establishing the same physical modeland setting the same boundary conditionsin Ref. [20]. Three Pr_t models introduced in section 2.3 are selected for numerical calculation, and the corresponding wall temperature distribution is presented in Figure 2. The maximum relative error of T_w between simulation and experiment is about 4 %, which illustrates that the SST turbulence model and TWL Prandtl number model is accurate and credible to simulate flow and heat transfer of SCO_2.

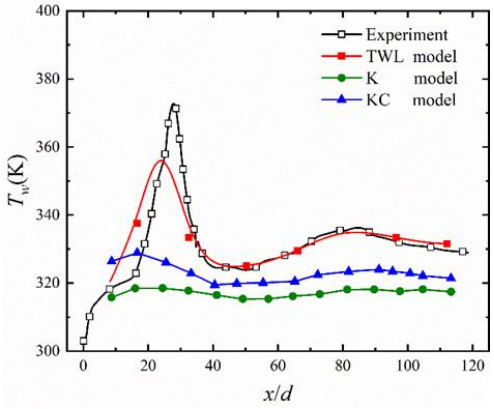

Figure 2 Comparison of turbulent Prandtl numbermodels under experiment conditions

3 Results and Dcussion

3.1 Cooling conditions in straight tubes

Figure 3 shows that for the cooling conditions the effect of the heat flux to mass flux ratio q/G on the wall temperature of the tube T_w. It can be found that the T_w decreases with the decrease of T_b. When the G is fixed, the T_w decreases with the enlargement of q, and the T_w increases with the raise of G When the q is fixed. Therefore, the T_w decreases with the increase of q/G, and the range of fluid temperatures increases with the enlargement of q/G. At G =200 kg/(m^2 s), when the fluid bulk temperature is slightly higher than the pseudocritical temperature (307.8 K at 8 MPa), it can be found that $T_{w\ upward} > T_{w\ horizon} > T_{w\ downward}$. In the region where theT_b islarger than T_{pc}, the distribution of T_w tends to be consistent in horizontal, vertical upward and vertical downward directions. There is almost no difference in the distributionsof T_w with three flow directions when the mass flux is 500 kg/(m^2 s).

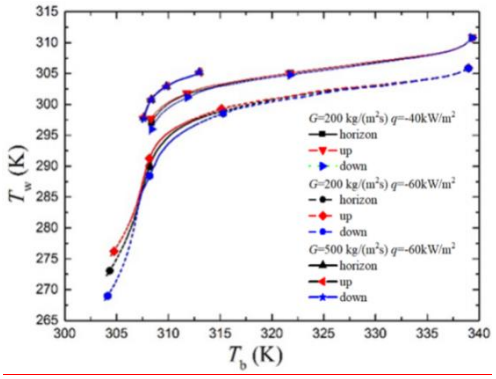

Figure 3 Variation of wall temperature with fluid temperature

The influence of buoyancy is considered because of the drastic changes of the density of SCO_2. The buoyancy factor Gr/Re^2 is employed to describe buoyancy effects in the horizontal flow direction and the expression of Grashof number Gr is shown in equation 9. Generally, the natural convection induced by buoyancy remarkably affects the thermal-hydraulic characteristics for $Gr/Re^2 > 0.001$. The effect of natural and forced convection on heat transfer isnecessaryto be considered simultaneously for $0.1 < Gr/Re^2 < 10$. When $Gr/Re^2 > 10$, compared with natural convection, forced convection can be ignored. The buoyancy factor $Gr/Re^{2.7}$ is adopted to characterize the buoyancy effect of the vertical upward and downward flow. It is generally accepted that the influence of the buoyancy force cannot be ignored for $Gr/Re^{2.7} > 10^{-5}$.

$$Gr^* = \frac{g\beta q d^4}{\lambda_b \nu_b^2} \tag{9}$$

Where β is the fluid volume expansion coefficient.

The variations of h and Gr/Re^2 with T_b are shown in Figure 4 (a) and (b). The *h* under various conditions first increases and then decreases, and there is a peak at slightly higher temperature than the pseudocritical point. With the increase of the q, the h is enhanced in the region where T_b is much higher than T_{pc}, butthere is no effect of the peak value of h. As the T_b decreases to the T_{pc}, it can be seen that $h_{upward} > h_{horizon} > h_{downward}$, but when the mass flow rate is 500 kg/(m^2 s), the heat transfer coefficients for the three flow directions are almost the same, which are consistent with the distribution of T_w presented in Figure3.

With the increase of *q/G*, the buoyancy effect is increased at three flow directions, and the effect of buoyancy could be basically ignored when the mass flux is 500 kg/(m^2 s). When the mass flux is 200 kg/(m^2 s), the

buoyancy factor gradually increases with the cooling of the SCO_2, and rapidly increases to the peak near the pseudocritical point which indicates that the buoyancy near the pseudocritical region is strong under the cooling condition. The buoyancy factor of the vertical downward flow is larger compared with upward flow. Combined with the results that $h_{upward} > h_{downward}$ from Figure 4 (a), it can be concluded that under the same q/G cooling condition, compared with the vertical downward flow, the vertical upward flow has less buoyancy effect and presents better thermal performance.

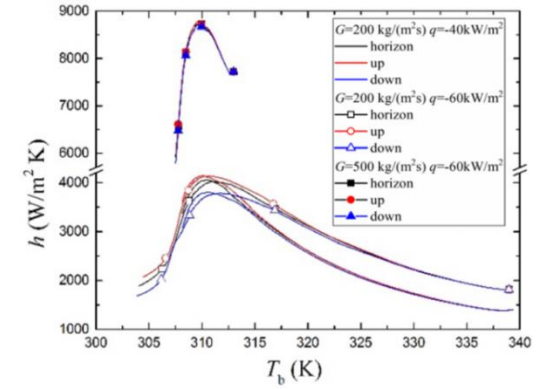

(a) h

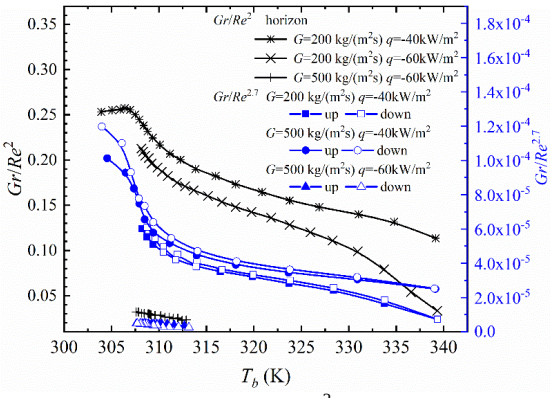

(b) Gr/Re^2

Figure 4 Variation of (a) local heat transfer coefficient and (b) buoyancy factor with fluid temperature.

3.2 Heating conditions in straight tubes

Figure 5 demonstrates the variations of the T_w with the T_b along the horizontal and vertical flow directions. For a horizontal flow, when the mass flux is set to 500 kg/(m^2 s), T_w increases monotonically. There are wall temperature peaks when the mass flux is set to 200 kg/(m^2 s). It is seen that there are wall temperature peaks in upward flow direction under the three conditions in Figure 5(b), and when q is fixed, the peak of T_w becomes more obvious with the increases of q. When q/G is small, the peak value of T_w also appears, and the wall temperature variation trendis different from the other two heating conditions, and this phenomenon will be further discussed in the subsequent work. The wall temperature monotonically increases, and there is no obvious peak at the vertical downward flow direction shown in Figure 5(c).

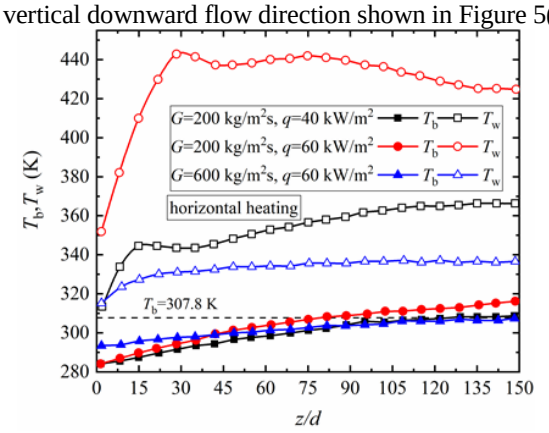

(a) Horizontal

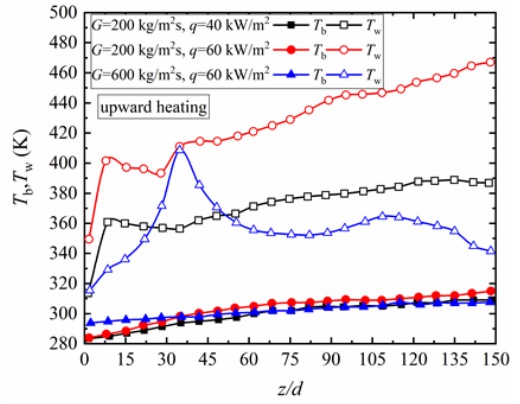

(b) Vertical upward

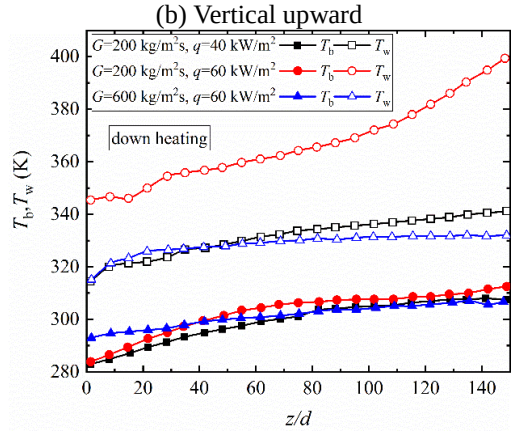

(c) Vertical downward

Figure 5 Variations of T_w with T_b under heating conditions: (a) horizontal (b) vertical upward

The variations of h with the T_b at horizontal and vertical flow directions are presented in Figure 6. Figure 6(a) and (c) show that h increases as G grows at the same heat flux, and h decreases as q increases when G is fixed. h shows a decreasing trend from the initial region of the heating section, which is due to T_w increases rapidly along the heating process, resulting in the rapid increase of the temperature difference between the fluid and the wall. Different from the horizontal and vertical downward flow, Figure 6(b) demonstrates that h appears a valley near the region of z = 35 d when the mass flux is 500 kg/(m^2 s), which means the heat transfer is deteriorated, this phenomenon corresponds to the peak of wall

temperature at about z = 35 d. In summary, the enlargement of the qinduces the rapid increase of T_w, resulting in the decrease of h under small mass flux condition. When q is 60 kW/m^2, heat transfer deterioration occurs at mass flux of 200 and 500 kg/(m^2 s), but the increase of G delays the occurrence of heat transfer deterioration and attenuates the degree of deterioration in the second half of heating tube. Thus, it is meaningful to explore the onset and mechanism of heat transfer deterioration under upward flow heating conditions.

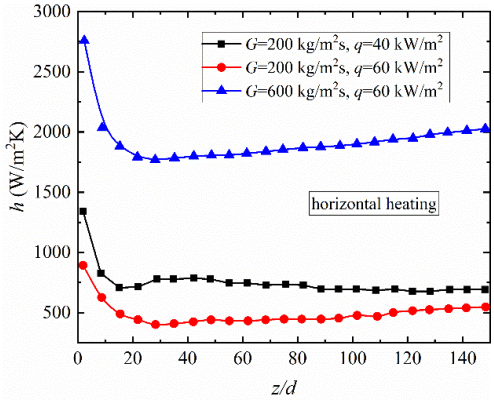

(a) Horizontal

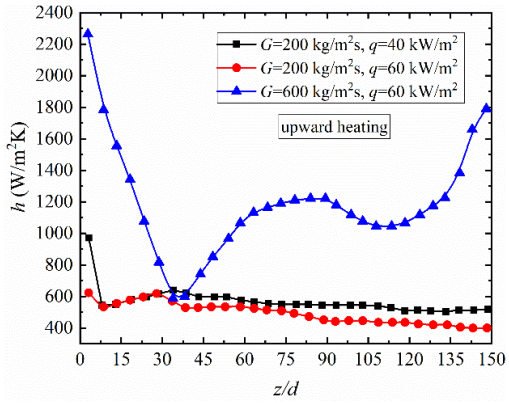

(b) Vertical upward

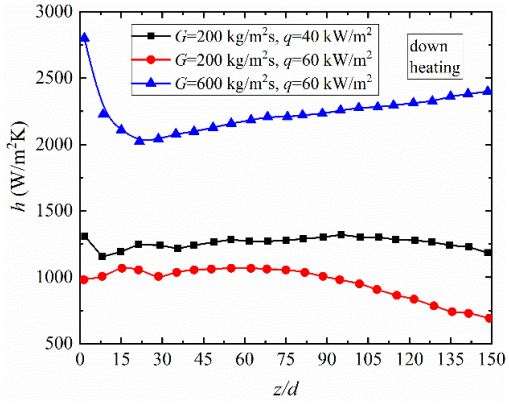

(c) Vertical downward

Figure 6 Variations of h with T_b under heating conditions: (a) horizontal (b) vertical upward (c) vertical downward

The relations of buoyancy factor with the bulk fluid temperature at different flow directions are demonstrated in Figure 7. Figure 7(a) illustrates Gr/Re^2 generally decreases as the T_b increases, and the influence of buoyancy on horizontal flow is the smallest at G = 500 kg/(m^2 s). It is seen that the buoyancy effect of the vertical upward flow is greater than that of the vertical downward flow.

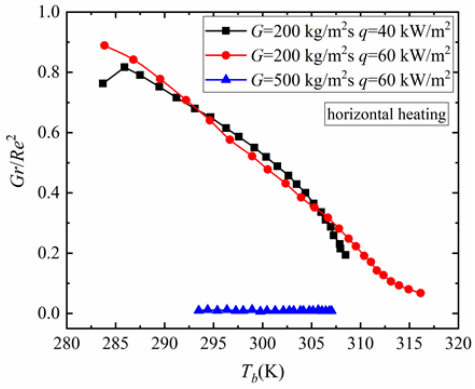

(a) Horizontal

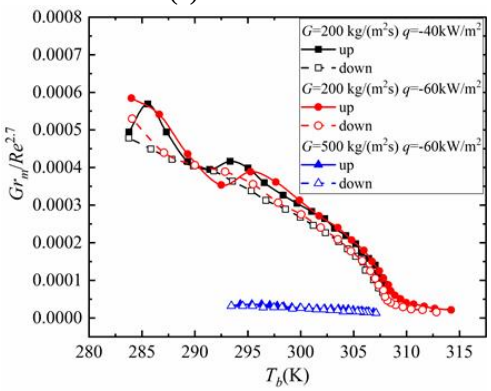

(b) Vertical up / down

Figure 7 Variations of buoyancy factor with T_b under heating conditions: (a) horizontal (b) vertical up/down.

3.3 Corrugated tubes

The distribution of the T_b and the T_w in corrugated and straight tubes along the horizontal direction is presented in Figure 8. T_b in corrugated and straight tubes is basically the same with the same q and G. However, the wall temperature in corrugated tube fluctuates along the flow direction and T_w is generally higher than that in the straight pipe.

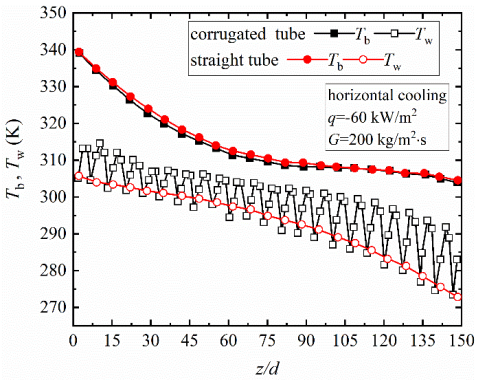

Figure 8 Distribution of bulk fluid temperature T_b and wall temperature T_w in corrugated and straight tubes

The distributions of h and the local evaluation factor $j/f^{1/3}$ in corrugated and straight tubes are provided in Figure. 9. h of a corrugated tube is significantly higher than that of a straight tube. Considering that the corrugated tube usually increases the pressure drop remarkably while enhancing the heat transfer, the evaluation factor $j/f^{1/3}$ is adopted to assess the comprehensive property of the straight and corrugated tubes. It could be concluded that the comprehensive thermal performance of SCO_2 in a corrugated tube is better than that in a straight tube from Figure. 9(b).

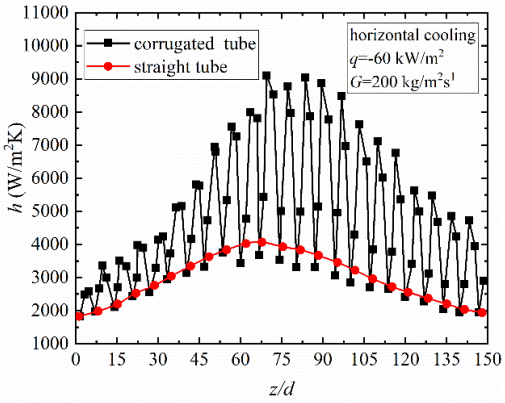

(a) Local heat transfer coefficient

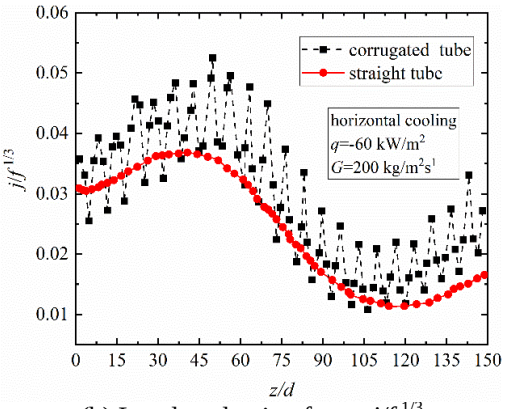

(b) Local evaluation factor $j/f^{1/3}$

Figure 9 Distributions of local heat transfer coefficienth and local evaluation factor $j/f^{1/3}$ in corrugated and straight tubes

Figure 10 and 11 illustrate the distributions of the secondary flow and field synergy angle β on different locations of the corrugated and straight tube under the horizontal cooling condition. The secondary flow in the straight pipe is uniformly distributed, and the left and right vortexes are vertically axisymmetric. The velocity of the secondary flow in the corrugated tube is larger than that in the straight tube, and the distribution of the secondary flow is non-uniform. There are multiple asymmetrically distributed vortices and the location of the vortices is complex and variable at different cross sections. In the straight tube, the smaller β is mainly concentrated in the upper of the cross section, but the overall β is almost 90°. In the corrugated tube, the distribution of the field synergy angle on the cross section is non-uniform, and the overall β is smaller than that in the straight tube. According to the field synergy theory, due to the high intensity and uneven distribution of the secondary flow, the fluid in the corrugated tube is more fully mixed, which enhances the synergy between the local fluid velocity and temperature gradient.

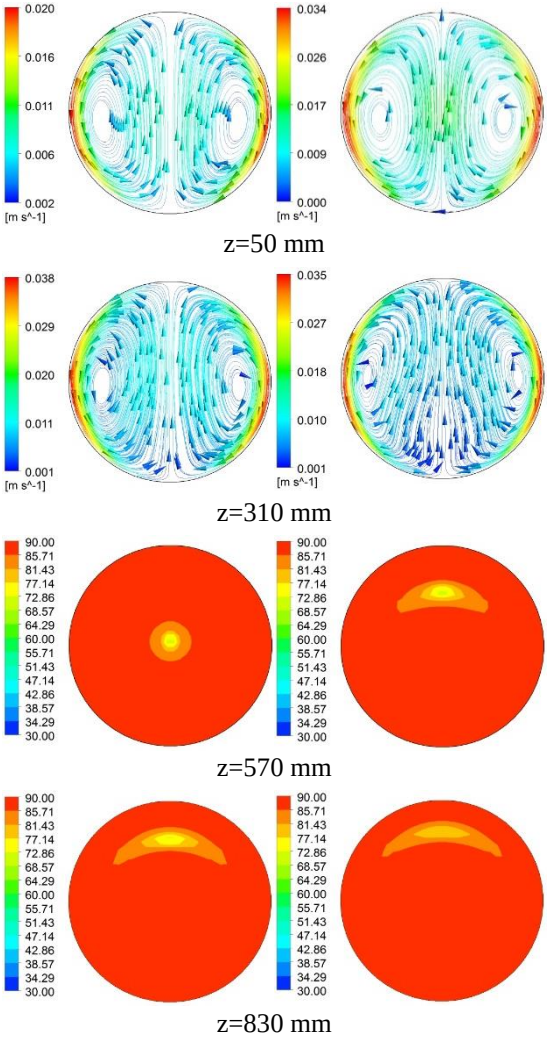

Figure 10 Field synergy angle distribution of the secondary flow and field on the local section of the straight tube

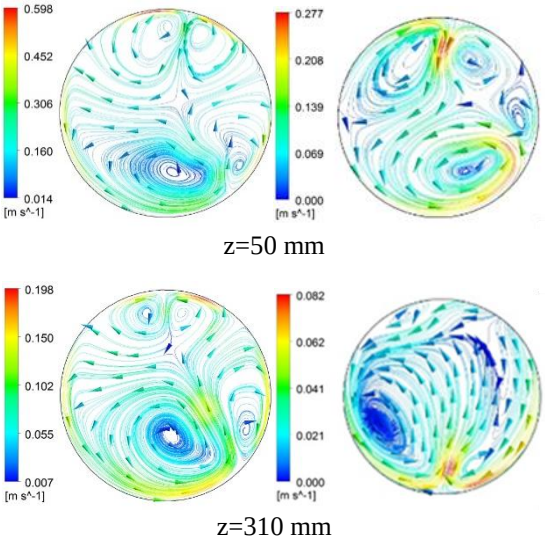

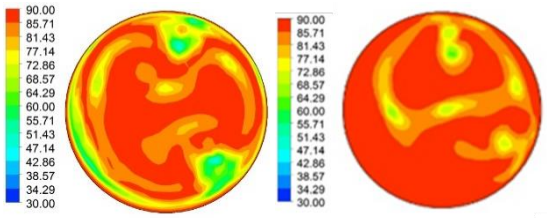

z=570 mm

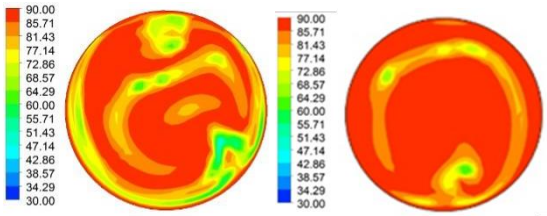

z=830 mm

Figure 11 Field synergy angle distribution of the secondary flow and field on the local section of the corrugated tube

4 Conclusions

The flow and heat transfer characteristics of SCO_2 in straightand corrugated tubesare numerically studied. The effects of mass flux, heat flux, flow direction and buoyancy on the heat transfer performance of SCO_2 are analyzed and discussed. The conclusions are listed as follows:

The selected SST k-ω turbulence model and differentturbulence Prandtl number models could reproduce the difference of the wall temperature distribution caused by buoyancy in the experiment, but the TWL Prandtl number model has the best consistency with the experiment data, which could more accurately describe the effect of buoyancy. It is suggested that this model be applied to numerical simulation of thermal-hydraulic characteristics of SCO_2.

Under the cooling condition in the straight tube, the T_w monotonically decreases along the flow direction, and there is no peak of T_w the in the vertical upward, vertical downward and horizontal flow directions. The h peaked near the pseudocritical point. The buoyancy factor in the vertical downward flow is larger than that in the upward flow at the vicinity of pseudocritical point under the cooling condition. As the fluid temperature decreases to less than the pseudocritical temperature, $h_{upward} > h_{horizon} > h_{downward}$. But, when q/G is small, there is almost no difference on h for the three flow directions.

Under the heating condition in the straight tube, the peak of the T_w only appears in the conditions of the upward and horizontal flow, and there is no wall temperature peak in the vertical downward flow. The increase of the q leads to the rapid enlargement of the T_w, resulting in the decrease of the h with the same G in the vertical upward flow. When the q is fixed, the increase of the G delays the occurrence of heat transfer deterioration and attenuates the deterioration degree in the vertical upward flow direction.

The comprehensive performance of SCO_2 in the corrugated tube is better than that in the straight tube. Compared with the straight tube, the stronger secondary flow of the corrugated tube enhances the synergy between local velocity and temperature gradient, thus the heat transfer of SCO_2 in the corrugated tube is enhanced.

References

[1] Jiang P X, Zhang F Z, Xu R N. Thermodynamic analysis of a solar-enhanced geothermal hybrid power plant using CO_2 as working fluid. Applied Thermal Engineering, 2017, 116, 463-472.

[2] Luu M T, Milani D, McNaughton R, Abbas A. Analysis for flexible operation of supercritical CO_2 Brayton cycle integrated with solar thermal systems. Energy, 2017, 124, 752-771.

[3] Cheng K Y, Zhou J Z, Huai X L, et al. Experimental exergy analysis of a printed circuit heat exchanger for supercritical carbon dioxide Brayton cycles. Applied Thermal Engineering, 2021, 192, 116882.

[4] Liu Z B, He Y L, Yang Y F, et al. Experimental study on heat transfer and pressure drop of supercritical CO_2 cooled in a large tube. Applied Thermal Engineering, 2014, 70(1): 307-315.

[5] Jiang P X, Zhang Y, Shi R F. Experimental and numerical investigation of convection heat transfer of CO_2 at supercritical pressures in a vertical mini-tube. International Journal of Heat and Mass Transfer, 2008, 51(11-12): 3052-3056.

[6] Xu R N, Luo F, Jiang P X. Experimental research on the turbulent convection heat transfer of supercritical pressure CO_2 in a serpentine vertical mini tube. International Journal of Heat and Mass Transfer, 2015, 91:552-561.

[7] Zhu B G, Xu L, Wu X M, et al. Supercritical "boiling" number, a new parameter to distinguish two regimes of carbon dioxide heat transfer in tubes. International Journal of Thermal Sciences, 2019, 136:254-266.

[8] Liu X X, Xu X X, Jiao Y Z, et al. Flow structure with mixed turbulent flow of supercritical CO_2 heated in helically coiled tube. Applied Thermal Engineering, 2021, 189, 116684.

[9] Liu Z B, He Y L, Wang K, et al. Effect of cross section shape of solar collector tube on supercritical CO_2 flow and heat transfer in tube. Journal of Engineering Thermophysics, 2018, 39(10): 2235-2243

[10] Liu Z B, Fei J Y, Yang Y F, et al. Effect of pipe diameter on flow and heat transfer in supercritical CO_2 pipe. Journal of Engineering Thermophysics, 2016, 37(2): 357-360.

[11] Liu X X, Shan H, Zhang S J, et al. Comparative study on heat transfer characteristics of supercritical CO_2 in vertical straight tube and spiral tube. Journal of Engineering Thermophysics, 2020, 41(1): 55-60.

[12] Chika E, Shahid A K, Kwun T L, et al. Numerical study on the heat transfer deterioration and its mitigations for supercritical CO_2 flowing in a horizontal miniature tube. Annals of Nuclear Energy, 2021, 151, 107982.

[13] Yan C S, Xu J L. Numerical analysis of flow and heat transfer

of supercritical pressure CO_2 in horizontal circular tube. Journal of Physics, 2020, 69(4)：044401.

[14] Wen Q L, Gu H Y. Numerical simulation of heat transfer deterioration phenomenon in supercritical water through vertical tube.Annals of Nuclear Energy, 2010, 37(10):1272-1280.

[15] Liu L, Xiao Z, Yan Z, et al. Heat transfer deterioration to supercritical water in circular tube and annular channel. Nuclear Engineering and Design, 2013, 255, 97-104.

[16] Li Z, Wu Y, Tang G, et al. Comparison between heat transfer to supercritical water in a smooth tube and in an internally ribbed tube. International Journal of Heat and Mass Transfer, 2015, 84:529-541.

[17]Kays W M, Crawford M E, Convective Heat and Mass Transfer, McGraw-Hill Inc., New York, 1993.

[18]Kays W M. Turbulent Prandtl number. Asme Transactions Journal of Heat Transfer, 1994, 116(2):284-295.

[19]Tang G, Shi H, Wu Y, et al. A variable turbulent Prandtl number model for simulating supercritical pressure CO_2 heat transfer. International Journal of Heat and Mass Transfer, 2016, 102:1082-1092.

[20] Weinberg R S, Experimental and Theoretical Study of Buoyancy Effects in Forced Convection to Supercritical Pressure Carbon Dioxide, University of Manchester, 1972.

Viser Technology Pte. Ltd.
Mechanical Engineering Science
DOI: 10.33142/mes.v3i2.6723

Research Article Open Access

Design Optimization of Boiler Tail Flue in Supercritical Carbon Dioxide Power Generation System

Wenli YE[1], Jinliang XU[1,2], Guanglin LIU[1,2,*]

1 Beijing Key Laboratory of Multiphase Flow and Heat Transfer for Low Grade Energy Utilization, North China Electric Power University, Beijing, China
2 Key Laboratory of Power Station Energy Transfer Conversion and System, North China Electric Power University, Ministry of Education, Beijing, China

***Corresponding Author:** Dr. Guanglin LIU, No. 2 Beinong Road, Beijing 102206, China; email address: liu0513@126.com*

Abstract:
The S-CO_2 top-bottom combined cycle based on overlap energy utilization can lead to excessive heating area, due to the small temperature difference and the large thermal load for the heating surface at the tail of the boiler. Therefore, reasonable optimization indexes are needed for design optimization. Common optimization indexes include heating area and working medium pressure drop, but lower working medium pressure drop usually leads to large heating area, for example, with the increase of tube inner diameter or boiler width, the pressure drop decreases but the heating area increases. Thus, if both are used as optimization indexes, it will be difficult to choose the optimum tube inner diameter and boiler width. In this paper, exergy loss analysis is used, in combination with economic analysis, the optimization index is unified to the cost per unit heat transfer of the heating surface. The thermal calculation and pressure drop calculation models are established for the heating surface at the tail of the boiler. The optimized heating surface can greatly improve the economic benefit.

***Keywords:** S-CO_2 cycle; calculation model; exergy loss analysis; optimization of the boiler*

1 Introduction

In supercritical carbon dioxide power generation system, the working medium in the cycle is CO_2 in supercritical state, and the cycle is called S-CO_2 cycle. The advantage of S-CO_2 cycle is high thermal efficiency and compact system. With the need to reduce carbon emission, the electric power grid needs to adapt the renewable energy generated power such as wind and solar energy. Due to the unstable nature of wind and solar energy, the fossil fuel power generation systems need to respond quickly to the load variation to avoid wasting of wind or solar energy. The S-CO_2 coal-fired power generation system has fewer components and more compact system, which provides possibility for rapid load variation. Therefore, S-CO_2 cycles are more advantageous than steam Rankine cycles [1].

Efforts have been made to study the boilers in S-CO_2 power cycles. Bai et al. [2] carried out the conceptual design of the boiler in a 300 MW coal-fired power plant with single reheat recompression S-CO_2 Brayton cycle. To utilize the waste heat of flue gas at the tail of boiler, split heater is used. Zhou et al. [3] put forward the calculation method for coal-fired boiler for S-CO_2 cycle, and used this calculation method to optimize the design and calculation of 1000 MW S-CO_2 coal-fired system with main parameters of 30.70 MPa and 606 ℃. The calculation shows that in terms of boiler heat transfer, part of the radiative heat transfer of S-CO_2 boiler becomes convective heat transfer. To solve the problems of large pressure drop of working medium and low temperature of reheating working medium under partial load conditions, Tong et al. [4] proposed a new layout scheme of heating surface of a 300 MW S-CO_2 coal-fired boiler, and studied its performance under load variation. The new S-CO_2 boiler is a single boiler with double tangential circle arrangement without central wall, which increases the proportion of reheat radiant heating surface.

Due to the small specific enthalpy increase of CO_2 in boiler, the mass flow rate of working medium in S-CO_2 boiler is 8 times that of steam Rankine cycle system, which causes larger pressure drop. Xu et al. [5] proposed the partial flow strategy for pressure drop reduction of boiler, and carried out modular design of the boiler heating surface. The working fluid is divided into two steams before entering the boiler and flows through different heating surfaces. Compared to the traditional water steam system, in the partial flow mode, the heating surface of the boiler tail is significantly different, and the inlet temperature and heat transfer characteristics of S-CO_2 in partial flow mode are also different. Because the inlet temperature of CO_2 is high, the temperature

Received on October 20, 2021; Accepted on December 10, 2021

difference between flue gas and working medium is small, which will result in a large heating surface area. Therefore, it is necessary to optimize the design of the heating surface in tail flue of the boiler. The objectives of the optimization is to reduce the area of the heating surface as much as possible and to ensure that the pressure drop of boiler working medium and flue gas is within a reasonable range. There is a trade-off between these two objectives, since increasing the flue gas flow rate can increase the heat transfer coefficient and reduce the heating area, but will increase the resistance on the flue gas side.

In this work, for the boiler of a 1000 MW coal-fired S-CO_2 cycle based on overlap energy utilization, this paper established the model for the thermal calculation of the heating surface in tail flue of the boiler and the model for calculating the working medium pressure drop on both sides of the heating surface. Combined with the minimum entropy production theory and the method of exergy loss analysis, the heating surface is optimized to minimize the cost per unit heat transfer. This work provides a reference for the optimal design of the heating surface in tail flue of S-CO_2 boiler.

2 Calculation Model and Methodology

S-CO_2 unit is quite different from water unit in terms of working medium thermophysical properties and working medium flow. At the same time, the diversion mode also brings changes to the heating surface, the most obvious of which is the change in flue gas pressure drop and heating area. Therefore, it is necessary to design and study the boiler tail heating surface. In order to explore the characteristics of the heating surface of a large capacity system, this work establishes the calculation model for the heating surface in tail flue of a 1000 MW coal-fired S-CO_2 boiler with overlap energy utilization and top-bottom combined cycle [6]. In Figure 1, the heating surface is represented by Heater 4a.

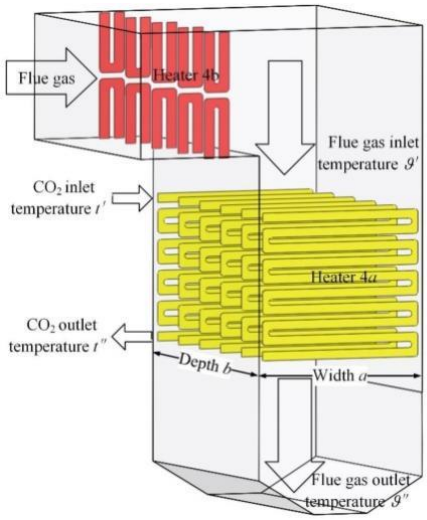

Figure 1 Heating surface in tail flue of an S-CO_2 cycle based on overlap energy utilization

Table 1 Prime table

Nomenclature			
t′	CO_2 inlet temperature	λ	Thermal conductivity
t″	CO_2 outlet temperature	ν	Viscosity
θ′	Flue gas inlet temperature	C_s	Correction factor for tube bundle arrangement
θ″	Flue gas outlet temperature	C_z	Correction factor of tube rows in flue pass
b	Depth	ε	The ash fouling coefficient
a	Width	Ψ	Thermal effective coefficient
Q	Heat absorbed	Pr	Prandtl number
D	Mass flow rate of the working fluid	α_2	Surface heat transfer coefficient
i′	Fluid enthalpy at the inlet	K	Heat transfer coefficient
i″	Fluid enthalpy at the outlet	H	Heating area
B_j	Calculate fuel consumption	Q^{tr}	Heat transfer calculated by heat transfer equation
φ	Thermal efficiency	Re	Reynolds
I'	Flue gas enthalpy at the inlet	ΔP	Pressure drop
I''	Flue gas enthalpy at the outlet	ζ	Friction factor
Δα	Air leakage coefficient	ρ	Density
I_{ca}^0	Enthalpy corresponding to cold air	ΔS	Entropy production
Δt	Temperature difference	ΔE	Exergy loss
d_o	Outer diameter	τ	Conversion coefficient
d_i	Inlet diameter	C_F	Operating cost of the heating surface
s_1	Transverse pitch	c_F	Operating cost per unit heat transfer
s_2	Longitudinal pitch	N	Average annual operating hours
l	Tube length	C_1	Heating surface investment cost
δ	Thickness	c_1	Cost per unit area
α_1	Heat transfer coefficient on the flue gas side	γ	Cost coefficient for operation and maintenance
α_d	Convective heat transfer coefficient of flue gas	CRF	Investment recovery coefficient
α_f	Radiative heat transfer coefficient	i	Loan interest rate
w	Flow velocity	n	Payback period of investment

2.1 Thermal calculation model of heating surface in tail flue

In a boiler, the heat transfer process of the heating surface in tail flue contains not only convection, but also radiation. To facilitate the calculation, the radiative heat transfer is converted to convective heat transfer and calculated by using Newton's law of cooling [7]. The calculation process is shown below.

(1) With given inlet and outlet parameters of the working medium, the heat absorbed by the working fluid is:

$$Q=D(i''-i')/B_j \tag{1}$$

Where D is the mass flow rate of the working fluid with a unit of kg/s, i' and i'' are the fluid enthalpy at the inlet temperature t' and outlet temperature t'', respectively, and B_j is the calculated fuel mass with a unit of kg/s.

(2) Based on energy balance, the heat released by the flue gas is the same as the heat absorbed by the working medium, which can be calculated as:

$$Q=\varphi(I'-I''+\Delta\alpha I^0_{ca}) \tag{2}$$

Where φ is the thermal efficiency taken as 0.99, I' and I'' represent the inlet and outlet enthalpy corresponding to the inlet and outlet temperature ϑ' and ϑ'' of the flue gas, Δα represents the air leakage coefficient, and I^0_{ca} represents the enthalpy corresponding to cold air (20 - 30 ℃).

(3) The temperature difference Δt is calculated as:

$$\Delta t=\frac{\Delta t_{max}-\Delta t_{min}}{\ln\frac{\Delta t_{max}}{\Delta t_{min}}} \tag{3}$$

Where Δt_{max} and Δt_{min} are the maximum and minimum temperature differences between flue gas and working medium on the heating surface, respectively. The position of them depends on the flow directions.

(4) Design the structural parameters of heating surface, and give the values of tube length, inner and outer diameters, transverse pitch, longitudinal pitch, and other parameters. Since there is no comprehensive reference for the design parameters of S-CO_2 system, these values are designed according to the design experience of heating surface of traditional water steam systems [8]. The ranges of structural parameters of heating surface in tail flue are as follows: the outer diameter of tube d_o ranges from 20-60 mm, the transverse pitch s_1 ranges from 20-100 mm, the longitudinal pitch s_2 ranges from 20-400 mm, the number of tubes in a single tube panel n_s ranges from 2 to 16, the tube length l ranges from 30-500 m. The relevant structural parameters are shown in Figure 2.

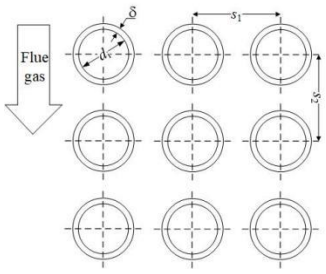

Figure 2 Structural parameters of the heating surface in tail flue

(5) For the flue gas side, after converting radiative heat transfer to convective heat transfer, a converted heat transfer coefficient [9] is obtained, which is called the radiative heat transfer coefficient α_f. The heat transfer coefficient on the flue gas side α_1 can be calculated by the following formula:

$$\alpha_1=\xi(\alpha_d+\alpha_f) \tag{4}$$

Where α_d is the convective heat transfer coefficient of flue gas on the surface, and ξ is the correction coefficient. When the flue gas transversely flows on the in-line tube bundle, take ξ = 1.0.

$$\alpha_d=0.2C_sC_z\frac{\lambda_y}{d_0}\left(\frac{w_yd_0}{\nu_y}\right)^{0.65}Pr_y^{0.33} \tag{5}$$

$$\alpha_f=5.7\times10^{-8}\frac{a_{hb}+1}{2}\alpha_hT^3\times\frac{1-\left(\frac{T_{hb}}{T}\right)^4}{1-\left(\frac{T_{hb}}{T}\right)} \tag{6}$$

C_s refers to the structural correction coefficient, which is related to σ_1 and σ_2 and can be calculated as:

$$C_s=\left[1+\left(2\sigma_1-3\right)\left(1-\frac{\sigma_2}{2}\right)^3\right]^{-2} \tag{7}$$

Where $\sigma_1=s_1/d_o$ and $\sigma_2=s_2/d_o$ with s_1 and s_2 being the transverse and longitudinal pitch sizes, respectively. When $\sigma_1\leqslant1.5$ or $\sigma_2\geqslant2$, C_s=1; when $\sigma_1<2$ and $\sigma_2>3$, take σ_1=3.

C_z represents the correction coefficient of the number of tube rows, and its value is related to the average number of rows z_2 of each tube group of the calculated tube bundle, which is calculated according to the following formula:

$$C_z=0.91+0.0125(z_2-2) \quad \text{when } z_2<10 \tag{8}$$

$$C_z=1 \quad \text{when } z_2\geqslant10 \tag{9}$$

d_o is the tube outer diameter, w_y is the flow velocity of the flue gas, λ_y, ν_y and Pr_y represent thermal conductivity, viscosity, and Prandtl number of the flue gas under average temperature, respectively.

a_{hb} is the blackness of the tube wall, taken as 0.82. T represents the average temperature of flue gas, T_{hb} represents the temperature of the heating surface with ash deposition, a_h represents the blackness of ash containing flue gas at temperature T.

(6) For the working medium side, since CO_2 is in supercritical state and there is no phase change process in the tube, the surface heat transfer coefficient α_2 can be calculated by the following formula:

$$\alpha_2=0.023C_tC_l\frac{\lambda_g}{d_{dl}}\left(\frac{w_gd_{dl}}{\nu_g}\right)^{0.8}Pr_g^{0.4} \tag{10}$$

Where subscript g represents parameters for working medium side, d_{dl} is the equivalent diameter (taken as the inner diameter for circular tube). C_t represents the correction coefficient between fluid temperature and tube wall temperature, which can be taken as 1. C_l represents the correction coefficient of the relative length of the flowing heating surface and can also be taken as 1.

(7) According to the basic principle of heat transfer [10], the general expression of heat transfer coefficient K is:

$$K=\frac{1}{\frac{1}{\alpha_{1h}}+\frac{\delta_h}{\lambda_h}+\frac{\delta_b}{\lambda_b}+\frac{\delta_{sg}}{\lambda_{sg}}+\frac{1}{\alpha_2}} \tag{11}$$

Where α_{1h} is the surface heat transfer coefficient of flue gas to the tube wall surface with ash deposition. δ_h is the thickness of ash layer, and λ_h is the thermal conductivity of ash layer. δ_b is the thickness of tube wall, and λ_b is the thermal conductivity of tube wall. The thermal resistance of the metal tube wall $\frac{\delta_b}{\lambda_b}$ is much smaller than other terms and is negligible. δ_{sg} is the thickness of scale layer, and λ_{sg} is the thermal conductivity of scale layer. Scale deposition is not allowed on the inner wall of the pipe, so that the thermal resistance $\frac{\delta_{sg}}{\lambda_{sg}}$ can be omitted.

In the actual calculation, the following two methods are usually adopted for simplification of the calculation:

(1) Introducing the ash fouling coefficient ε to correct the surface heat transfer coefficient on the flue gas side:

$$\frac{1}{\alpha_{1h}}+\frac{\delta_h}{\lambda_h}=\frac{1}{\alpha_1}+\varepsilon \tag{12}$$

The heat transfer coefficient can then be written as:

$$K=\frac{1}{\frac{1}{\alpha_1}+\varepsilon+\frac{1}{\alpha_2}} \tag{13}$$

(2) Introducing the thermal effective coefficient Ψ to correct the change of heat transfer coefficient caused by pollution:

$$\Psi=\frac{K}{K_0} \tag{14}$$

The heat transfer coefficient can then be written as:

$$K=\Psi\frac{1}{\frac{1}{\alpha_1}+\frac{1}{\alpha_2}} \tag{15}$$

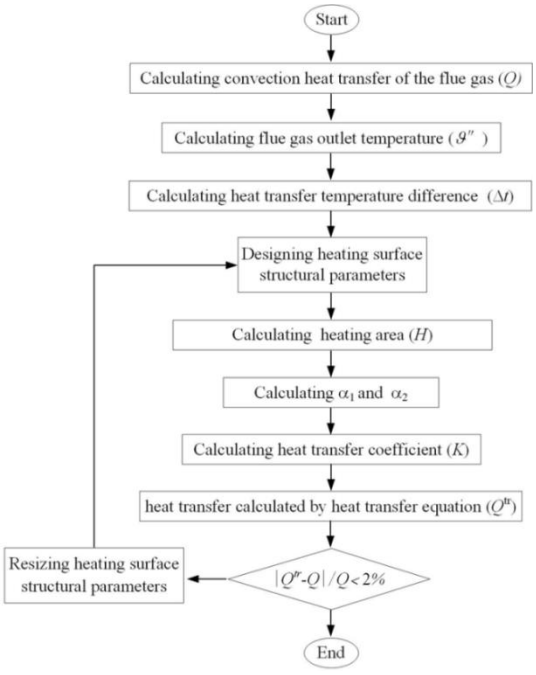

Figure 3 Flow chart of the thermal calculation model

(3) The convective heat transfer of the heating surface is obtained using $Q^{tr}=KH\Delta t/B_j$, where H is the heating area. If the difference between the calculated convective heat transfer Q^{tr} and Q is within an acceptable range $\left|\frac{Q^{tr}-Q}{Q}\right|\cdot 100\% \le 2\%$, the design process of the heating surface is completed. Otherwise, return to step 4, adjust the structural parameters of the heating surface according to the existing calculation results, and repeat the process. The process is shown in Figure 3. The thermophysical properties of supercritical CO_2 were from NIST REFPROP V9.0[11],and thermophysical properties of flue gas were from Ref [6].

2.2 Pressure drop calculation model of heating surface in tail flue

To measure the performance of a heating surface, the pressure drops on the flue gas side and the CO_2 side are important indexes, and can also be used to judge whether the design of the heating surface is reasonable. For the tail flue, the temperature and velocity in the pressure drop calculation formula are taken as the average temperature and average speed [12].

Pressure drop of flue gas ΔP_y can be calculated by:

$$\Delta P_y=\xi_0 z_2\frac{w_y^2}{2}\rho_y \tag{16}$$

Where ξ_0 is the friction factor of a single tube row in the tube bundle, and ρ_y is the equivalent flue gas density. ξ_0 can be calculated based on the structural parameters of the heating surface.

When $\sigma_1\le\sigma_2$:

$$\xi_0=2\left(\frac{s_1}{d_0}-1\right)^{-0.5}Re_y^{-0.2} \tag{17}$$

When $\sigma_1>\sigma_2$:

$$\xi_0=0.38\left(\frac{s_1}{d_0}-1\right)^{-0.5}\left(\frac{s_1-d_0}{s_2-d_0}-0.94\right)^{-0.59}Re_y^{\frac{-0.2}{\left(\frac{s_1-d_0}{s_2-d_0}\right)^2}} \tag{18}$$

Where Re_y is the Reynolds number on the flue gas side.

According to the principle of momentum conservation, when the fluid flows in the tube, the total pressure drop ΔP_g consists of gravitational pressure drop, frictional pressure drop and local resistance loss pressure drop. In the current model, the gravitational pressure drop and local resistance loss pressure drop are ignored, and the frictional pressure drop is calculated using the empirical formula for turbulent flow:

$$\Delta P_g=\zeta\frac{l}{d_{dl}}\frac{w_g^2}{2}\rho_g \tag{19}$$

Where ζ is the friction factor in the turbulent flow regime calculated as $\zeta=0.0055[1+(0.16/d_i+10^6/Re_g)^{1/3}]$, and l is the length of the tube.

The data for the type of coal selected in this work (Table 2), the structural parameters of heating surface

(Table 3), and the design parameters of the boiler (Table 4) are obtained from Ref [9].

Table 2 Properties of the designed coal-type

C_{ar}	H_{ar}	O_{ar}	N_{ar}	S_{ar}	A_{ar}	M_{ar}	V_{daf}	$Q_{net,ar}$
61.7	3.67	8.56	1.12	0.6	8.8	15.55	0.3473	23442

C(carbon), *H*(hydrogen), *O*(oxygen), *N*(nitrogen), *S*(sulfur), A(ash), *M*(moisture), *V*(Volatile)

Table 3 Structural parameters of the heating surface

Parameters	Unit	Formula	Values
Width (a)	m	set value	10
Depth (b)	m	set value	30
Inner diameter (d_i)	mm	set value	27
Thickness (δ)	mm	$10^6P'\times d_i/(156\times10^6-10^6P')+1$	7.583
Outer diameter (d_o)	mm	$d_i+2\delta$	42.166
Transverse pitch (s_1)	mm	$2d_o$	105.416
Longitudinal pitch (s_2)	mm	$1.5d_o$	63.249
Tube length (l)	m	set value	233.8
Number of tube panels (n_1)	/	$(30-0.12)/(s_1)+1$	284
Number of tubes in tube panels (n_2)	/	set value	7
Total number of tubes (n)	/	n_1n_2	1988
Area of heating surface (H)	m^2	$\pi d_o l\times n$	61571.038
Cross-sectional area of CO_2 flow (f)	m^2	$\pi/4\times d_i^2\times n$	1.138
Cross-sectional area of flue gas flow (F_y)	m^2	$30\times14-(14-0.12)d_on_1$	181.685
Effective thickness of radiation layer (S)	m	$0.9d_o(4s_1s_2/\pi d_o^2-1)$	0.143

Table 4 Parameters for the boiler

Parameters	Unit	Values
Boiler efficiency (η_b)	%	94.43
Exit flue gas temperature (ϑ_{exg})	℃	123
Primary air temperature	℃	320
Primary air flow rate ratio	%	19
Secondary air temperature	℃	336
Cold secondary air temperature	℃	21
Environment temperature (t_{ca})	℃	20
Calculate fuel consumption (B_j)	kg/s	87.4

2.3 Model verification

First of all, the thermal calculation and pressure drop calculation is verified for a heating surface of a 1000 MW S-CO_2 coal-fired boiler [13], such as Table 5, it can be seen that the thermal calculation and pressure drop calculation models compiled in this paper can meet the deviation of the heating surface is basically within the allowable range.

Table 5 Model Verification of 1000 MW S-CO_2 coal-fired boiler.

Parameters	Unit	Literature value	Calculated value	Deviation (%)
heat absorption Q	MW	223.46	225.57	0.94
heat transfer coefficient K	$W/(m^{2o}C)$	53.10	54.02	1.73
temperature difference Δt	℃	55.38	55.38	0
heating area H	m^2	67004	66107	1.34
Pressure drop of flue gas ΔP_y	Pa	602.4	598	0.73
Pressure drop of fluid ΔP_g	MPa	0.0957	0.0969	1.25

3 Optimal Design Based on Exergy Loss Analysis

3.1 Entropy production of the heating surface in tail flue

Due to the existence of temperature difference and flow resistance in the heating surface, the total entropy production of the heating surface in tail flue ΔS_g is composed of heat transfer entropy production $\Delta S_{g\Delta T}$ and flow entropy production $\Delta S_{g\Delta P}$. The heat transfer entropy production can be calculated as [14]:

$$\Delta S_{g,\Delta T}=\dot{m}_f c_f \ln\frac{T_{f,o}}{T_{f,i}}+\dot{m}_y c_y \ln\frac{T_{y,o}}{T_{y,i}} \tag{20}$$

Where the subscripts f, y, i, and o represent working medium side, flue gas side, inlet, and outlet, respectively. $\dot{m}$ is the mass flow rate.

The flow entropy production can be calculated as [15]:

$$\Delta S_{g,\Delta P}=\dot{m}_f\frac{\Delta P_f}{\rho_f}\frac{\ln(T_{f,o}/T_{f,i})}{T_{f,o}-T_{f,i}}-\dot{m}_f R_f \ln\frac{P_{y,o}}{P_{y,i}} \tag{21}$$

Finally, the total entropy production of the heating surface is:

$$\Delta S_g=\Delta S_{g,\Delta T}+\Delta S_{g,\Delta P} \tag{22}$$

3.2 Exergy loss of the heating surface in tail flue

The exergy loss is used to judge whether the design of the heating surface is reasonable. In the process of heat transfer, there are operation costs of the heating surface, including cost of heat transfer exergy loss, cost of flow exergy loss, and investment cost of the heating surface. The heat transfer exergy loss $\Delta E_{\Delta T}$ and flow exergy loss $\Delta E_{\Delta P}$ can be obtained by [16]:

$$\Delta E_{\Delta T}=T_0\cdot\Delta S_{g,\Delta T} \tag{23}$$

$$\Delta E_{\Delta P}=T_0\cdot\Delta S_{g,\Delta P} \tag{24}$$

It is worth noting that the costs of heat transfer exergy loss and flow exergy loss cannot be simply added, because the flow of working medium is driven by the pump and

Table 6 Calculated parameters with different inner diameters (Width=10 m)

Number	d_i/(mm)	d_o/(mm)	s_1/(mm)	s_2/(mm)	l/(m)	H/(m^2)	K/W/(m^2·°C)	ΔP_g/(MPa)
1	24	37.7	94.3	56.6	226	59589	62.23	0.172
2	25	39.2	98.0	58.8	229.5	60328	61.47	0.153
3	26	40.7	101.7	61.0	231.8	60964	60.82	0.136
4	27	42.2	105.4	63.3	233.8	61571	60.22	0.121
5	28	43.7	109.1	65.5	236.5	62209	59.60	0.109
6	29	45.1	112.9	67.7	238.8	62821	59.03	0.098
7	30	46.6	116.6	69.9	240.4	63354	58.52	0.088
8	31	48.7	120.3	72.2	242.6	63920	58.00	0.080
9	32	49.6	124.0	74.4	245.4	64515	57.47	0.074
10	33	51.1	127.7	76.6	247.4	65046	57.00	0.067

consumes mechanical work, this paper need to convert the cost of flow exergy loss before adding. The conversion coefficient between them is τ=3-5, and the operating cost of the heating surface C_F can be calculated by [17]:

$$C_F=c_F\cdot(\Delta E_{\Delta T}+\tau\cdot\Delta E_{\Delta P})\cdot N \quad (25)$$

Where c_F represents the operating cost per unit heat transfer and is taken as 40 ¥/GJ. N represents the average annual operating hours and is taken as 5400 h.

The heating surface investment cost C_1 can be calculated by the following formula :

$$C_1=c_1\cdot H\cdot(CRF+\gamma) \quad (26)$$

Where c_1 represents the cost per unit area, taken as 650 ¥/m^2, and H represents the area of the heat exchanger. γ represents the cost coefficient for operation and maintenance which is taken as 0.06, and CRF represents the investment recovery coefficient, which can be obtained by [18]:

$$CRF=[i\cdot(1+i)^n]/[(1+i)^n-1] \quad (27)$$

Where i represents the loan interest rate which is 0.08, and n represents the payback period of investment which is 20 years.

Therefore, this paper can obtain the total cost C of the heating surface as the sum of the operating cost C_F and the investment cost C_1, i.e., $C=C_F+C_1$. The cost per unit heat transfer of the heating surface is obtained as:

$$\overline{C}=\frac{C}{Q} \quad (28)$$

Where Q is the total thermal load of the heating surface.

4 Results and Discussion

4.1 Optimization results and analysis with same boiler width and different inner diameters

Based on the thermal calculation and pressure drop calculation models, the corresponding heat transfer coefficient, heating area and working medium pressure drop on both sides of the heating surface can be obtained for the same boiler width (10 m), as shown in Table 6. In Figure 4, it can be seen that with the change of tube inner diameter d_i, the heating area H and working medium pressure drop ΔP_g show opposite trends: with the increase of tube inner diameter, the heating area increases and the working medium pressure drop decreases.

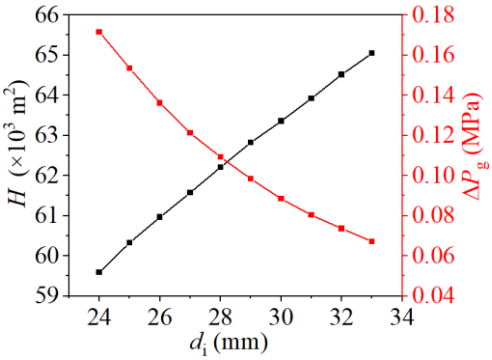

Figure 4 Variations of heating surface area and CO_2 pressure drop with inner diameter

By combining the exergy loss analysis and converting the irreversible loss into the economic index, it is found that when the boiler width is 10 m, with the increase of the inner tube diameter, the cost per unit heat transfer of the heating surface does not show a monotonic variation; it decreases and then increases as shown in Figure 5. Therefore, there is an optimal tube diameter. From Figure 5, it can be seen that the optimal tube diameter is 27 mm. The cost per unit heat transfer of the corresponding heating surface is the lowest, only 4.705 ¥/GJ.

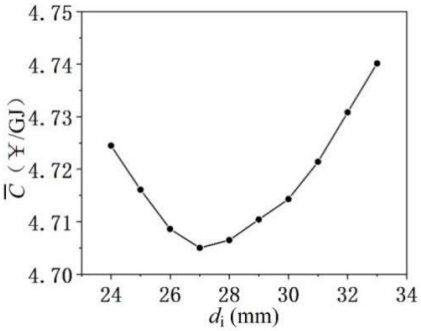

Figure 5 Variation of the cost per unit heat transfer of the heating surface with different inner diameters

4.2 Optimization results and analysis of optimal inner diameter with different boiler widths

The optimal structural parameters corresponding to

Table 7 Optimal structural parameters with different boiler widths

a/(m)	d_i/(mm)	d_o/(mm)	s_1/(mm)	s_2/(mm)	l/(m)	H/(m^2)	K/W/(m^2·°C)	ΔP_y/(Pa)
8	27	42.17	105.4	63.2	207.7	54698	67.80	931.7
9	27	42.17	105.4	63.2	221.1	58227	63.68	739.7
10	27	42.17	105.4	63.2	233.8	61571	60.22	601.6
11	27	42.17	105.4	63.2	245.9	64758	57.26	498.9
12	27	42.17	105.4	63.2	257.4	67786	54.70	420.6
13	27	42.17	105.4	63.2	268.4	70683	52.45	359.3
14	28	43.65	109.1	65.5	281.9	74150	50.00	309.9

the boiler width of 8-14 m are calculated, and the results are shown in Table 7. Figure 6 shows the changes of heating area H and flue gas pressure drop ΔP_y with the boiler width, it is found that the changes of heating area and flue gas pressure drop with different boiler widths are greater than those when the inner diameter is varied with the same boiler width. With varying boiler width, the heating area and flue gas pressure drop also change with opposite trends. Therefore, as the boiler width is varied, the designed heating surface still needs to be optimized by the method of exergy loss analysis.

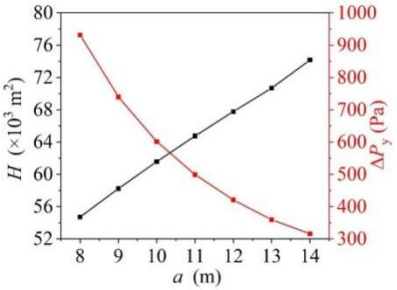

Figure 6 The variations of heating surface area and gas pressure drop with the boiler width

Figure 7 shows the exergy loss analysis results. It shows that with the increase of boiler width a, the cost per unit heat transfer of the heating surface also decreases first and then increases, creating an optimal boiler width of 10 m. The optimal boiler width corresponds to the lowest the cost per unit heat transfer of heating surface of 4.705 ¥/GJ.

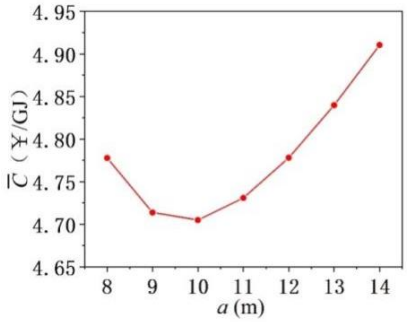

Figure 7 Variation of the cost per unit heat transfer of heating surface with different boiler widths

4.3 Sensitivity analysis

After the calculation, the sensitivity analysis of economic parameters is carried out: cost per unit area c_1, operating cost per unit heat transfer c_F and the conversion coefficient τ fluctuate by 20%. The results are shown in Figure 8: with the change of c_1, the change of $\overline{C}$ is the most obvious. Therefore, c_1 has the greatest influence, so in the process of optimization, the setting of c_1 must be in a reasonable range. After calculation, when c_1 is 650 ¥/m^2, the parameters of the heating surface, such as flue gas velocity, flue gas pressure drop, fluid pressure drop and so on, are the most reasonable.

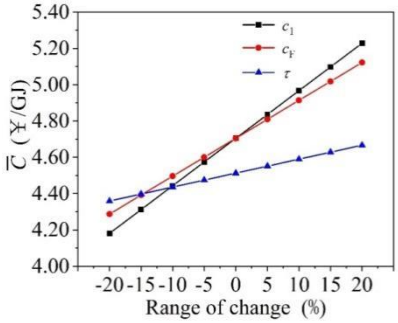

Figure 8 Sensitivity analysis of economic parameters

5 Conclusions

In order to achieve tasks of "carbon peak emission" and "carbon neutrality", it is imperative to develop more efficient and cleaner power generation technologies. The S-CO_2 cycle can greatly improve power generation efficiency compared with water steam Rankine cycle, meanwhile reduce carbon emissions. The heating surface in tail flue of an S-CO_2 top-bottom combined cycle based on overlap energy utilization has small temperature difference and large thermal load, which will lead to excessive heating area. This work develops the models to optimize the structural parameters of the heating surface in tail flue. Combined with the exergy analysis method, the heating surface in tail flue of a 1000 MW power generation system is optimized. It is concluded that the optimal boiler width is 10 m and the optimal inner tube diameter is 27 mm.

Author Contributions: Wenli Ye: Conceptualization, Investigation, Writing-original draft. Jinliang Xu: Conceptualization, Supervision, Writing-review & editing. Guanglin Liu: Writing-review & editing, Verification.

Conflict of Interest: The authors declare that there is no conflict of interest regarding the publication of this paper.

Acknowledgments: This work is supported by

Beijing Nova Program (Z211100002121158). The authors are most grateful to Ms. Chao Liu at the North China Electric Power University for her help and advice during the preparation of this paper.

References

[1] Xu J L, Liu C. Perspective of SCO_2 power cycles. Energy 2019,186:115831.

[2] Bai W , Zhang Y F. 300 MW boiler design study for coal-fired supercritical CO_2 Brayton cycle. Applied Thermal Engineering 2018,135,66-73.

[3] Zhou J, Ling P. Exergy analysis of a 1000 MW single reheat advanced supercritical carbon dioxide coal-fired partial flow power plant. Fuel 2019, 255,115777.

[4] Tong Y J, Duan L Q. Off-design performance analysis of a new 300MW supercritical CO_2 coal-fired boiler. Energy 2020, 216, 119306.

[5] Xu J L, Sun E H. Key issues and solution strategies for supercritical carbon dioxide coal fired power plant. Energy 2018, 157, 227-246.

[6] Sun E H, Xu J L. Overlap energy utilization reaches maximum efficiency for S-CO_2 coal fired power plant: A new principle. Energy Conversion and Management 2019, 195, 99-113.

[7] Yan W P, Yan S L. Principles of Boiler, 2nd ed.; Publisher: Beijing Science press,China,2014;pp. 154-188.

[8] Yang D, Pan J. Experimental study and theoretical calculation on hydrodynamic characteristics of (ultra) supercritical boiler, 1st ed.; Publisher: China Electric Power Press, China ,2017;pp. 205-257.

[9] Design and Calculation method of Industrial Boiler Editorial Board. Industrial boiler design calculation method, 1st ed.; Publisher: China Standards Press,China,2005;pp. 56-89.

[10] Tao W Q. Numerical heat transfer, 2nd ed.; Publisher: Xi'an: Xi'an Jiaotong University Press, China ,2001;pp. 66-110.

[11] https://www.nist.gov/node/580426.

[12] Wang X Y. Engineering Thermodynamics, 2nd ed.; Publisher: China Machine Press, China ,2016;pp. 168-188.

[13] Hu H. Conceptual Design and Optimization of heating Surface of Supercritical carbon dioxide Coal-fired Boiler. Master's thesis, North China Electric Power University, Beijing,2020.

[14] Zhang D, Li J X. Complete exergy efficiency analysis on heat exchangers. Cryogenics and Superconductivity 2009, 37,72-75.

[15] Webb R L. Performance evaluation criteria for use of enhanced heat transfer surface in heat exchanger design. International Journal of Heat and Mass Transfer 1981, 24,715-726.

[16] Cheng X, Zhang Q. Analyses of entransy dissipation, entropy generation and entransy dissipation-based thermal resistance on heat exchanger optimization. Applied Thermal Engineering 2012, 58,31-39.

[17] Zhou L, Xu G. Parametric analysis and process optimization of steam cycle in double reheat ultra-supercritical power plants. Applied Thermal Engineering 2016, 99,652-660.

[18] Xu G, Jin H G. A comprehensive techno-economic analysis method for power generation systems with CO_2 capture. International Journal of Energy Research 2010, 34,321-332.

Viser Technology Pte. Ltd.
Mechanical Engineering Science
DOI: 10.33142/mes.v3i2.6724

Research Article Open Access

Aerothermodynamic Design and Flow Characteristics for a S-CO_2 Radial Inflow Turbine

Lehao HU[1], Yu JIANG[1], Qinghua DENG[1, 2, *], Zhuobin ZHAO[1], Jun LI[1, 2], Zhenping FENG[1]

1 Institute of Turbomachinery, Xi'an Jiaotong University, Xi'an, China
2 Collaboration Innovation Center of Advanced Aeroengine, Beihang University, Beijing 100191, China

***Corresponding Author:** Qinghua DENG, No. 28, Xianning West Road, Xi'an 710049, Shaanxi Province, China; qhdeng@mail.xjtu.edu.cn*

Abstract:
In this paper, a radial inflow turbine is designed for the 150 kW S-CO_2 Brayton cycle system, and flow characteristics and off-design performances are analyzed. The design results are accurate and high performances can be achieved for the S-CO_2 power system, and the total-static efficiency of 86% and net output power about 285.2 kW can meet the design requirements of S-CO_2 cycle system. The results of the flow characteristics show the streamlines of radial inflow turbine distribute uniformly, and the vortexes generated at the shroud of the blade suction surface have little influence on the turbine performances. The off-design performances show the total-static efficiency remains above 80% in the pressure ratio range of 1.6 ～ 2.9, and the output power and mass flow rate increase with the pressure ratio increasing. It is indicated that the designed turbine has excellent off-design performances and can meet the operation requirements. The study results can provide guidance for S-CO_2 radial inflow turbine design and operation.
***Keywords:** supercritical carbon dioxide; radial inflow turbine; flow characteristics; off-design performances*

1 Introduction

A power cycle is a collection of the process and machinery used to generate useful energy such as power energy and mechanical energy from heat sources. There are lots of different power cycles, and the most commonly used for large-scale power generation are Brayton cycle, in which a single-phase gas is in the complete cycle, and Rankine cycle where there is a transition between vapor and liquid phases. In 1968, Angelino [1] and Feher [2] proposed that a supercritical fluid operating in supercritical region, never crossing into the gas-liquid two-phase region, serves as the working fluid of a power cycle. A number of researches have shown that the selection of supercritical carbon dioxide (S-CO_2) as the working fluid for a power cycle can increase the cycle efficiency by making full use of the special physical properties near the critical point, and allow the cycle system to be combined with a wide range of heat sources and the variations of the cycle to be operated with heat rejection to near-ambient sinks due to a nearly ambient critical temperature (31℃) for CO_2.

In addition, the Brayton cycle using S-CO_2 as the working fluid has the potential to attain significantly higher cycle efficiency than either the air Brayton cycle or the steam Rankine cycle, and there is a possibility for the S-CO_2 turbomachinery to be smaller than those of other power cycles due to the relatively high density of S-CO_2 [3]. The efficiency of 50% for S-CO_2 Brayton cycle is greatly larger than that of the ultra-supercritical steam Rankine cycle [4]. The size of component including turbine and compressor employed S-CO_2. Brayton cycle is one fifth as that of turbomachinery used other working fluids such as helium gas at same output power [5]. The results in Ref. [6] have shown that the aerothermal performances of the turbomachinery have the significantly influence on the S-CO_2 Brayton cycle system, and the turbine may be the most complicate component for entire cycle system due to a lack of design experience.

Perhaps the most widely known S-CO_2 turbine designed by Wright et al. [7] was installed in S-CO_2 Brayton cycle loop at Sandia National Laboratory. The designed rotation speed and impeller diameter of the turbine are 75, 000 r/min and 68.1 mm, respectively. The operation indicated that the high density and low viscosity of S-CO_2 have led to fouling, which also results in significant erosion in turbine nozzles [8-9]. The test loop for S-CO_2 Brayton cycle was constructed at Bettis Atomic Power Laboratory to verify the cycle efficiency predicted by theoretical method and investigate the operation characteristics of turbomachinery [10-13]. At inlet of tested turbine that can generate the power energy of 100 kW, temperature and pressure of S-CO_2 are 299 ℃ and 16.3 MPa. However, the cycle efficiency of 7.5% is

Received on October 24, 2021; Accepted on December 23, 2021

far less than that for large-power S-CO_2 Brayton cycle since the greatly larger relative clearance formed stationary component and rotating impeller results in larger leakage flow loss and windage loss. The radial inflow turbine applied to 10 kW scale S-CO_2 Brayton cycle test loop was designed and constructed by Cho et al. [14-17]. The working fluid of 3.04 kg/s can pass through turbine that extract work of 82.4 kW when temperature and pressure at inlet are 453 K and 13 MPa. Considering extremely high rotation speed, the closed impeller is more reasonable comparing to opened impeller because of significantly small blade height and greatly large pressure of S-CO_2. In addition, the numerous scholars including Cho working at Korea Energy Research Institute designed the two different power S-CO_2 Brayton cycles to validate the feasippbility of cycle principle and machined a radial inflow turbine to generate the power. Zhou et al. [18] introduced a design method aimed at radial inflow turbine, designed a 1.5 MW S-CO_2 radial inflow turbine by using the self-programming software and analyzed the flow characteristics based on the numerical study.

The 450 MW S-CO_2 Brayton cycle system with reheat and recompression used for a coal fired power plant was designed and operated by General Electrics Company [19-20]. Based on the cycle, the high-pressure and low-pressure axial turbines whose rotation speed is 3,600 r/min are designed. The working fluid of total temperature of 973.15 K and total pressure of 25.06 MPa at inlet of the high-pressure turbine having four-stage is able to transform the heat energy of 90.6% to mechanical energy, and total-static efficiency of the three-stage low-pressure turbine attains 91.6% while total temperature and total pressure are 953.15 K and 12.96 MPa at inlet. The working fluid passes through the high-pressure and low-pressure turbines from the opposite direction, which decreases significantly the axial thrust and makes turbine operation easier. The blade height of the first-stage and third-stage of the high-pressure turbine are only 71.12 mm 137.16 mm, which is far lower than that of the steam turbine for same power scale turbine.

In this paper, the radial inflow turbine is designed for a 150 kW S-CO_2 Brayton cycle based on the self-programming code, and flow characteristics under design condition and performances under off-design conditions are analyzed by the numerical investigation. The study results can provide the guidance for S-CO_2 radial inflow turbine design and operation [21].

2 Design of S-CO_2 Radial Inflow Turbine

2.1 Aerothermodynamic design of radial inflow turbine

The radial inflow turbine whose performances have a direct influence on cycle efficiency is an important component extracting work from the heat sources. Based on 150 kW S-CO_2 Brayton cycle system composed of the compressor, recuperator, heater, turbine, generator and cooler as shown in Figure 1, design parameters of S-CO_2 turbine are able to be obtained and listed in Table 1. It is worth mentioning that the value of mass flow rate listed in Table 1 for practical design process is about increased to 125% as that shown in Figure 1 required by S-CO_2 Brayton cycle, which ensures that the whole cycle could loop smoothly to avoid unknown losses in main parts and make the output power meet the requirements. Therefore, the mass flow rate is determined as 3.61 kg/s as listed in Table 1. At the moment, it is noted that the values of pressure drop are determined by referring to the S-CO_2 Brayton cycle designed by Sandia National Laboratory. They assumed that the pressure drops for cooler and regenerator at low temperature side are about 0.8% of pressure at compressor inlet, and that of heater and regenerator at high temperature side is 0.8% of pressure at compressor outlet. Therefore, the pressure drop value of cooler and regenerator at low temperature side is set as 65 kPa, and that of heater and regenerator at high temperature side is assumed as 130 kPa in this paper.

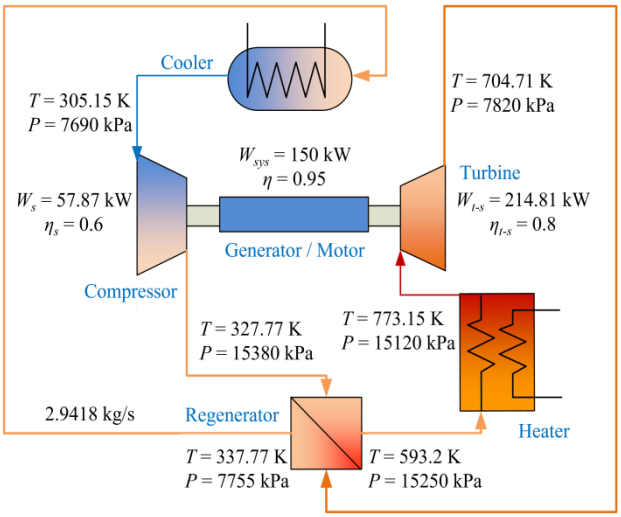

Figure 1 150 kW S-CO_2 Brayton cycle system

The aerothermodynamic design of the radial inflow turbine is based on self-programming code which has been developed and improved by choosing the appropriate loss model [22-23] in order to ensure the results accuracy, and Figure 2 shows flow chart for turbine design. For this program, the total-static efficiency $\eta_{t\text{-}s}$, geometric parameters of turbine and flow parameters of working fluid can be calculated by selecting a set of the load coefficient ψ, flow coefficient Φ and rotational speed n combined with design parameters listed in Table 1. In order to attain the highest total-static efficiency $\eta_{t\text{-}s}$ for a turbine, genetic algorithm is introduced to this program to seek out an optimum setting about ψ, Φ and n. In addition, considering variation of physical properties of CO_2 near or above critical point, the physical properties of the working fluid in this program come from REFPROP 9.0, which is real fluid property database developed by the National Institute of Standards and Technology (NIST). This program has been validated by the reference results to ensure its reasonability and accuracy, and it is also able to be used in the aerothermodynamic design process to achieve high performance for the S-CO_2 radial inflow turbine.

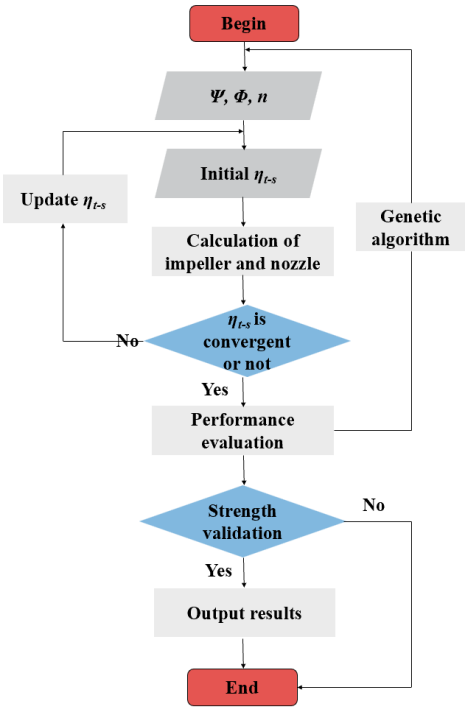

Figure 2 Flow chart of turbine design program

According to the design parameters listed Table 1 and the self-programming code, the geometric and flow parameters of S-CO_2 turbine are obtained and listed in Table 2. Total-static efficiency of 86% is larger than required that of 80%, and net output power about 285.2 kW also meet the design requirements of cycle system. However, it needs to be noted that absolute flow angle at impeller inlet α_1 of 8° is smaller than recommended value based on design experience aimed other working fluid turbine. This is because the relatively large S-CO_2 density at impeller inlet makes the blade height smaller if the recommended flow angle is adopted, which results in increasing flow leakage loss and raising the operation difficulty. The velocity triangle for the designed turbine is presented in Figure 3. Generally, the tip clearance value is depended on impeller blade height of 1% ～ 2% referring to conventional turbine. However, the shroud clearance referring to conventional turbine standard is too small to manufacture impeller blade, thus the value of 0.25 mm is finally determined.

In Figure 3, the subscripts "1" and "2" denote inlet and exit positions of the impeller, respectively. α, β denote absolute and relative flow angle, and C, W, and U denote absolute velocity, relative velocity and tangential velocity, respectively.

Table 1 Design parameters of S-CO_2 turbine

Design parameters	Value
Total temperature at turbine inlet / K	773.15
Total pressure at turbine inlet / MPa	15.12
Static pressure at turbine outlet / MPa	7.82
Mass flow rate / kg s^{-1}	3.61
Total-static efficiency	＞ 80%

Table 2 Design results of S-CO_2 radial inflow turbine

Parameters	Value
Rotation speed / r min^{-1}	60,000
Absolute flow angle at nozzle outlet / °	8
Absolute velocity at nozzle outlet / m s^{-1}	283.59
Blade height of nozzle / mm	3.89
Diameter of at nozzle inlet / mm	114
Diameter of at impeller inlet / mm	93.34
Relative velocity at impeller inlet / m s^{-1}	41.37
Relative flow angle at impeller inlet / °	107.45
Blade height at impeller inlet / mm	3.89
Relative velocity at impeller outlet / m s^{-1}	110.4
Relative flow angle at impeller outlet / °	24.46
Absolute velocity at impeller outlet / m s^{-1}	51.05
Absolute flow angle at impeller outlet / °	102.53
Hub diameter at impeller outlet / mm	20
Shroud diameter at impeller outlet / mm	45.4
Blade height at impeller outlet / mm	12.7
Shroud clearance / mm	0.25
Number of nozzle blade	15
Number of impeller blade	13
Total-static efficiency / %	86.0
Net output power / kW	285.2

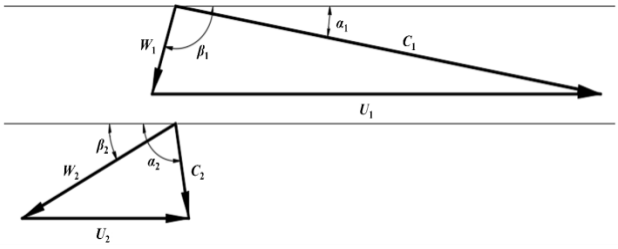

Figure 3 Velocity triangle for S-CO_2 radial inflow turbine

2.2 Blade geometric design

Figure 4(a) shows the meridional passage of S-CO_2 radial inflow turbine according to the parameters as shown in Table 2. In addition, the nozzle plays the major role on transferring the heat energy to kinetic energy and controlling the flow direction so that working fluid can flow smoothly into impeller based on the designed flow angle and fluid expands and extracts work. In this paper, nozzle blade profiles are designed referring to the island-type nozzle blade and the three-dimension geometry is shown in Figure 4(b).

The Non-Uniform Rational B-Splines method is used to design impeller blade profiles. The process of impeller blade design is performed by using the commercial software NUMECA Autoblade. After obtaining the profiles data, the three-dimension geometry is generated as presented in Figure 4(c). In addition, the designed S-CO_2 turbine composed of nozzle and impeller can be used to conduct the investigation of flow characteristics and analysis of the off-design performances.

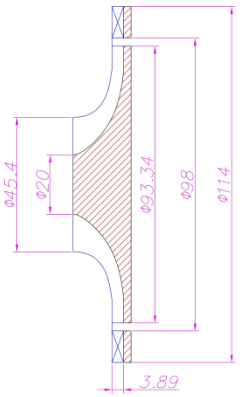

(a) Meridional passage

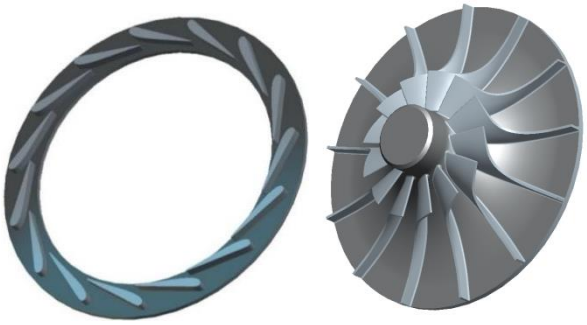

(b) Nozzle (c) Impeller

Figure 4 Schematic diagram of meridional passage and geometry

3 Numerical Method

In this paper, four kinds of turbulence model including Spalart-Almaras (S-A), k-ε, SST and k-ω are validated for the numerical method, and the results of total-static efficiency, output power and mass flow rate are listed in Table 3.

Table 3 Comparison of numerical results for the four turbulence models

Turbulence model	Total-static efficiency / %	Output power / kW	Mass flow rate / kg s^{-1}
S-A	86.00	284.24	3.606
k-ε	86.23	285.39	3.612
SST	86.87	286.32	3.597
k-ω	85.72	284.25	3.619

It is worth noting that there is a few of experimental data for S-CO_2 radial inflow turbine to this day, but no detailed geometry is published together with the performance results. So the results of four turbulence models here are only able to compare with themselves in this paper. As shown in Table 3, the deviations of four turbulence models are so low that the difference on the turbine performances can be ignored. Considering the time cost, S-A model is also most suitable among the four turbulence models. In addition, referring to the paper published by Jiang [24] and Zhang et al. [25], S-A model is often greatly applicable to simulate flow and analyze performances for axial or radial turbomachinery. Therefore, S-A model is reliable to investigate the flow in this paper.

For computational domain of the designed S-CO_2 turbine, mesh with default grid structure is obtained by the commercial software NUMECA Autogrid. Considering the adaptability of flow characteristics in boundary layer, mesh is denser at near-wall, endwall, leading edge, and trailing edge of nozzle and impeller blade. In addition, in order to ensure to meet the requirements of S-A turbulence model, the first cell height on the walls is 4.0×10^{-4} mm so that maximum Y^+ and averaged Y^+ are less than the order of unity. Figure 5 presents the computational domain mesh.

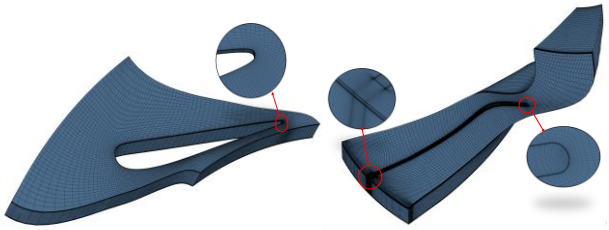

(a) Nozzle (b) Impeller

Figure 5 Mesh of S-CO_2 radial inflow turbine

To investigate accurately flow characteristics, Navier-Stokes equations are solved by using commercial software NUMECA FineTurbo. The four-step Runge-Kutta algorithm is adopted to ensure numerical time integration, and multigrid method is applied in order to decrease the solution time. In order to ensure that the working fluid can flow smoothly into the nozzle and flow out the impeller with no backflow and no vortexes, the extension section is set in front of the nozzle inlet and behind the impeller outlet. During whole computation process, mass flow rate at nozzle inlet and impeller outlet are monitored evaluating the stability of numerical simulation. When mass flow rate reaches to a stable value, less than 1% with additional iterations, simulation results are regarded as a "steady" state. In addition, the convergence of solution is attained with residual values at least below 1.0×10^{-5}. In all computational cases, there are no stability and convergence problems and every simulation typically requires 3,000 iterations.

The boundary conditions are set referring to the design parameters, total inlet pressure of 15.12 MPa, total inlet temperature of 773.15 K, and the flow angle of 45 ° at turbine inlet are set. The static pressure of 7.82 MPa is defined as the boundary condition at the turbine outlet. The rotational speed of the turbine impeller is set to be 60,000 r/min. The non-slip adiabatic wall is set for all walls including the endwall, which is consistent with the physical condition of the S-CO_2 turbine. Similarly, the physical properties of S-CO_2 are from real fluid property database developed by the NIST to ensure the accuracy of numerical simulation.

In order to ensure that the numerical simulation results are independent of grid number, a comparative study has been conducted with three kinds of different meshes of 1.0 million, 1.4 million, 2.0 million, and 3.0 million grids. For each grid, total-static efficiency, output power, and mass flow rate are listed in Table 4 for the design condition. It is seen that the relative deviation of

total-static efficiency for the mesh between 1.0 million grids and 1.4 million grids is 0.16%. With grids increasing to 2.0 million and 3.0 million, the range of relative deviation is 0.04% ～ 0.05%, which indicates that the 1.4 million grids can achieve grid-independent solution.

Table 4 Comparison of numerical results for different meshes

Grid number / M	Total-static efficiency / %	Output power / kW	Mass flow rate / kg s^{-1}
1.0	86.16	284.15	3.598
1.4	86.00	284.24	3.606
2.0	85.97	283.99	3.604
3.0	85.92	284.38	3.611

4 Results and Discussion

4.1 Flow characteristics under the design condition

The static pressure distribution and streamlines in meridional passage for S-CO_2 radial inflow turbine under design condition are presented in Figure 6 and Figure 7, respectively. From Figure 6 and Figure 7, it is seen that static pressure decreases along the flow direction, and there is no static pressure mutation due to no backflow and boundary layer separation near wall for the meridional passage, which indicates that the meridian passage design is reasonable. The averaged flow parameters in the meridional passage are only used to evaluate whole performance of the S-CO_2 turbine, but more details about flow characteristics cannot fully be displayed in Figure 6, and these will be discussed and analyzed in detail in later section.

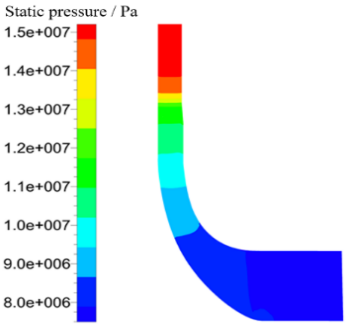

Figure 6 Static pressure distribution

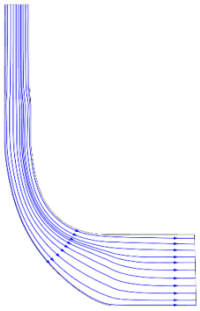

Figure 7 Streamlines in meridian passage

Figure 8 displays static pressure distribution at five span locations on the nozzle blade surface along the flow direction. From hub to shroud, pressure difference between pressure surface and suction surface is constant when horizontal coordinate value is lower than 0.9 as shown in Figure 8, which means that the variation of blade load is small enough. Because of tip clearance of impeller in existence, static pressure of the nozzle near shroud fluctuates.

In addition, static pressure and relative Mach number distribution at the mid-span are presented in Figure 9 and Figure 10. It can be seen that the flow of the working fluid is consistent with static pressure distribution, and there is no existence of the flow separation and the backflow.

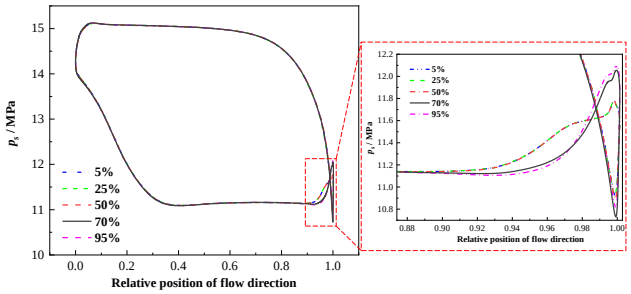

Figure 8 Static pressure distribution on the nozzle blade surface at five span locations

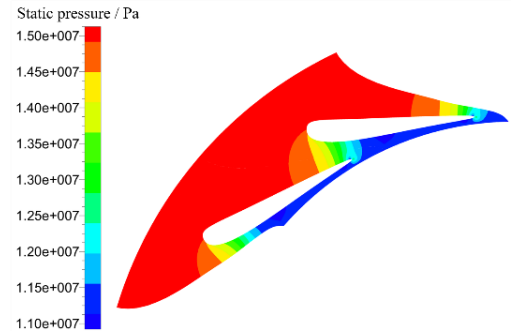

Figure 9 Static pressure at the mid-span

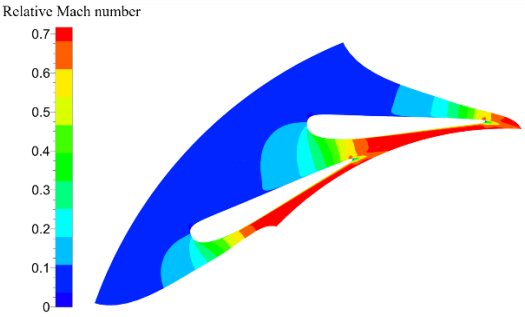

Figure 10 Relative Mach number at the mid-span

Figure 11 shows static pressure on the impeller blade surface at 10% blade height, 50% blade height and 90% blade height along the flow direction. It is found that the relatively larger adverse pressure gradient at the blade leading edge since smaller flow angle at nozzle outlet results in smaller incidence angle, which makes flow separation more serious and static pressure lower at the impeller suction surface at the same linear velocity.

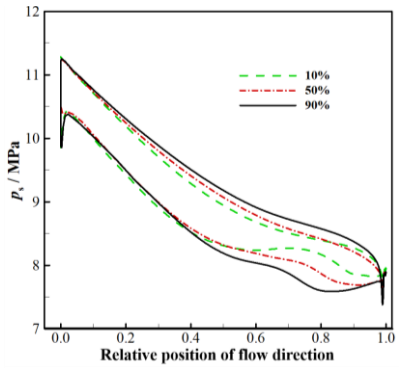

Figure 11 Static pressure distribution on impeller surface at three span locations

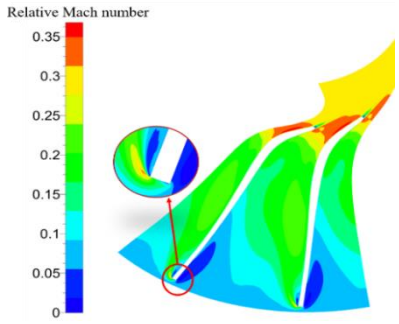

Figure 12 Relative Mach number distribution at the mid-span

The limiting streamlines of pressure surface, suction surface and endwall surface for the S-CO_2 radial inflow turbine are shown in Figure 13. Differing from flow separation observed at the leading edge shown in Figure 13(a) and Figure 13(b), flow separation occurs at the leading edge of pressure and suction surface but the separated flow will adhere quickly to the blade surface as shown in Figure 13(c). On the suction surface, the effect of Coriolis force makes separated flow adhere quickly to suction surface. On pressure surface, the main flow with high energy can impact static pressure due to the existence of negative incidence angle, which makes the low-energy separated flow reattach to the surface. In summary, flow separation has a little influence on the performances.

In Figure 13(a), it can also be clearly found that there is a separation line near blade shroud region and an attachment line near blade bub region, respectively. The separation line is formed by the scraping effect of the casing and the influence of leakage flow in shroud clearance. The scraping effect may not completely suppress the leakage flow due to greatly large relative shroud clearance about 6 %, thus a portion of the leakage flow can flow into pressure surface to interference main flow. The flow direction of the leakage flow in shroud clearance is deflected due to the influence of scraping flow resulting in vortexes in shroud region for the suction surface. Along the flow direction, the phenomenon of flow separation is more obvious because of the combined actions of weakened scraping effect and strengthened leakage flow. In addition, the attachment line on pressure surface is formed by the interaction of leakage flow from shroud clearance of the suction surface and vortexes due to negative attack angle and pressure gradient.

In Figure 13(c) where the limiting streamlines on endwall surface are presented, it can be seen that there is a saddle point at blade leading edge, and the working fluid passing through this point is divided into two streams of fluid entering turbine impeller, which indicates that horseshoe vortexes and flow separation occur at the blade leading edge. After working fluid bypassing the saddle point, the frictional force increases due to the thick boundary layer at inlet, resulting in the low-speed horseshoe vortexes cannot resist effect of centrifugal force generated by rotational impeller and the flow separation, but the streamlines of radial inflow turbine distribute uniformly. In summary, the flow characteristics meet design and operation requirements for S-CO_2 radial inflow turbine.

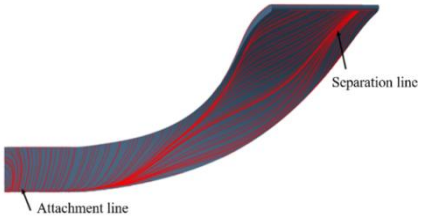

(a) Pressure surface

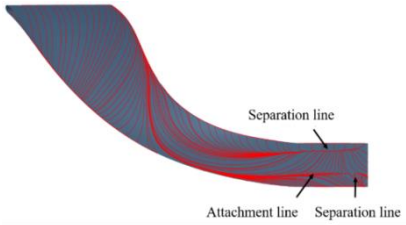

(b) Suction surface

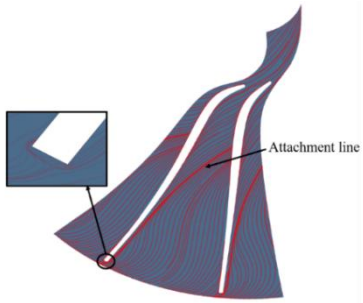

(c) Endwall surface

Figure 13 Limiting streamlines on blade surface

4.2 Performances under off design conditions

Generally, total-static efficiency of the S-CO_2 radial inflow turbine is highest under the design conditions. However, for the actual operation of S-CO_2 Brayton cycle system, the demand determines parameters of the cycle system, which results in turbine operation under the off-designed conditions. In order to provide excellent performances to the cycle system, total-static efficiency, output power and mass flow rate of the S-CO_2 turbine designed in Section 2.2 are studied by numerical method under the different working conditions.

At the time of the variation of cycle system demand, output power of the cycle system is adjusted by changing

turbine parameters such as pressure ratio and rotation speed. The variation of total-static efficiency, output power, and mass flow rate for the S-CO_2 radial inflow turbine with pressure ratio under different operated rotational speeds of 36,000, 45,000, 60,000 and 65,400 r/min are shown in Figure 14. It can be seen that total-static efficiency attains the peak at pressure ratio of 1.9 when operated rotation speed of 60,000 r/min is equal to designed that, as shown in Figure 14(a) where the trend of total-static efficiency with pressure ratio is presented. When pressure ratio ranges from 1.6 to 2.9, total-static efficiency decreases with pressure ratio increasing, but it can remain above 80 %. When pressure ratio is less than 1.6, total-static efficiency decreases rapidly to below 80 % with pressure ratio decreasing. Figure 14(b) and Figure 14(c) show the variation of output power and mass flow with pressure ratio. It can be seen that the output power and mass flow rate increase with pressure ratio increasing.

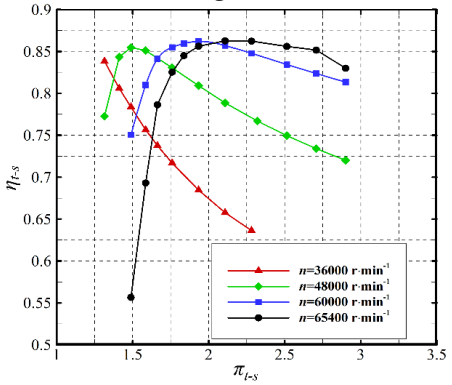

(a) Total-static efficiency

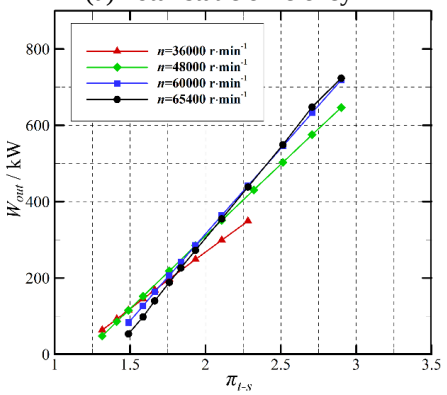

(b) Output power

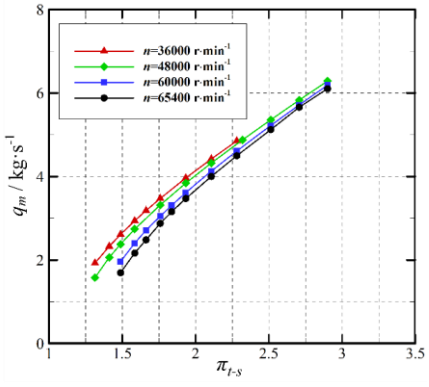

(c) Mass flow rate

Figure 14 Performances of S-CO_2 radial inflow turbine

In fact, there is a highest value of total-static efficiency at an optimal pressure ratio for a certain rotational speed, and lower operated rotational speed will make the optimal pressure ratio smaller from Figure 14(a). At the moment, it can also be found that when the operated rotational speed deviates from the designed that, total-static efficiency decreases whether the pressure ratio increases or decreases. What's more, the high efficiency region will also be more narrowed while the deviations between operated and designed rotational speed increase. In summary, the S-CO_2 radial inflow turbine designed can remain the higher operated total-static efficiency over 80 % in the wide range of operated conditions, which indicates that the turbine has excellent performances under the off-design conditions and meets the operation requirements.

5 Conclusions

In this paper, a radial inflow turbine is designed applied to 150 kW S-CO_2 Brayton cycle based on the self-programming code. In addition, flow characteristics and off-design performances are analyzed by the numerical investigation. The study results can provide the guidance for S-CO_2 radial inflow turbine design and operation. The main conclusions have been drawn as follows:

(1) The design work of thermodynamic design of S-CO_2 radial inflow turbine and three-dimensional profiled design of the nozzle and impeller blade are carried out. The thermodynamic design results are reasonable and accurate and high performances can be achieved for the S-CO_2 radial inflow turbine based on the self-programming code interlocked with REFPROP 9.0. The nozzle blade profiles are designed referring to an island nozzle, and the Non-Uniform Rational B-Splines method is used to design the impeller blade profiles. The total-static efficiency of 86% and net output power about 285.2 kW for the designed turbine can meet the design requirements of the cycle system.

(2) The flow characteristics under design condition are analyzed adopting the mesh of 1.4 million grids that can achieve grid-independent solution. The research results show the static pressure gradually decreases along the flow direction, and the obvious vortexes are generated at the shroud of the blade suction surface under the combined actions of leakage flow and scraping effect, but the streamlines of radial inflow turbine distribute uniformly. Therefore, the vortexes have little influence on the performances of the turbine, and the flow characteristics can meet design and operation requirements of S-CO_2 radial inflow turbine.

(3) The performances under off design condition are studied for the S-CO_2 radial inflow turbine. The study results show that total-static efficiency attains the peak at pressure ratio of 1.9 and operated rotation speed of 60,000 r/min, and total-static efficiency decreases with the pressure ratio increasing, but it still remains above 80 % in pressure ratio range of 1.6 ～ 2.9. What's more, output power and mass flow rate increase with the pressure ratio increasing, which indicates that the turbine has excellent performances under off-design conditions and can meet the operation requirements.

Author Contributions: Conceptualization and Writing-Original Draft Preparation, Lehao Hu;

Methodology, Yu Jiang; Software, Lehao Hu and Zhuobin Zhao; Writing-Review & Editing, Qinghua Deng, Jun Li, and Zhenping Feng.

Conflict of Interest: The authors declare that there is no conflict of interest regarding the publication of this paper.

Acknowledgments: This study is partially supported by National Key R&D Program of China (Grant No. 2017YFB0601804) and Joint Funds Key Program of the National Natural Science Foundation of China (Grant No. U20A20303).

References

[1] Angelino G. Carbon dioxide condensation cycles for power production. Journal of Engineering for Gas Turbines and Power 1968, 90: 287-295.

[2] Feher E G. The supercritical thermodynamic power cycle. Energy Conversion 1968, 8: 85-90.

[3] Cao R, Li Z G, Deng Q H, et al. Design and aerodynamic performance investigations of supercritical carbon dioxide centrifugal compressor. Proceedings of ASME Turbo Expo 2021: Turbomachinery Technical Conference and Exposition, Virtual Online, June 7-11, 2021; The American Society of Mechanical Engineers, New York, US.

[4] Xu J L, Sun E H, Li M J,et al. Key issues and solution strategies for supercritical carbon dioxide coal fired power plant. Energy 2018, 157: 227-246.

[5] Dostal V, Driscoll M J, Hejzlar P. A supercritical carbon dioxide cycle for next generation nuclear reactors; Massachusetts Institute of Technology: Cambridge, US, 2004.

[6] Bru K, Friedman P, Dennis R. Applications of supercritical carbon dioxide based power cycle; Woodhead Publishing: Duxford, UK, 2017.

[7] Wright S A. Summary of the sandia supercritical CO_2 development program supercritical carbon dioxide power cycle symposium; Sandia National Laboratory: Boulder, US, 2010.

[8] Clementoni E M, Cox T L. Practical aspects of supercritical carbon dioxide Brayton system testing. 4th International Symposium-Supercritical CO_2 Power Cycles, Pittsburgh, Pennsylvania, September 9-10, 2014; Southwest Research Institute, Texas, US.

[9] Fleming D D, Pasch J J, Conboy T M,et al. Corrosion and erosion behavior in supercritical CO_2 power cycles; Sandia National Laboratory: Boulder, US, 2011.

[10] Clementoni E M, Kimball K J. Supercritical carbon dioxide Brayton power cycle development overview. Proceedings of ASME Turbo Expo 2012: Turbomachinery Technical Conference and Exposition, Copenhagen, Denmark, June 11-15, 2012; The American Society of Mechanical Engineers, New York, US.

[11] Clementoni E M, Cox T L, Sprague C P. Startup and operation of a supercritical carbon dioxide Brayton cycle. Proceedings of ASME Turbo Expo 2013: Turbomachinery Technical Conference and Exposition, Texas, US, June 3-7, 2013; The American Society of Mechanical Engineers, New York, US.

[12] Clementoni E M, Cox T L. Steady-state power operation of a supercritical carbon dioxide Brayton cycle. Proceedings of ASME Turbo Expo 2014: Turbomachinery Technical Conference and Exposition, Düsseldorf, Germany, June 16-20, 2014; The American Society of Mechanical Engineers, New York, US.

[13] Clementoni E M, Cox T L. Comparison of carbon dioxide property measurements for an operating supercritical Brayton cycle to the Refprop physical properties database. Proceedings of ASME Turbo Expo 2014: Turbomachinery Technical Conference and Exposition, Düsseldorf, Germany, June 16-20, 2014; The American Society of Mechanical Engineers, New York, US.

[14] Cho J, Choi M, Baik Y,et al. Development of the turbomachinery for the supercritical CO_2 power cycle. International Journal of Energy Research 2015, 40: 587-599.

[15] Cho J, Shin H, Ra H S,et al. Development of the supercritical carbon dioxide power cycle experimental loop in KIER. Proceedings of ASME Turbo Expo 2016: Turbomachinery Technical Conference and Exposition, Seoul, South Korean, June 13-27, 2014; The American Society of Mechanical Engineers, New York, US.

[16] Baik Y.J, Cho J, Kim M,et al. Current R&D status of the supercritical carbon dioxide power cycle in KIER. 13th International Conference on Sustainable Energy technologies, Geneva Switzerland, August 25-28, 2014; HES-SO University, Geneva, Switzerland.

[17] Cho J, Ryong S, Minsung P,et al. Design of a small-scale supercritical carbon dioxide power cycle experimental loop. 13th International Conference on Sustainable Energy, technologies, Geneva Switzerland, August 25-28, 2014; HES-SO University, Geneva, Switzerland.

[18] Zhou A Z, Song J, Li X S,et al. Aerodynamic design and numerical analysis of a radial inflow turbine for the supercritical carbon dioxide Brayton cycle. Applied Thermal Engineering 2018, 132: 245-255.

[19] Rahual A B, Andrew M, Rajkeshar S,et al. Conceptual design of 50 MWe and 450 MWe supercritical CO_2 turbomachinery trains for power generation from coal. Part 1: Cycle and turbine. 5th International Symposium-Supercritical CO_2 Power Cycles, Texas, US, March 28-31, 2016; Southwest Research Institute, Texas, US.

[20] Rahual A B, Grant M, Day M,et al. Conceptual designs of 50MWe and 450 MWe supercritical CO_2 turbomachinery trains for power generation from coal. Part 2: Compressors. 5th International Symposium-Supercritical CO_2 Power Cycles, Texas, US, March 28-31, 2016; Southwest Research Institute, Texas, US.

[21] Wright S A, Pickard P S, Fuller R,et al. Supercritical CO_2 Brayton cycle power generation development program and initial test results. Proceedings of the ASME 2009: ASME 2009 Power Conference, New Mexico, USA. July 21-23, 2009, The American Society of Mechanical Engineers, New York, US.

[22] Balje O E, Binsley R L. Axial turbine performance evaluation Part a: loss-geometry relationship. Journal of Engineering for Power, Transaction of the ASME, 1968, 90: 341-348.

[23] Balje O E. A contribution to the problem of designing radial turbomachines, Transaction of the ASME 1952, 74: 451.

[24] Jiang Y. Comprehensive design of supercritical carbon dioxide power cycle prototype optimization system thermodynamic performance. Master Thesis, Xi'an Jiaotong University, Xi'an, 2019.

[25] Zhang H Z, Zhao H, Deng Q H,et al. Aerothermodynamic design and numerical investigation of supercritical carbon dioxide turbine. Proceedings of ASME Turbo Expo 2015: Turbomachinery Technical Conference and Exposition, Montreal, Canada, June 15-19, 2015; The American Society of Mechanical Engineers, New York, US.

Viser Technology Pte. Ltd.
Mechanical Engineering Science
DOI: 10.33142/mes.v3i2.6725

Research Article Open Access

Influence of Different Equations of State on Simulation Results of Supercritical CO_2 Centrifugal Compressor

Yueming YANG[1], Bingkun MA[1], Yongqing XIAO[1], Jianhui QI[1,2*]

1 Shandong Engineering Laboratory for High-efficiency Energy Conservation and Energy Storage Technology & Equipment, School of Energy and Power Engineering, Shandong University, Jinan, China
2 Beijing Key Laboratory of Multiphase Flow and Heat Transfer for Low Grade Energy Utilization, North China Electric Power University, Beijing, China

***Corresponding Author:** QI Jian-hui, No. 17923 Jingshi Road, Jinan, China; j.qi@sdu.edu.cn*

Abstract:
Supercritical CO_2 (SCO_2) Brayton cycle has received more and more attention in the field of power generation due to its high cycle efficiency and compact structure. SCO_2 compressor is the core component of the cycle, and the improvement of its performance is the key to improving the efficiency of the entire cycle. However, the operation of the SCO_2 compressor near the critical point has brought many design and operation problems. Based on the Reynolds Averaged Navier-Stokes (RANS) model, the performance and flow field of SCO_2 centrifugal compressors based on different CO_2 working fluid models are numerically investigated in this paper. The stability and convergence of the compressor steady-state simulation are also discussed. The results show that the fluid based on the Span-Wanger (SW) equation can obtain a more ideal compressor performance curve and capture a more accurate flow field structure, while the CO_2 ideal gas is not suitable for the calculation of SCO_2 centrifugal compressors. But its flow field can be used as the initial flow field for numerical calculation of centrifugal compressor based on CO_2 real gas.
***Keywords:** Supercritical CO_2; Centrifugal compressor; Near the critical point; Compressor performance; Real gas equation of state*

Table 1 Prime table

Nomenclature		Subscripts	
r	Radius	0	Stagnation temperature or pressure
b	Width	1	Main blade inlet
η	Isentropic efficiency	2	Impeller exit
ε	Pressure ratio	3	Splitter blade inlet
p	Static pressure	t	Tip
T	Static temperature	s	Shroud
m	Mass flow rate	h	Hub
N	Impeller rotation speed	c	Critical state
V	Specific volume	u	General gas symbol
R	Gas constant		
w	Eccentricity factor.		
M_r	Molecular weight		
f	Helmholtz free energy		

1 Introduction

As a rapidly developing country, China has become the world's largest energy consumption country. In a long time to come, coal will still be the primary energy consumption. However, the massive consumption of fossil leads to problems such as climate warming and pollution, which have had a significant impact on the sustainable development of our country. In 2020, China officially committed to peak carbon dioxide emissions before 2030 and achieve carbon neutrality before 2060. The reduction of carbon emissions, the use of clean energy, and the improvement of energy efficiency have been included in the national strategy. The power system bridges human society and energy resources, and every gain on efficiency will make a great breakthrough in energy-saving and emission reduction. Using an advanced power cycle is one method to enhance the power system efficiency.

Supercritical CO_2 (SCO_2) Brayton cycle is a

Received on October 13, 2021; Accepted on December 9, 2021

promising power cycle with great potential. SCO_2 is used as a working fluid in the cycle and no phase transition occurs during heating and cooling stages. Moreover, SCO_2 has the characteristics of large specific heat and low dynamic viscosity under operating conditions, which can realize thermal energy conversion more efficiently. The cycle not only has great application value in fossil energy power generation[1] but also has broad prospects in nuclear power[2], geothermal energy[3], solar power generation[4], and waste heat recovery[5]. However, in addition to high efficiency, another advantage of the SCO_2 Brayton cycle is that it has a more compact structure size. Due to its miniaturized system components and compact configuration, it has advantages for restricted space and weight applications, such as marine ships and interspace power systems [6]. However, the performance of some system components restricts the development and application of SCO_2 power systems, such as turbomachinery. Turbomachinery, including turbines and compressors, are the most important components in the SCO_2 power cycle. Sharp changes in fluid properties introduce greater uncertainties into experimental measurements and affect the accuracy of numerical simulations. This uncertainty becomes more prominent when the operating conditions approach the critical point. The most affected by the critical point physical properties of the system component is the compressor [7]. Hence, the SCO_2 compressor needs more attention.

As illustrated in previous studies, for lower power SCO_2 Brayton cycles, centrifugal compressors perform better than axial compressors in terms of stability and efficiency [8-9]. The study by Angelino and Invernizzi showed that the efficiency of both the SCO_2 compressor and the cycle increases when the compressor inlet conditions get near the CO_2 critical point [10]. Thus, keeping the operating point near the CO_2 critical point is essential for SCO_2 compressors, which helps reduce the compression work. However, Lee et al. proved that the dramatic changes in the thermodynamic properties of CO_2 near the critical point will lead to very high uncertainty in the prediction of compressor performance through experiments [11]. Kim et al. indicated that when the operating point approaches the critical points, the errors between numerical simulations and experiments will be increased [12]. Bao Wen-rui studied the internal flow structure of the SCO_2 centrifugal compressor at different inlet temperatures, and recommended an optimized inlet temperature for the off-design conditions [13]. Currently, the three-dimensional (3D) computational fluid dynamics (CFD) simulation is the most popular method for analyzing turbomachinery performance. Exploring the physical properties of the fluid in the SCO_2 centrifugal compressor and expanding the stability of the compressor are the focus of related research. Therefore, it is important to ensure the accuracy of the CO_2 thermophysical property model, and guarantee the convergence and stability of the solution process. This is necessary to optimize the design of SCO_2 centrifugal compressors.

This paper carries out a numerical simulation of a centrifugal compressor in a 350 kW SCO_2 power cycle. In the first part of the paper, brief descriptions of the studied compressor and computational domain are provided. Then, the numerical methodology and method verification are discussed. And the effect of RGP table resolution on the compressor performance is investigated. Finally, explore the effects of different CO_2 thermophysical properties models on its performance and flow field, and discuss the convergence issues in the numeical solution process.

2 Studied Case

2.1 Research model

Table 2 Main design parameters for SCO_2 compressor impeller

Model parameters	Value
Exit blade height (b_2)/mm	a
Inlet shroud radius (r_{s1})/mm	6.55a
Inlet hub radius (r_{h1})/mm	4a
Outlet radius (r_{t2})/mm	19.25a
Tip clearance(constant)/mm	0.15a
Inlet blade angle at tip/ °	58
Number main and splitter blades/-	8

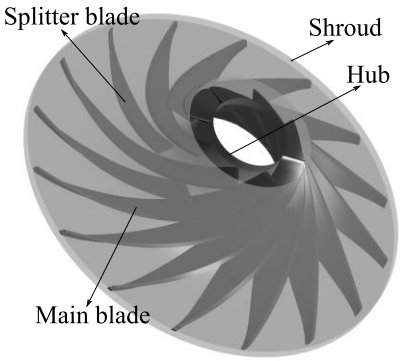

Figure 1 The 3D schematic of the SCO_2 compressor impeller

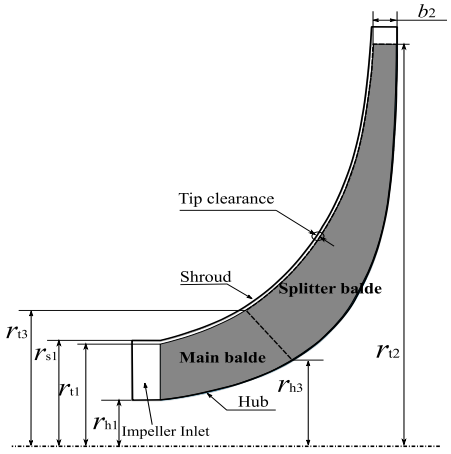

Figure 2 Meridional view of compressor's impeller

In this study, a single-stage centrifugal compressor is studied. As it is temporarily unable to disclose all design parameters, this article parameterizes the main size parameters, as shown in Table 2. As shown in

Figure1, the computational domain of the compressor impeller is generated by the modeling software SolidWorks. The meridional view of the impeller passage is shown in Figure2. The centrifugal compressor impeller consists of 8 main blades and 8 splitter blades. The designed mass flow rate (m) of the compressor is 6.4 kg/s, and the designed rotational speed (N) is 40,000 r/min.

2.2 Grid scheme

As shown in Figure3, a high-quality structured mesh of the impeller single passage was generated with ANSYS TurboGrid. For the reason that the blade tip clearance has an obvious influence on the flow field of the compressor, the mesh on the gap region was refined. Similar, it is necessary to ensure sufficient numbers of cells near the wall, so that the value of y+ for the first layer of near-wall-grid was between 1 and 5.

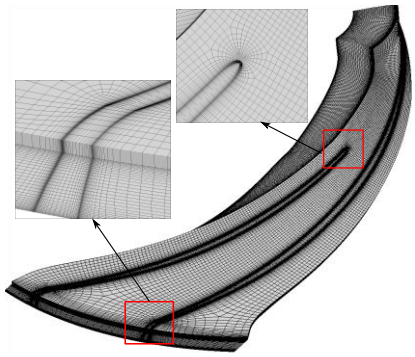

Figure 3 Single passage computational grid of the impeller

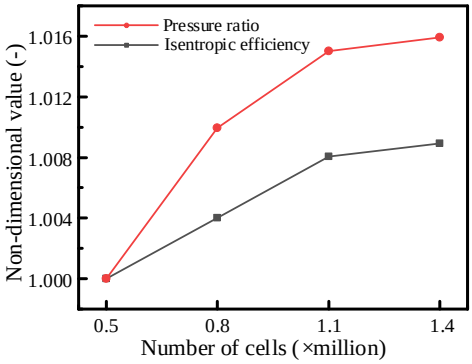

Figure 4 Schematic diagram of grid independence verification results

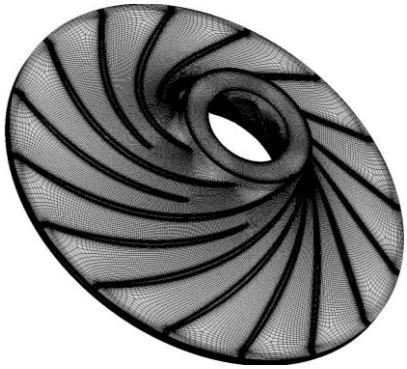

Figure 5 Computational grid of the impeller

The grid independence study was carried out with four different grid sizes. The number of cells for a single passage varies from 0.5 to 1.4 million with an increment of 0.3 million. For centrifugal compressors, we usually use pressure ratio (ε) and isentropic efficiency (η) to show their performances. These two parameters were used as monitored variables for the grid independence verification. Figure 4 shows the mesh dependency test for the studied centrifugal compressor. If the number of grids continues to increase after 1.1 million, the dimensionless values of the ε and η were both in the order of 10^{-3}, but the calculation speed dropped sharply. Therefore, a single-passage grid scheme with 1.1 million cells was adopted. And then import the grid into ICEM CFD to generate a full-passage grid scheme. The average y+ is 1.6 for the impeller single passage, which is in the reasonable range. Figure 5 shows the final computational grid scheme of the SCO_2 centrifugal compressor.

3 Methodology

3.1 Numerical method and boundary conditions

In this study, the commercial software ANSYS CFX[14] was used to simulate the 3D steady-state flow of the compressor. The solver adopts the finite volume method (FVM) based on finite elements, which not only guarantees the conservation characteristics of the finite volume method but also absorbs the numerical accuracy of the finite element method.

The internal flow of the compressor is very complicated, including many separated flows. Therefore, the turbulence model adopted the k-ω Shear Stress Transport (k-ω SST) model, which predicts the flow (such as separated flow) against the pressure gradient more accurately. The uniform m and total temperature (T01) were imposed at the compressor inlet boundary condition. The static pressure (p2) was imposed at the compressor outlet. The reference pressure was set to zero, and no slip-wall was employed on any solid wall. The high-resolution method was used at advection scheme and turbulence numerics. The convergence limit residual value of each physical quantity was set to 10^{-5}.

3.2 Validation through SNL's experiments

To validate the ability of ANSYS-CFX on solving the fluid field of the SCO_2 compressor, a SCO_2 compressor of Sandia National Laboratory (SNL) was simulated. The simulation results are used to compare with the experimental data. Table 3 shows the main parameters of the SNL compressor [15]. The characteristics of the small and high-speed SNL's compressor are similar to those of the SCO_2 centrifugal compressor in this study. Based on the ANSYS Workbench platform, BladeGen was used to generate a main compressor impeller model. TurboGrid was used to produce a high-quality structured grid. And CFX was used to perform steady-state calculations. The geometric model of the impeller reproduced during the verification process is provided in Figure 6. In terms of simulation settings, the

in-house Python code was used to invoke the CO_2 real gas properties in NIST REFPROP, and the *k-ω* SST model was also used to close the control equation. Table 4 lists other simulation condition settings.

Table 5 illustrates the difference between the simulation results and the experiments. The efficiency obtained from simulation is 70.1 %, which is 2.3 % higher than the experimental results, 67.8%. The pressure ratio is 1.20, which is identical to the experimental data. This fully proves the rationality of the simulation process in this research.

Table 3 SNL's compressor impeller parameters

Impeller Parameters	Value
Inlet shroud radius (r_{s1})/mm	9.372
Inlet hub radius (r_{h1})/mm	2.537
Outlet radius (r_{t2})/mm	18.681
Exit blade height (b_2)/mm	1.712
Inlet blade angle at tip/ °	50
Blade tip angle (minus is backswept)/ °	-50
Blade thickness/mm	0.762
Number main and split blades/-	6

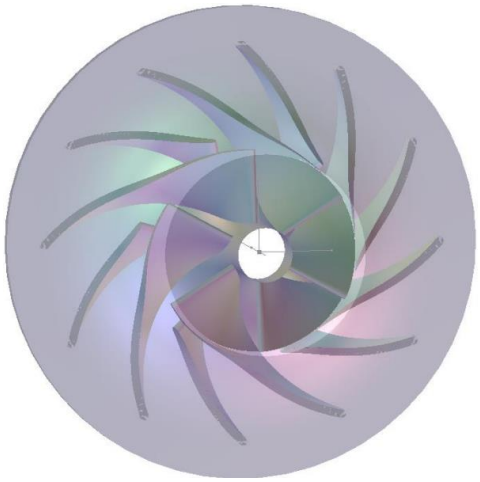

Figure 6 The 3D geometric model of SNL's compressor impeller

Table 4 SNL's compressor simulation settings

Location	Settings
Impeller inlet	p_{01} = 7.687 MPa T_{01} = 305.3 K
Computing domain outlet	m = 3.53 kg/s
Rotation speed	N = 50,000 r/min
Wall	Adiabatic、No Slip Wall
Working fluid	CO_2 Real Gas (Based on NIST REFPROP)

Table 5 Comparison of simulation results and experimental results

	Efficiency (η)/%	Pressure ratio (ε)/-
CFD	70.1	1.20
Laboratory data	67.8	1.20

4 Results and Analysis

To explore the influence of different CO_2 thermophysical properties models and real gas effects on the flow performance and flow field of SCO_2 compressors, this paper constructed three SCO_2 physical properties working fluid models, including CO_2 ideal gas model, CO_2 real gas model based on cubic Aungier-Redlich-Kwong equation of state (RK EoS), and CO_2 real gas property model based on Span-Wanger equation of state (SW EoS). The compressor used these three working fluids for steady-state numerical calculation.

4.1 CO_2 ideal gas property model

SCO_2 is assumed to be an ideal gas, and the thermodynamic process in the compressor satisfies the following equation:

$$pV = R_g T \quad (1)$$

$$pV^{\kappa} = C \quad (2)$$

κ is the isentropic index which is the ratio of the specific heat capacity at constant pressure and the specific heat capacity at a constant volume. For an ideal CO_2 gas, κ = 1.29, C is a constant.

The performance of the CO_2 ideal gas model for centrifugal compressors was studied below. In order to facilitate the comparison with the data based on the real gas model, the simulation used the same T01 and p01. Figure 7 shows that the compressor surges at the mass flow rate of about 1.8 kg/s under the designed rotational speed. This is consistent with the simulation results because the relevant calculation error occurs at a 1.8 kg/s flow rate. The flow choking phenomenon will occur when m reaches about 5.2 kg/s, and related errors will also appear in the ANSYS CFX solver. Compressor simulated with ideal gas models cannot reach the design m of 6.4 kg/s. In the actual operation of the compressor, the temperature and pressure of the working fluid in the impeller will increase from the inlet to the outlet. The density of ideal gas changes linearly with temperature and pressure, and it can be considered that the density changes little. However, for CO_2 real gas, the density near the critical point varies dramatically with temperature and pressure and will reach a larger value. Therefore, m of the compressor with ideal gas as working fluid cannot reach the design m of real gas working fluid. In addition, with the increase of m, the decrease of ε almost decreases at the same rate, which conforms to the performance curve shape of the general centrifugal compressor. However, for the performance curve where the η varies with m, the highest efficiency point appears near the surge flow rate, which is not in line with the actual situation.

In summary, when CO_2 ideal gas is used as the working fluid of the compressor, the real gas effect cannot be exerted. The performance of the compressor will be reduced significantly compared with the real refrigerant compressor. For the entire Brayton cycle, it will become an important factor in reducing cycle efficiency.

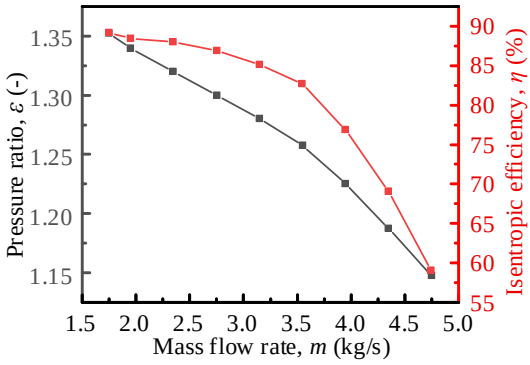

Figure 7 Performance curve of the centrifugal compressor based on CO_2 ideal gas

4.2 CO_2 real gas property models

4.2.1 Real gas calculated by RK EoS

Compared with other real gas EoS, the cubic EoS has the advantages of fewer variables, greater flexibility, and higher accuracy. These equations are widely used in engineering applications. One of them is RK EoS. The fluid based on CO_2 RK EoS is used in this study comes from the ANSYS CFX database. Its thermophysical properties are calculated using the Aungier-Redlich-Kwong cubic EoS [16]. The formula is shown in the appendix.

4.2.2 Real gas calculated by SW EoS

Span and Wanger proposed a multi-parameter state equation of CO_2 physical properties based on Helmholtz free energy [17]. Because of the wide range of applications, this equation can more accurately capture the changes in the thermal properties of CO_2 in the supercritical region and near the critical point. At the same time, due to closer to the experimental measurement data, it is recommended by the National Institute of Standard and Technology. The equation consists of the ideal part and the remaining part, and it is shown in the appendix.

4.2.3 RGP table based on SW EoS

An RGP file combining the NIST REFPROP database was encoded and employed for numerical analysis to deal with the dramatic variation of CO_2 thermophysical properties. Import the generated physical property parameter table (RGP table) into the ANSYS CFX solver to define a new working fluid. The bilinear interpolation method was used to calculate the thermophysical properties. It can be seen that the higher the resolution of the RGP tables, the more accurate the simulation. Especially at the adjacent region of the critical point, the thermodynamic properties of CO_2 change drastically with the variation of temperature and pressure. However, if the resolution of the physical property table is too high, it will have a large effect on the stability and convergence of the numerical calculation of the SCO_2 compressor [18]. ANSYS CFX solver has limited memory capacity to read the RGP table. So, if the resolution is too high, the table will not be read. Considering the above facts, an optimum resolution of the table will have to be found.

Similar to the grid-independent study, the pressure ratio and isentropic efficiency of the centrifugal compressor were used as the monitor in the dependency study of RGP tables. In this study, the RGP table ranges 250-450 K and 3-30 MPa for temperature and pressure, respectively. Six RGP tables have various resolutions from 50×50 up to 800×800 points. Same boundary conditions are assigned to the simulation cases with different table resolutions. The boundary condition settings are listed in Table 6. In order to express the changes intuitively, a nondimensional value was obtained by dividing the simulated performance data by the simulated data of the highest resolution table calculation results. Figure 8 shows the independent study results of the RGP table. As the resolution increases, the total pressure ratio rises gradually, and the isentropic efficiency shows a trend of oscillation convergence. When the resolution exceeds 400×400, the performance of the SCO_2 compressor tends to be steady. But, when the resolution is lower than 400×400, the simulation becomes unstable and the error becomes significant. Considering the stability, convergence, and accuracy of the simulation, RGP tables with a resolution of 400×400 are used.

Table 6 Boundary conditions applied to the independent study of RGP table resolution

Location	Boundary Conditions
Impeller inlet	T_{01} = 306.15 K m = 6.4 m/s
Computing domain outlet	p_2= 12 MPa
Rotation speed	N = 12,000 r/min
Working fluid	CO_2 Real Gas (Based on NIST REFPROP)

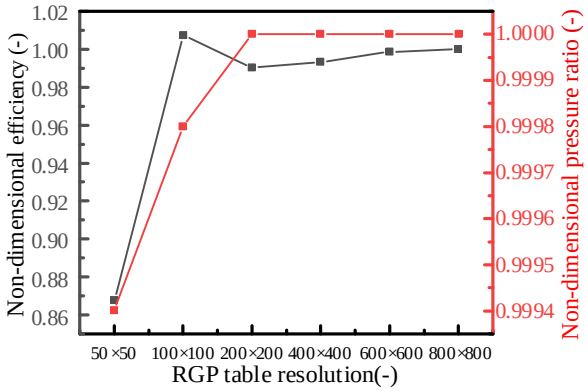

Figure 8 Accuracy of the RGP tables

A study on the convergence and stability of the RGP table with different resolutions at various compressor rotation speeds is also carried out, as shown in Figure9. If the number of convergence steps is equal to zero, it indicates the simulation is divergent at this speed. At the same speed, with the resolution of the RGP table increasing, the convergence steps of the simulation increase, which is more difficult to converge. This is

because, when the rotational speed increases, the temperature and pressure near the leading edge will decrease. Thus, it is easier that the fluid properties drop into the metastable region below the critical point. This makes it difficult to calculate physical properties with drastic changes in physical properties

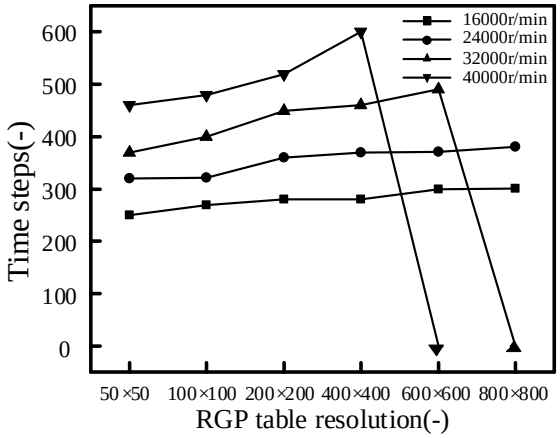

Figure 9 Stability test of RGP tables with different resolutions at different rotational speeds

To increase the convergence rate of the simulation, this study tries to initialize the flow field with simulation results of the ideal gas. Figure 10 compares the average residual convergence curves of the momentum equation with and without initialized flow field. It can be seen that after initializing the flow field, the convergence speed of numerical simulation is greatly improved, and the convergence residual is smaller. So, it is necessary to initialize the flow field for the following simulation with real gas.

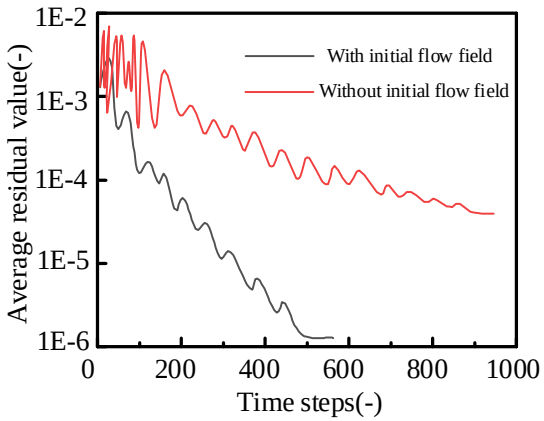

Figure 10 Convergence history of momentum equation with or without initialization

4.3 Comparison of two real gas EoSs

To explore the influence of two sets of real gas EoSs on the steady-state simulation of SCO_2 centrifugal compressor, the ε of compressors calculated by two real gas EoSs under four different speeds are compared in this paper, as shown in Figure11. With the increase of rotational speed, the ε is also increasing. However, the ε calculated with RK EoS is lower than that calculated by SW EoS. Besides, with the increase of rotational speed, the gap between the ε of the two increases gradually. The reason for this phenomenon is that the calculation accuracy of the cubic EoS in the near-critical and supercritical regions is inferior to the Helmholtz free energy EoS [19]. After many iterations, the error accumulates, which leads to the inability for simulations near the critical point and supercritical state. As the speed increases, the pressure and temperature near the leading edge of the blade drop to a position closer to the critical point due to local acceleration. However, near the critical point, the RK EoS will produce greater calculation errors. Compared with the ideal gas, the performance of the centrifugal compressor calculated by the steady-state numerical simulation of the CO_2 real gas based on the RK EoS is still greatly improved.

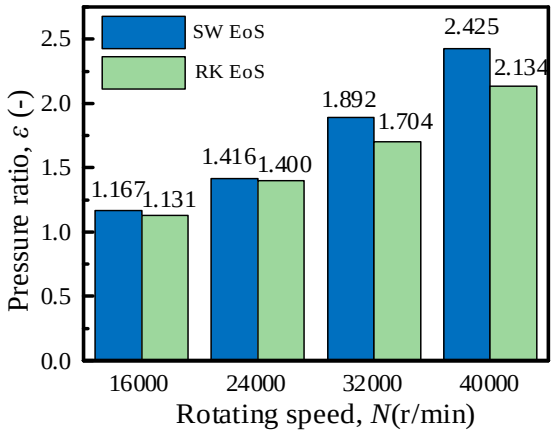

Figure 11 Comparison of the pressure ratio of two CO_2 real gas property models under steady-state simulation calculations at different speeds

The flow fields of the simulation with two CO_2 real gas EoSs are compared and analyzed in Figure12. The x-axis indicates the normalized streamwise position, and 0 is the entrance, 1 is the exit. From the entrance to the exit, the temperature and pressure will show an overall increase. There are local fluctuations in thermodynamic properties near the leading edge due to the flow separations, which leads to a certain level of losses. In Figure12 (a), the static pressure and total pressure of fluid calculated by RK EoS are higher than fluid calculated by SW EoS at the inlet, but along the streamwise direction, the difference between the two working fluid parameters is gradually reduced. At the exit, the total pressure of CO_2 real gas calculated by SW EoS has exceeded that calculated by RK EoS, and the static pressure level is very close. In Figure12 (b), the difference between the total temperature and static temperature of the CO_2 real gas calculated by SW EoS has exceeded that calculated by RK EoS. Observing the operating fluid parameter level, we can see that the working fluid calculated by the SW EoS shows better operating performance at a fixed speed.

Figure 13 illustrates the distributions of streamlines in the impeller internal passage of the centrifugal compressors. In the tip clearance of the main blade and the splitter blade, the phenomenon of flow across the tip clearance is normal. The flow velocity increases in the tip clearance and the flow across the tip clearance is

more obvious in the latter half of the blade. More swirls form in the passage when the fluid calculated by RK EoS crosses the tip clearance, which leads to easier flow separation and more losses. The position of the vortex is marked by a red line frame in Figure13. It can be seen that the low-speed area caused by the vortex in the flow field of RK EoS is significantly larger than that in the flow field of SW EoS. This also explains the reason why the parameter curve of RK EoS is lower than that of SW EoS in Figure12. In other words, this is an important reason that the performance of a centrifugal compressor with CO_2 real gas based on SW EoS is better than that with CO_2 real gas based on RK EoS.

Figure 14 shows the pressure distribution near the leading edge of the blade when the compressor operates on three different working fluids. Both the CO_2 ideal gas flow field and the CO_2 real gas flow field will show a pressure drop at the leading edge of the blade. The pressure drop of the ideal gas is relatively gentle and small, and the pressure is above the critical pressure. The pressure drop of the real gas flow field is drastic, especially for the flow field based on the SW EoS. The pressure in a considerable part of the area has dropped below the critical point (pressure lower than 7.38 MPa). The profile curvature at the leading edge of the main blade changes the most, so the fluid velocity gradient also increases. The fluid velocity increased dramatically, resulting in a distinct low-pressure and low-temperature region at the leading edge of the main blade. In other words, the phenomenon of flow acceleration at the leading edge of the compressor impeller will cause the working fluid to enter the two-phase region. A criterion for determining whether condensation of supercritical carbon dioxide has occurred deserves further discussion. It can also be observed that the pressure rise near the tip of the blade leading edge due to flow impact is also more intense in a real gas. The Mach number and entropy contours at 80% span are presented in Figure 15. As can be seen from the Mach number contour, the flow acceleration occurs at the leading edge of the blade suction side. Since entropy increase is an important sign of flow loss, it can be seen from the entropy contour that the existence of the two-phase region has produced a larger loss.

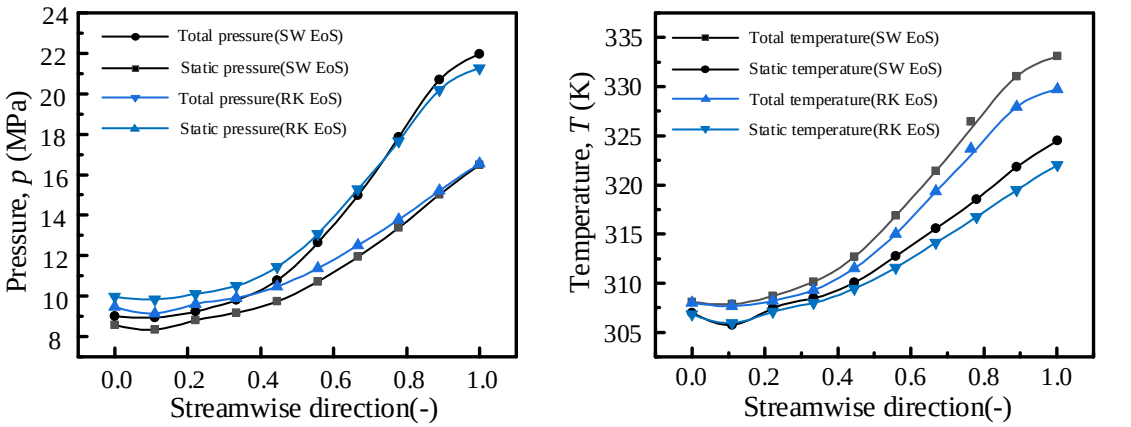

(a) Pressure change in streamwise direction (b) Temperature change in streamwise direction

Figure 12 Schematic diagram of the temperature and pressure changes of the compressor in the streamwise direction calculated by two different EoSs

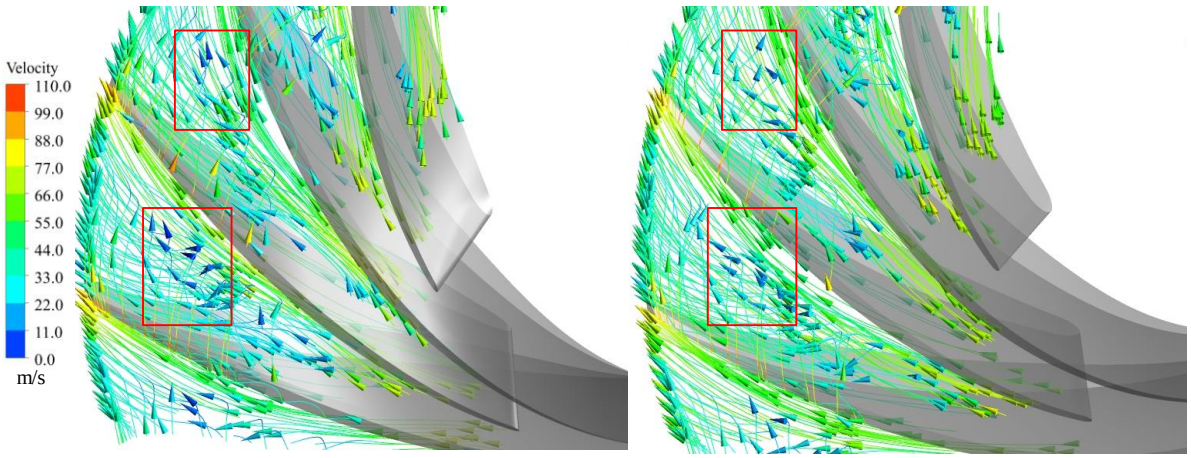

(a) Streamline distribution of impeller passages with RK EoS (b) Streamline distribution of impeller passages with SW EoS

Figure 13 The streamline distribution of compressor impeller passages based on two different CO_2 real gas EoSs

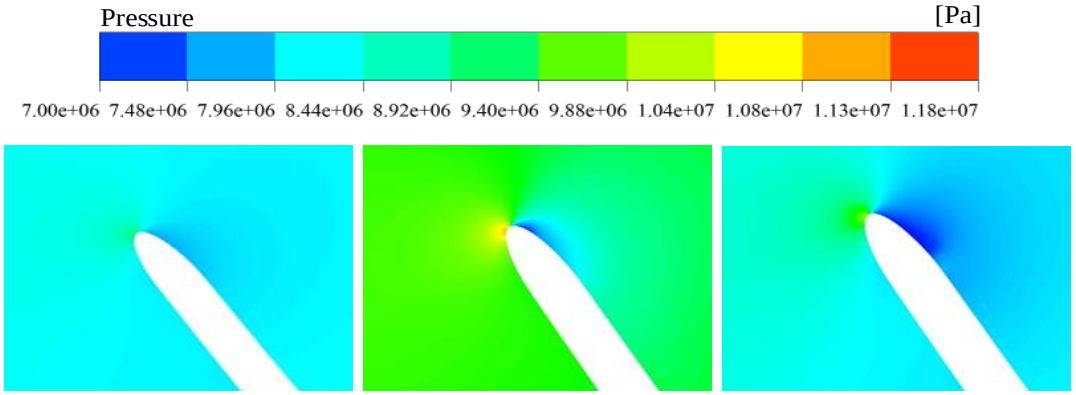

(a) Blade leading edge with CO_2 ideal gas (b) Blade leading edge with RK EoS (c) Blade leading edge with SW EoS

Figure 14 Schematic diagram of the pressure distribution on the leading edge of the blade at 80% span

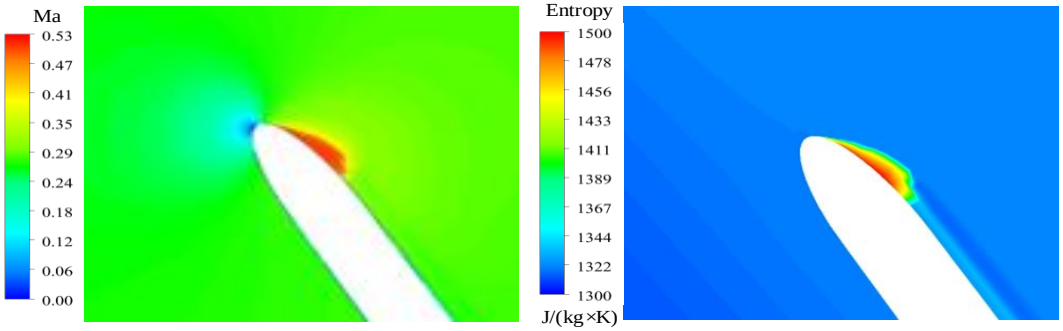

(a) Mach number (b) Entropy

Figure 15 Mach number and entropy contours at 80% span

5 Conclusion

This study explores the influence of three different gas EoSs on the steady-state simulation characteristics of SCO_2 centrifugal compressor, and the main conclusions are as follows:

(1) Analyzing the ideal gas simulation results, it can be seen that the performance is poor and can only work under a small mass flow rate. When applying ideal gas EoS, the simulated compressor working range is 1.8-4.8kg/s; the highest isentropic efficiency can only reach 88%; the highest pressure ratio is about 1.35. When the simulation result of the ideal gas is used as the initial condition of the real gas simulation, it will have a good effect.

(2) In this study, the external RGP tables were combined with the computational fluid dynamics solver. Through the independent study of the RGP table resolution, a table with 400 × 400 is selected to carry out the following simulations. The drastic change of CO_2 thermodynamic properties near the critical point has a certain impact on the stability and convergence characteristics of the numerical simulations. By the stability analysis, it can be found that as the RGP table resolution and simulated rotational speed increase, the possibility of simulation divergence increases.

(3) By analyzing and comparing the effects of two real gas EoS on the simulated performance and flow field of SCO^2 centrifugal compressors, it is found that the RK EoS has certain errors in the calculation of physical properties near the critical point. In the front half of the flow passage of the impeller, especially the position of the leading edge of the blade, some phenomena in the flow field based on RK EoS cannot be captured. Besides, the simulation based on RK EoS predicts a higher flow loss in the latter half of the blade.

Conflict of Interest: The authors declare that there is no conflict of interest regarding the publication of this paper.

Acknowledgments: Funding data: National Natural Science Foundation of China (Grant No: 52106049); Natural Science Foundation of Shandong Province (ZR2020QE191); Natural Science Foundation of Jiangsu Province (BK20210113); The Young Scholars Program of Shandong University (31380089964175).

Appendix A.

CO_2RK EoS:

$$p = \frac{RT}{V - e + c} - \frac{\alpha(T)}{V(V+e)} \tag{1}$$

$$\alpha(T) = d\left(\frac{T_c}{T}\right)^n \tag{2}$$

$$c = \frac{RT_c}{p_c + d/(V_c^2 + V_c \cdot e)} + e - V_c \tag{3}$$

$$n = 0.4986 + 1.1735w + 0.4754w^2 \tag{4}$$

$$d = 0.42747 R^2 T_c^2 / p_c \tag{5}$$

$$e = 0.08664 RT_c / p_c \tag{6}$$

$$R = \frac{R_u}{M_r} \tag{7}$$

In formula (4), d and e are constants, used to correct the intermolecular gravitation and correct the volume respectively. A fourth-order polynomial was used for the calculation to ensure simulation accuracy.

CO_2SW EoS:

$$\frac{f(\rho,T)}{R_g T} = \phi(\delta,\tau) = \phi^0(\delta,\tau) + \phi^r(\delta,\tau) \tag{8}$$

In formula (11), ϕ is the Helmholtz free energy nondimensionalized by the gas constant and temperature. δ and τ are the reciprocals of the relative density and relative temperature respectively. The relative value here is relative to the critical point. ϕ^0 and ϕ^r represent the ideal part and the remaining part of the physical properties of CO_2, respectively.

$$\phi^0(\delta,\tau) = \ln(\delta) + a_1^0 + a_2^0\tau + a_3^0\ln(\tau) + \sum_{i=4}^{8} a_i^0 \ln(1 - e^{-\tau\theta_i^0}) \tag{9}$$

Where a_i^0 and θ_i^0 are the parameters of the ideal part.

$$\phi^r = \sum_{i=1}^{7} n_i \delta^{di} \tau^{ti} + \sum_{i=8}^{34} n_i \delta^{di} \tau^{ti} e^{-\tau c_i} + \sum_{i=35}^{39} n_i \delta^{di} \tau^{ti} e^{-\alpha_i(\delta-\epsilon_i)^2 - \beta_i(\tau-\gamma_i)^2} + \sum_{i=40}^{42} n_i \Delta^{bi} \delta e^{-C_i(\delta-1)^2 - D_i(\tau-1)^2} \tag{10}$$

In formula (13), α_i, β_i, γ_i, ϵ_i, t_i, c_i, b_i, C_i, D_i, and n_i are all the parameters of i≤39 in the remaining part. The improvement of the calculation accuracy of physical properties near the critical point by this equation is mainly derived from the last term in formula (13).

$$\Delta = \left\{ (1-\tau) + A_i[(\delta-1)^2]^{\frac{1}{2\beta_i}} \right\}^2 + B_i[(\delta-1)^2]^{a_i} \tag{11}$$

In formula (14), ai, βi, Ai, and Bi are all parameters of 39≤i≤42 in the remaining part, and they are all constants. In the SW EoS, other thermophysical parameters need to be calculated by Helmholtz free energy and its partial derivatives relative to temperature and density, such as pressure, enthalpy, entropy, and so on.

References

[1] Jia-Qi Guo, Ming-Jia Li, Jin-Liang Xu,et al. Energy, exergy and economic (3E) evaluation and conceptual design of the 1000 MW coal-fired power plants integrated with S-CO_2 Brayton cycles[J]. Energy Conversion and Management,2020,211.

[2] Vaclav Dostal, Pavel Hejzlar, Michael J Driscoll. High-Performance Supercritical Carbon Dioxide Cycle for Next-Generation Nuclear Reactors[J]. Nuclear Technology,2006,154(3).

[3] Eduardo Ruiz-Casanova, Carlos Rubio-Maya, J Jesús Pacheco-Ibarra,et al. Thermodynamic analysis and optimization of supercritical carbon dioxide Brayton cycles for use with low-grade geothermal heat sources[J]. Energy Conversion and Management,2020,216.

[4] Qi Jian-hui, Reddell Thomas, Qin Kan,et al. Supercritical CO_2 Radial Turbine Design Performance as a Function of Turbine Size Parameters[J]. Journal of Turbomachinery,2017,139.

[5] Xu-rong Wang, Yi-ping Dai. Exergoeconomic analysis of utilizing the transcritical CO 2 cycle and the ORC for a recompression supercritical CO_2 cycle waste heat recovery: A comparative study[J]. Applied Energy,2016,170.

[6] Vaclav Dostal, Pavel Hejzlar, Michael J. Driscoll. The Supercritical Carbon Dioxide Power Cycle: Comparison to Other Advanced Power Cycles[J]. Nuclear Technology,2006,154.

[7] Nikola D. Baltadjiev, Claudio Lettieri, Zoltan S. Spakovszky. An Investigation of Real Gas Effects in Supercritical CO_2 Centrifugal Compressors[J]. Journal of Turbomachinery,2015,137(9).

[8] Zhi-yuan Liu, Weiwei Luo, Qing-jun Zhao,et al.Preliminary Design and Model Assessment of a Supercritical CO_2 Compressor[J]. Applied Sciences,2018,8(4).

[9] Darryn Fleming, Thomas Holschuh, Tom Conboy,et al. Scaling Considerations for a Multi-Megawatt Class Supercritical CO_2 Brayton Cycle and Path Forward for Commercialization[C]. Copenhagen, DENMARK: ASME Turbo Expo 2012.

[10] Angelino G, Invernizzi C. Real Gas Brayton Cycles for Organic Working Fluids, Proceedings of the Institution of Mechanical Engineers, Part A: Journal of Power and Energy. 2001,215(1); pp. 27-28.

[11] Jekyoung Lee, Seungjoon Baik, Seong Kuk Cho,et al. Issues in performance measurement of CO_2 compressor near the critical point[J]. Applied Thermal Engineering,2016,94.

[12] Seong Gu Kim, Jekyoung Lee, Yoonhan Ahn,et al. CFD investigation of a centrifugal compressor derived from pump technology for supercritical carbon dioxide as a working fluid[J]. The Journal of Supercritical Fluids,2014,86.

[13] Bao Wen-rui, Yang Ce, Wang Wen-li,et al. Effect of inlet temperature on flow behavior and performance characteristics of supercritical carbon dioxide compressor[J]. Nuclear Engineering and Design,2021,380.

[14] ANSYS Academic Research, ANSYS CFX User Guide, Release 17.1, ANSYS, Inc, 2016

[15] Wright, Steven A, Lipinski,et al. Closed Brayton Cycle Power Conversion Systems for Nuclear Reactors: Modeling, Operations, and Validation. The United States,2006.

[16] Aungier R H. A Fast, Accurate Real Gas Equation of State for Fluid Dynamic Analysis Applications[J]. Journal of Fluids Engineering,1995, 117:277-281.

[17] Roland Span, Wolfgang Wagner. A New Equation of State for Carbon Dioxide Covering the Fluid Region from the Triple-Point Temperature to 1100 K at Pressures up to 800 MPa[J]. Journal of Physical and Chemical Reference Data,2009,25(6).

[18] Ameli Alireza, Afzalifar Ali, Turunen-Saaresti,et al Effects of Real Gas Model Accuracy and Operating Conditions on Supercritical CO_2 Compressor Performance and Flow Field[J]. Journal of Engineering for Gas Turbines and Power-Transactions of the ASME,2018,140(6).

[19] Michela Mazzoccoli, Barbara Bosio, Elisabrtta Arato. Analysis and Comparison of Equations-of-State with p-ρ-T Experimental Data for CO_2 and CO_2-Mixture Pipeline Transport[J]. Energy Procedia,2012,23: 274-283.

Viser Technology Pte. Ltd.
Mechanical Engineering Science
DOI: 10.33142/mes.v3i2.6727

Research Article Open Access

Process and Component Analysis on S-CO_2 Cooling Wall in the Coal-fired Boiler Power System

Yuanhong FAN, Danlei YANG, Guihua TANG*, Xiaolong LI

MOE Key Laboratory of Thermo-Fluid Science and Engineering, School of Energy and Power Engineering, Xi'an Jiaotong University, Xi'an 710049, China

***Corresponding Author:** Guihua TANG, E-mail: Guihua TANG ghtang@mail.xjtu.edu.cn*

Abstract:
The supercritical carbon dioxide (S-CO_2) cooling wall in coal-fired boiler suffers from severe fragile crisis due to the high temperature of S-CO_2. The analysis of both heat transfer at process scale and cooling wall arrangement at component scale were carried out in present work. At the process scale, the difference in heat transfer performance between the smooth tube and the rifled tube were identified, especially the location of maximum outer wall temperature of cooling wall. The 1-D mathematical model for thermal-hydraulic analysis of S-CO_2 furnace cooling wall tubes was then developed. At the component scale, the coupled model of combustion and S-CO_2 heat transfer is employed for studying the thermal-hydraulic performance of rifled-spiral (R-S) and smooth-spiral (S-S) cooling wall arrangements. The maximum outer wall temperature of R-S cooling wall is 16.38℃ lower while the pressure drop increases by 2.33 times compared with the S-S cooling wall. Considering the pressure drop penalty on cycle efficiency of S-CO_2 boiler power system, the R-S cooling wall is not recommended, while the S-S cooling wall should be carefully arranged in S-CO_2 boilers.

***Keywords:** thermal fragile; heat transfer; correlation; cooling wall arrangement; spiral*

Table 1 Prime table

	Nomenclatur	SCW	Supercritical water
Bo	Buoyancy parameter	T	Temperature (℃)
d	Inner diameter (mm)	U	Circumference (mm)
D	Outer diameter (mm)	x	Coordinate (mm)
f	Friction coefficient		Greek letters
g	Gravity acceleration (m • s^{-2})	α	Angle (°)
G	Mass flux (kg • m^{-2} • s^{-1})	δ	Thickness (mm)
h	Enthalpy (kJ • kg^{-1})	λ	Thermal conductivity (W • m^{-1} • K^{-1})
L	Length (mm)	ρ	Density (kg • m^{-3})
m	Mass flow (kg • s^{-1})	φ	View factor
Nu	Nusselt number		Subscripts
P	Pressure (MPa)	ave	Average
q	Heat flux (kW • m^{-2})	b	Bulk
r	Inner radius diameter (mm)	f	Friction
R	Outer radius diameter (mm)	in	Inlet
Re	Reynold number	iso	Isothermal
s	Pitch diameter (mm)	max	Maximum
S-CO_2	Supercritical carbon dioxide	w	Wall

1 Introduction

Due to its high efficiency [1] and compactness, the supercritical carbon dioxide (S-CO_2) Brayton cycle has been considered as one of the promising candidates in the coal-fired power conversion systems [2]. For the engineering design of S-CO_2 coal-fired power system,

Received on October 17, 2021; Accepted on December 12, 2021

one of the major issues lies in the thermal-hydraulic design of cooling wall in boilers, e.g. the prevention of thermal fragile and the circumferentially average heat transfer prediction for a single tube at the process scale, and the arrangement of the S-CO_2 cooling wall at the component scale.

Firstly, at the process scale, there exist restraints to the heat transfer for an actual S-CO_2 cooling wall tube: (1) circumferentially non-uniform heating condition, (2) large tube diameter (d), and (3) large mass flux (G). However, few work concerns the aforementioned issues [3]. The test parameters in typical experiments for the S-CO_2 heat transfer are presented in Table 2. We can see that the test tube diameter d is lower than 10 mm and the mass flux G is within a moderate range. Moullec et al. [4] designed the S-CO_2 cooling wall tube with d of 50-70 mm. In contrast, Xu et al. [5-6] suggested that although the tube with large d can theoretically alleviate the pressure drop in cooling wall, its reliability under such working conditions of high pressure and temperature cannot be ensured. Thus, a traditional range of 25-40 mm was recommended. Meanwhile, the large G in the S-CO_2 cooling wall was mainly caused by the low enthalpy difference of S-CO_2 in heaters in S-CO_2 power system [5]. Generally, the large G was accompanied with the large pressure drop [7], further leading to the reduction in cycle efficiency. Thus, aiming to solve this problem, some researchers employed the partial flow strategy [8-9] so that the G of S-CO_2 in cooling wall can be within a reasonable range of 1500-2500 kg m^{-2} s^{-1}.

Table 2 Experimental parameters in literature

Authors	*d*, mm	*P*, MPa	*G*, kg m^{-2} s^{-1}	*q*, kW m^{-2}
Tanimizu et al. [10]	8.7	7.5-9.0	185-285.97	16-64
Jiang et al. [11]	2	8.58-9.62	6.29-6.63	4.49-81
Liao et al. [12]	0.7-2.16	7.4-12	Re=(1-20) $\cdot 10^4$	10-200
Kim et al. [13]	4.5	7.46-10.26	208-874	38-234
Jiang et al. [14]	0.948-4	8.53-9.5	Re=1743-25011	2.593-108
Li et al. [15]	2	7.8-9.5	Re=3800-20000	6.50-51.96
Bae et al. [16]	6.32	7.75-8.12	285-1200	30-170
Gupta et al. [17]	8	7.4-8.8	900-3000	16-615

The smooth tube and the rifled tube are two dominant tube configurations in actual boilers [18–20]. However, the heat transfer of S-CO_2 in the rifled tubes are less concerned yet. Li et al. [21] studied the S-CO_2 inside the rifled tubes and suggested that the inner ribs can destroy the boundary layer to weaken the negative effects of buoyancy effect. Meanwhile, the heat transfer of supercritical water (SCW) inside the rifled tubes was investigated broadly, which would be helpful for understanding S-CO_2. Shen et al. [19] found a positive impact of inner ribs on the heat transfer of SCW. Gu et al. [22] found that the heat transfer of SCW is closely related to the ribs. Yang et al. [23] found a high flow resistance caused by the inner ribs. Whereas, note that all the above-mentioned works mainly focus on the heat transfer in the near-critical region. For the S-CO_2 cooling wall, the working conditions are far away from the critical point as T_{in} ＞ 450 ℃ and P_{in} ≈ 30 MPa. Moreover, as the scale of the cooling wall tube is much less than that of the combustion chamber, a simplified thermal-hydraulic tube model for predicting the maximum outer wall temperature and average outer wall temperature is essential to engineering design.

In addition to the thermal-hydraulic analysis of S-CO_2 at the process scale, the detailed analysis of S-CO_2 cooling wall arrangement is essential. Yang et al. [24] studied the 300 MW S-CO_2 boiler by a coupled simulation between the S-CO_2 heating and the combustion. Yang et al. [25], our previous work, provided both 1-D and 3-D coupled simulation of S-CO_2 cooling wall and proposed the "cold S-CO_2-hot fire matching and cascaded temperature control" method guiding the S-CO_2 cooling wall arrangement under partial flow strategy [5]. The method of S-CO_2 cooling wall arrangement in ref [25] was further proved with high reliability by Zhou et al. [7-8]. However, all the existing works for the S-CO_2 cooling wall are based on the smooth tube, and the rifled tube is not concerned. Moreover, the spiral cooling wall layout with the smooth or the rifled tube is widely used in the steam boiler, while the open literature concerning S-CO_2 cooling wall is limited to the vertical layout. Therefore, the spiral arrangement for both smooth and rifled cooling walls in S-CO_2 boiler needs to be examined, especially considering both thermal safety and pressure drop penalty on cycle efficiency.

The rest of the paper is organized as below. In Sec. 2, the three-dimensional numerical model for S-CO_2 heat transfer in both smooth tube and rifled tube and the coupled simulation method between S-CO_2 heating and combustion are demonstrated. The heat transfer performance is discussed in detail in Sec. 3. In Sec. 4, the arrangement of rifled-spiral R-S and smooth-spiral S-S cooling walls for S-CO_2 boiler is discussed. A brief conclusion is finally given in Sec. 5.

2 Numerical model and validation

2.1 3-D S-CO_2 heat transfer model inside smooth and rifled tubes

The numerical model of S-CO_2 flowing in smooth tube is quite similar to our previous work [26]. Firstly, the circular tubes made of stainless steel 316L were selected for the smooth tube and the rifled tube. The typical geometric parameters of the tubes are presented in Table 3. Particularly, the mesh of fluid region at the cross section for the rifled tube is presented in Figure 1. Four rectangular ribs with depth of 0.85 mm and width of 2.5 mm are arranged uniformly in the inner rifled tube. And the helix angle of the inner ribs is 30°. An additional isothermal section was also adopted in the present physical configuration. Secondly, the Shear Stress

Transport (SST) *k-ω* turbulent model was employed to solve the turbulent flow and heat transfer for S-CO_2. The model validation is shown in Figure 2 and a good agreement with available experimental data for both smooth and rifled tubes is found. Note that Figure 2a and Figure 2b stand for the high performance of SST *k-ω* turbulent model at near-critical region while Figure 2c further indicates a high reliability at the far-critical region. Thirdly, considering the non-uniform distribution of heat flux along the circumferential direction of the tube, the view factor of $\phi = q_{local} / q_{max}$ is adopted to model the non-uniform heat flux on the outer wall of tubes, as shown in Figure 3. Note that the view factor is calculated by a self-developed subroutine program in FLUENT based on the theoretical formulas in ref [27]. For the inner wall, the coupled thermal boundary condition and non-slip velocity boundary condition are utilized. Besides, the boundary conditions of the mass flow inlet and the pressure outlet are employed, as required by the NIST real gas model [28]. Finally, the grid independency is checked and the optimal grid numbers for smooth tube and rifled tube are 3.67 million and 4.89 million, respectively, as shown in Table 4.

Table 3 Geometric parameters of the smooth and rifled tubes

Tube	*d*/mm	*D*/mm	*s*/mm	L_{iso} / d_i	L_{heated} / d_i
Smooth tube	38	49.2	78	79	184
Rifled tube	38	49.2	78	79	184

Table 4 Grid independency test results

Tube	Total grid number/ $\times 10^6$	Mean relative error of Nu along the tube/ %
Smooth tube	1.37	-3.96
	2.29	-1.24
	3.08	1.67
	3.67	0.81
	4.36	0
Rifled tube	1.94	-2.64
	2.78	2.09
	3.67	1.13
	4.89	0.56
	5.91	0

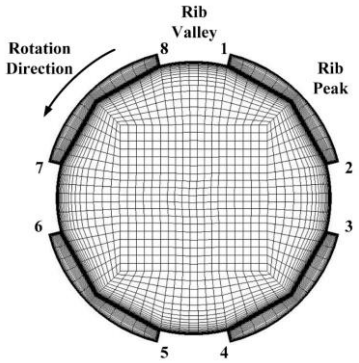

Figure 1 Cross section mesh of the rifled tube

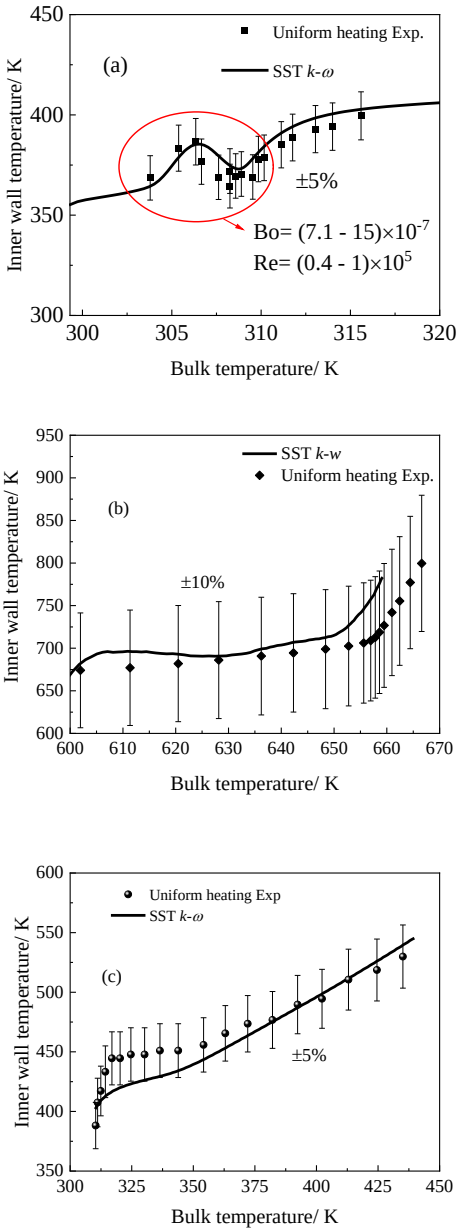

Figure 2 Comparisons between available experimental data and present predictions for (a) smooth tube [13], (b) rifled tube [23], and (c) smooth tube at far-critical region [29]

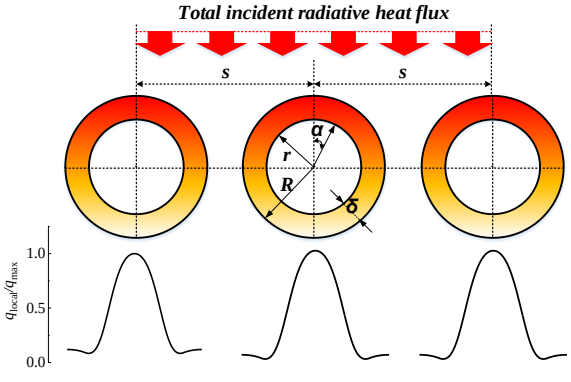

Figure 3 Non-uniform heat flux applied on the outer wall of tubes using the φ of q_{local} / q_{max}

2.2 1-D coupled simulation between S-CO_2 heating and combustion

The coupled model of combustion and S-CO_2 heat transfer for cooling wall was presented in our previous work [25], by which the thermal-hydraulic performance of cooling wall can be calculated. Firstly, the simulation of combustion of furnaces is essential for the coupled model, by which the wall furnace wall heat flux can be obtained for further S-CO_2 heat transfer calculation. Second, the 1-D S-CO_2 heat transfer model is used for cooling wall calculation. Finally, after the iteration of the two calculation processes, the maximum temperature and pressure drop of cooling wall tubes can be captured. More details about the coupled model can be found in [25]. In this work, we will use this coupled model to calculate the R-S and S-S cooling walls in S-CO_2 boiler.

3 S-CO_2 heat transfer in smooth and rifled tubes

The comparison of the heat transfer performance of S-CO_2 between the smooth tube and the rifled tube is shown in Figure 4. Note that the working conditions are based on the 1000 MW S-CO_2 coal-fired power system in ref [30]. A small difference in the inner circumferentially average heat transfer (characterized by $T_{w,inner,ave}$) is observed, indicating a negligible effect of inner ribs of rifled tubes on the circumferentially average heat transfer of S-CO_2. Meanwhile, the outer circumferentially average wall temperature ($T_{w,outer,ave}$) for the smooth tube tends to be a little higher than that of the rifled tube. This difference in $T_{w,outer,ave}$ means that the heat conduction in the solid regions cannot be ignored. Moreover, the localized maximum wall temperature in the inner wall ($T_{w,inner,max}$) of the smooth tube is almost identical to that of the rifled tube, while the localized maximum wall temperature in the outer wall ($T_{w,outer,max}$) of the smooth tube is slightly higher than that of the rifled tube.

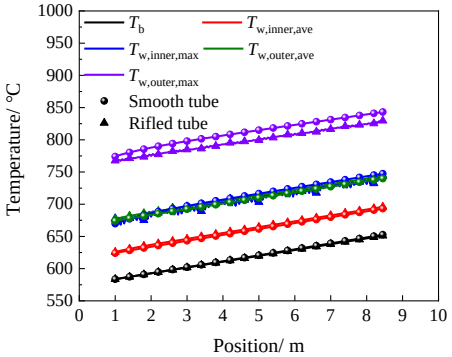

Figure 4 Comparison of heat transfer of S-CO_2 between smooth tube and rifled tube with T_{in} = 580 ℃, P_{in} = 35 MPa, q_{max} = 240 kW ṁ$^{-2}$ and G = 1800 kg ṁ$^{-2}$ s^{-1}

As shown in Figure 4, the bulk fluid temperature (T_b) and all the wall temperature almost increase linearly in the streamwise direction. Thus, the abnormal heat transfer phenomenon near the critical region does not occur at the working conditions of the S-CO_2 cooling wall. We take the distribution of the wall temperature and heat flux at 2.25 m as an example and compare the circumferential heat transfer between smooth tube and rifled tube in Figure 5. As shown in Figure 5a, both the inner wall temperature ($T_{w,inner}$) and the outer wall temperature ($T_{w,outer}$) of smooth tube show a smooth profile. In contrast, for the rifled tube, $T_{w,outer}$ shows a smooth profile, while $T_{w,inner}$ goes oscillating. This distinct distribution of $T_{w,inner}$ of rifled tube is mainly caused by the oscillating distribution of the localized heat flux on the inner wall (q_{inner}) of rifled tube, as shown in Figure 5b. Meanwhile, the smooth distribution of q_{inner} for smooth tube and the outer wall heat flux (q_{outer}) for both smooth and rifled tubes lead to the smooth distribution of the wall temperature in Figure 5a. Therefore, we can see a strong relation between the distribution of wall temperature and heat flux. Moreover, compared with the $T_{w,inner}$ of the smooth tube, the $T_{w,inner}$ of the rifled tube is more gentle since the difference between the maximum and the minimum $T_{w,inner}$ is smaller, as shown in Figure 5a. Besides, the maximum $T_{w,inner}$ in the smooth tube and the rifled tube are almost the same, while the maximum $T_{w,outer}$ of rifled tube is smaller than that of smooth tube.

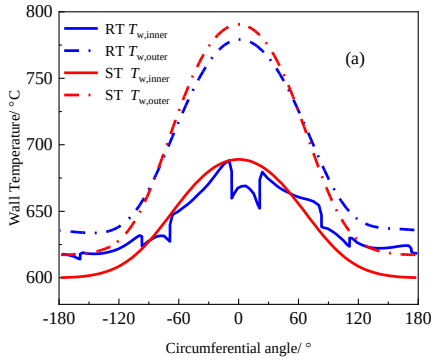

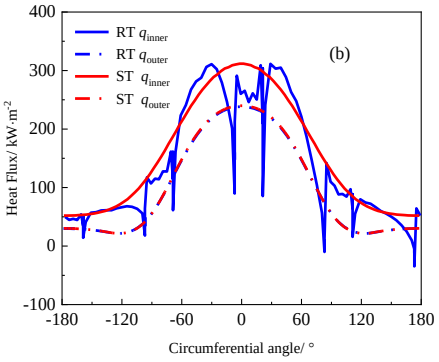

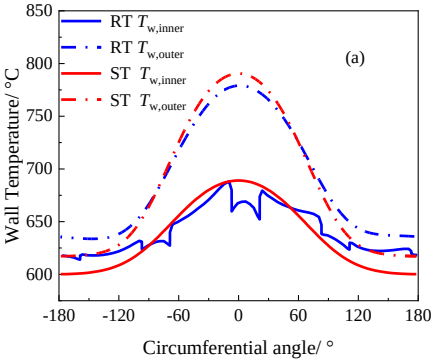

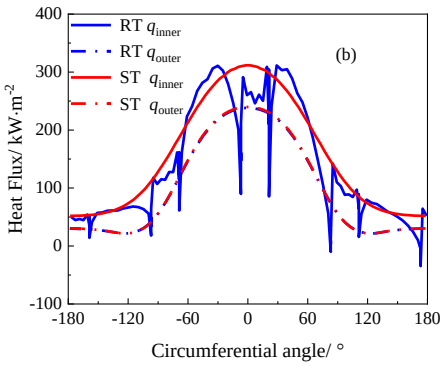

Figure 5 Circumferential distribution of (a) wall temperature and (b) heat flux on inner and outer walls for smooth tube and rifled tube in the streamwise direction of 2.25 m

$T_{w,outer,max}$ is the main concern in the analysis of thermal fragile of cooling wall. Generally, the distribution of $T_{w,outer}$ is closely related to $T_{w,inner}$. The circumferential distributions of $T_{w,inner,max}$ and $T_{w,outer,max}$ for rifled tube are further presented in Figure 6. As shown in Figure 6a, the $T_{w,inner,max}$ of rifled tube does not always occur at the heated top generatrix and shows a dispersive distribution, which is different from that of smooth tube. The $T_{w,inner,max}$ always locates near the left zone of the top generatrix. For this reason, the $T_{w,outer,max}$ of rifled tube also concentrates near the left of the top generatrix, but note that it is not that disperse as the $T_{w,inner,max}$.

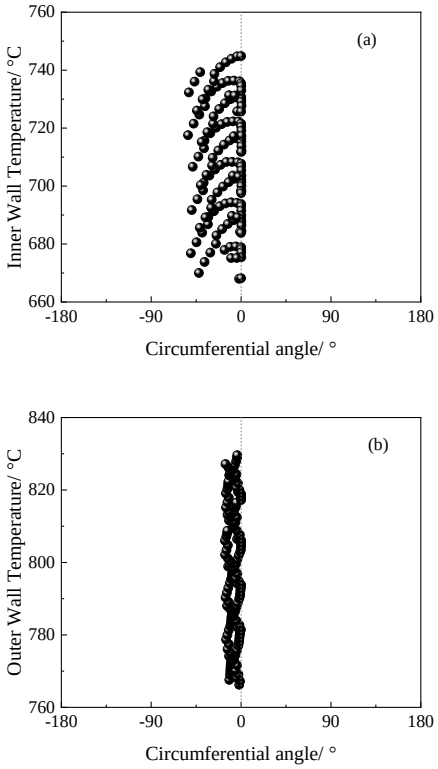

Figure 6 Circumferential distribution of (a) $T_{w,inner,max}$ and (b) $T_{w,outer,max}$ for rifled tube

To identify the relation between $T_{w,inner,max}$ and $T_{w,outer,max}$ of rifled tube, the effect of the ribs on the heat transfer of S-CO_2 in rifled tube is further discussed as shown in Figure 7. From Figure 7a, we can observe that the inner ribs lead to the rotating flow of S-CO_2, especially in the rib peak region. It indicates that the S-CO_2 in the rifled tube can be mixed more strongly than in the smooth tube. Thus, the $T_{w,inner}$ of the rifled tube can be more gentle than that of the smooth tube as shown in Figure 5a, further leading to the reduction in the maximum $T_{w,outer}$. From Figure 7b, we can observe that the points of $T_{w,inner,max}$ mostly concentrate at the intersection of rib valley and windward rib side close to the top generatrix. In contrast, the $T_{w,outer,max}$ in Figure 7c has a more even distribution. Thus, we can observe a stronger impact of heat conduction in the solid region than the inner convective heat transfer on the distribution of $T_{w,outer}$ for rifled tube.

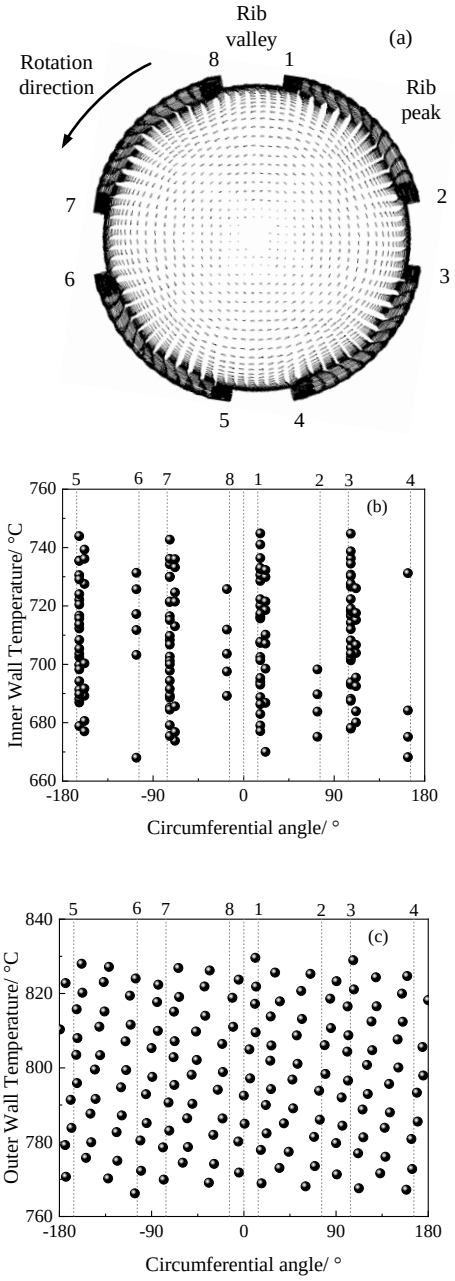

Figure 7 The impacts of inner rib distribution on the heat transfer of S-CO_2: (a) the rotating flow due to inner ribs and the distribution of (b) $T_{w,inner,max}$ and (c) $T_{w,outer,max}$

Based on the aforementioned discussion of the S-CO_2 flow and heat transfer, we find that both $T_{w,outer,max}$ and $T_{w,outer,ave}$ are closely related to the tube configuration (external diameter D and internal diameter d), pitch distance (S), tube solid thermal conductivity (λ_{solid}), total incident radiative heat flux value (q_{max}) and inner heat transfer coefficient (h). Thus, the empirical correlations are proposed according to the dimensional analysis method:

Smooth tube:

$$\begin{cases} T_{w,out,max} = T_b + 0.74\left(\frac{D}{S}\right)^{1.894}\left(\frac{d}{S}\right)^{-0.931}\left(\frac{Nu_{top}S\lambda_b}{d\lambda_{solid}}\right)^{-0.512}\left(\frac{q_{max}S}{\lambda_{solid}}\right) \\ T_{w,out,ave} = T_b + 0.967\left(\frac{D}{S}\right)^{2.470}\left(\frac{d}{S}\right)^{-1.648}\left(\frac{Nu_{ave}S\lambda_b}{d\lambda_{solid}}\right)^{-0.717}\left(\frac{q_{ave,out}S}{\lambda_{solid}}\right) \end{cases} \quad (1)$$

Rifled tube:

$$\begin{cases} T_{w,out,max} = T_b + 0.498\left(\frac{S}{d}\right)^{0.0338}\left(\frac{D}{d}\right)^{1.251}\left(\frac{Nu_{top}\lambda_b}{\lambda_{solid}}\right)^{-0.522}\left(\frac{q_{max}d}{\lambda_{solid}}\right) \\ T_{w,out,ave} = T_b + 2.34\left(\frac{S}{d}\right)^{-0.0183}\left(\frac{D}{d}\right)^{-1.787}\left(\frac{Nu_{ave}\lambda_b}{\lambda_{solid}}\right)^{-0.463}\left(\frac{q_{ave,out}d}{\lambda_{solid}}\right) \end{cases} \quad (2)$$

To determine the parameters along the cooling wall tube, the thermal-hydraulic correlations were incorporated into the 1-D mass, momentum and energy equations to develop the heat transfer prediction model. Firstly, the mass, momentum and energy conservation equations of the steady state S-CO_2 flow are solved.

Mass:

$$\frac{d\dot{m}}{dx} = 0 \quad (3)$$

Momentum:

$$\frac{dp}{dx} + \frac{dp_f}{dx} + \frac{\dot{m}^2}{A^2}\frac{d}{dx}\left(\frac{1}{\rho}\right) + \rho g = 0 \quad (4)$$

Energy:

$$\frac{dh}{dx} - \left(\frac{1}{\rho}\frac{dp}{dx} + \frac{1}{\rho}\frac{dp_f}{dx} + \frac{\int_U qdU}{\dot{m}}\right) = 0 \quad (5)$$

where p_f is the friction pressure drop. Secondly, the backward difference scheme was employed to approximate the derivatives in the conservation equations (Eqs. 3-5). The control volume of the 1-D S-CO_2 flow is shown in Figure 8. Finally, after obtaining the detailed parameters of S-CO_2 flowing inside the tube, $T_{w,outer,max}$ and $T_{w,outer,ave}$ can be calculated using Eqs. 1-2.

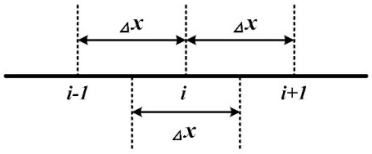

Figure 8 The 1-D S-CO_2 flow control volume

To validate the present model, we compared the S-CO_2 heat transfer results between the FLUENT 3-D simulation and the present 1-D model in Figure 9 and a good agreement is found. Therefore, the present 1-D model can be regarded as an efficient and accurate tool for the design of S-CO_2 furnace cooling wall.

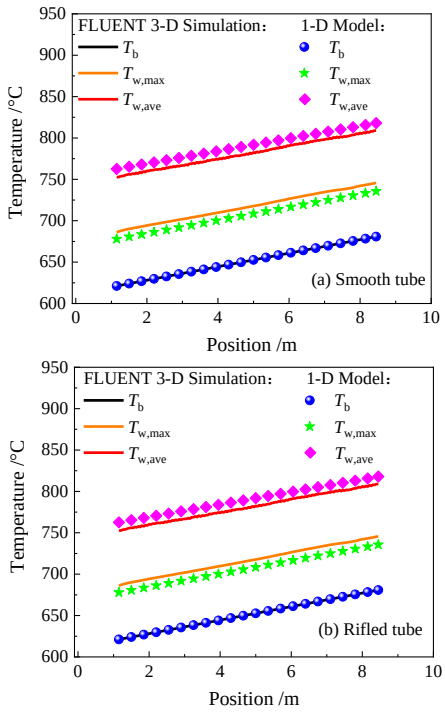

Figure 9 Comparison of temperature between FLUENT 3-D simulation and present 1-D model. (a) Smooth tube. (b) Rifled tube

4 R-S and S-S cooling wall arrangements for S-CO_2 boiler

The spiral cooling wall arrangement calculation is based on the coupled model of combustion and S-CO_2 heat transfer. In the coupled model, the cooling wall tube model can be set as smooth tube or rifled tube by changing the empirical correlations as shown in Eqs.1 and 2. To examine the R-S and smooth-spiral (S-S) cooling wall in 1000 MW S-CO_2 boiler, a traditional cooling wall arrangement in steam boiler is chosen, in which the integral spiral tubes cover the whole surface of the furnace wall without interruption. The inclination of spiral tube is 30 °. The thermal parameters of the cooling wall are presented in Table 5.

Table 5 Thermal parameters of the cooling wall

Cooling wall	Inlet temperature/℃	Inlet pressure /MPa	Mass flow/kg·s^{-1}
S-S and R-S	552.87	35.35	6320.09

The fluid temperature and maximum outer wall temperature distributions of R-S and S-S cooling walls are presented in Figure 10. First, we can see that the maximum outer wall temperature of R-S cooling wall is lower than that in S-S cooling wall. The maximum temperature difference is up to 16.38 ℃ in the tube outlet. The rifled tube can successfully reduce the maximum outer wall temperature. Second, the S-CO_2

fluid temperatures are quite similar inside both cooling walls due to the same heat load. Third, the profiles of maximum outer wall temperature show an obvious drop near 20 m in the furnace height direction, where the spiral cooling walls are going through the corner of the furnace and the wall heat fluxes are quite low due to the dual circle tangential firing in the furnace. In summary, the rifled tube can improve the thermal safety of the furnace.

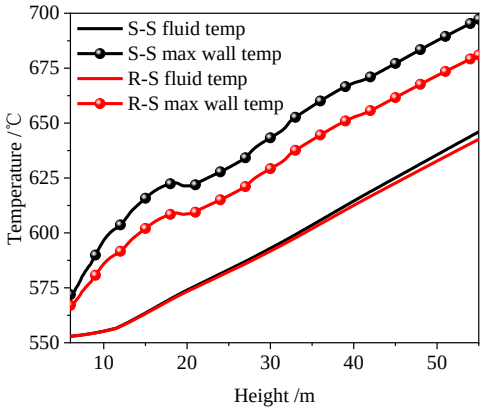

Figure 10 Fluid and maximum outer wall temperature distributions of R-S and S-S cooling wall in S-CO_2 boiler

In addition, the pressure drop penalty on cycle efficiency is essential for S-CO_2 boiler. Figure 11 shows the pressure drops of R-S and S-S cooling walls. Due to the large flow friction in the rifled tube, the pressure drop in R-S cooling wall increases by 2.33 times of that in S-S cooling wall, which will cause incredible penalty on cycle efficiency. Since the reduction in the cooling wall temperature by the rifled tube is not obvious either, it is not recommended in S-CO_2 boilers. Moreover, the pressure drop in S-S cooling wall is up to 4.10 MPa, which is extremely high. It is because we do not use the partial flow strategy and module design of the cooling wall [5]. According to the 1/8 principle [5] and 4 times of the cooling wall length, the present pressure drop of S-S cooling wall increases by 31 times of the result in our previous work [26] using partial flow strategy. Therefore, we can come to a conclusion that the S-S cooling wall should be carefully arranged in S-CO_2 boiler, while the R-S cooling wall is not recommended.

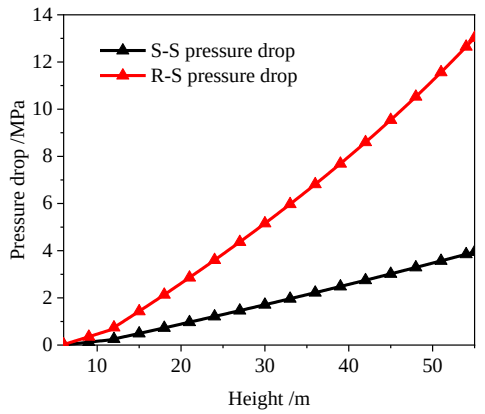

Figure 11 Pressure drops of R-S and S-S cooling walls in S-CO_2 boiler

5 Conclusions

The process and component analysis for the supercritical carbon dioxide (S-CO_2) cooling wall in coal-fired boiler was investigated, including the heat transfer performance and the S-CO_2 cooling wall arrangement. The main conclusions are as follows.

(1) The rifled tube is able to reduce the maximum outer wall temperature since it has a stronger mixing effect on S-CO_2 than the smooth tube under the non-uniform heating.

(2) The 1-D heat transfer prediction model coupled with the empirical correlations for S-CO_2 inside smooth tube and rifled tube is developed based on the 1-D steady state governing equations. A good agreement for S-CO_2 fluid flow and heat transfer prediction is found between the 1-D heat transfer prediction model and the 3-D FLUENT simulation.

(3) The coupled model of combustion and S-CO_2 heat transfer is employed for cooling wall arrangement. The maximum outer wall temperature of rifled-spiral cooling wall is 16.38 ℃ lower, while the pressure drop increases by 2.33 times compared with the smooth-spiral cooling wall. Considering both pressure drop penalty on the cycle efficiency of S-CO_2 boiler and the wall temperature reduction, the rifled-spiral cooling wall is not recommended in S-CO_2 coal-fired boilers. In addition, the smooth-spiral cooling wall should also be carefully arranged due to its extremely high pressure drop.

Author Contributions: G.H. Tang: Conceptualization, Investigation, Methodology, Funding acquisition, Project administration, Supervision, Writing – review & editing; Y.H. Fan: Formal analysis, Investigation, Methodology, Validation, Writing-original draft, Writing – review & editing; D.L. Yang: Formal analysis, Investigation, Methodology, Validation, Writing-original draft, Writing – review & editing; X.L. Li: Formal analysis.

Conflict of Interest: The authors declare that there is no conflict of interest regarding the publication of this paper.

Acknowledgments: This work was supported by the National Key Research and Development Program of China under grant number of 2017YFB0601803 and the National Natural Science Foundation of China under grant number of 51721004.

References

[1] Wang K, Li MJ, Zhang ZD, Min CH, Li P. Evaluation of alternative eutectic salt as heat transfer fluid for solar power tower coupling a supercritical CO_2 Brayton cycle from the viewpoint of system-level analysis. J Clean Prod 2021;279:123472. https://doi.org/10.1016/j.jclepro.2020.123472.

[2] Mecheri M, Le Moullec Y. Supercritical CO_2 Brayton cycles for coal-fired power plants. Energy 2016;103:758–71. https://doi.org/10.1016/j.energy.2016.02.111.

[3] Fan YH, Tang GH. Numerical investigation on heat transfer of supercritical carbon dioxide in a vertical tube under circumferentially non-uniform heating. Appl Therm Eng

2018;138:354–64. https://doi.org/10.1016/j.applthermaleng.2018.04.060.

[4] Le Moullec Y. Conceptual study of a high efficiency coal-fired power plant with CO_2 capture using a supercritical CO_2 Brayton cycle. Energy 2013;49:32–46. https://doi.org/10.1016/j.energy.2012.10.022.

[5] Xu J, Sun E, Li M, Liu H, Zhu B. Key issues and solution strategies for supercritical carbon dioxide coal fired power plant. Energy 2018;157:227–46. https://doi.org/10.1016/j.energy.2018.05.162.

[6] Liu C, Xu J, Li M, Wang Z, Xu Z, Xie J. Scale law of sCO_2 coal fired power plants regarding system performance dependent on power capacities. Energy Convers Manag 2020;226:113505. https://doi.org/10.1016/j.enconman.2020.113505.

[7] Zhou J, Zhu M, Xu K, Su S, Tang Y, Hu S, et al. Key issues and innovative double-tangential circular boiler configurations for the 1000 MW coal-fired supercritical carbon dioxide power plant. Energy 2020;199:117474. https://doi.org/10.1016/j.energy.2020.117474.

[8] Zhou J, Xiang J, Su S, Hu S, Wang Y, Xu K, et al. Key issues and practical design for cooling wall of supercritical carbon dioxide coal-fired boiler. Energy 2019;186:115834. https://doi.org/10.1016/j.energy.2019.07.164.

[9] Guo JQ, Li MJ, Xu JL, Yan JJ, Ma T. Energy, exergy and economic (3E) evaluation and conceptual design of the 1000 MW coal-fired power plants integrated with S-CO_2 Brayton cycles. Energy Convers Manag 2020;211:112713. https://doi.org/10.1016/j.enconman.2020.112713.

[10] Tanimizu K, Sadr R. Experimental investigation of buoyancy effects on convection heat transfer of supercritical CO_2 flow in a horizontal tube. Heat Mass Transf Und Stoffuebertragung 2016;52:713–26. https://doi.org/10.1007/s00231-015-1580-9.

[11] Jiang PX, Zhang Y, Xu YJ, Shi RF. Experimental and numerical investigation of convection heat transfer of CO_2 at supercritical pressures in a vertical tube at low Reynolds numbers. Int J Therm Sci 2008;47:998–1011. https://doi.org/10.1016/j.ijthermalsci.2007.08.003.

[12] Liao SM, Zhao TS. An experimental investigation of convection heat transfer to supercritical carbon dioxide in miniature tubes. Int J Heat Mass Transf 2002;45:5025–34.

[13] Kim DE, Kim MH. Experimental investigation of heat transfer in vertical upward and downward supercritical CO2 flow in a circular tube. Int J Heat Fluid Flow 2011;32:176–91. https://doi.org/10.1016/j.ijheatfluidflow.2010.09.001.

[14] Jiang PX, Xu YJ, Lv J, Shi RF, He S, Jackson JD. Experimental investigation of convection heat transfer of CO_2 at super-critical pressures in vertical mini-tubes and in porous media. Appl. Therm. Eng., vol. 24, 2004, p. 1255–70. https://doi.org/10.1016/j.applthermaleng.2003.12.024.

[15] Li ZH, Jiang PX, Zhao CR, Zhang Y. Experimental investigation of convection heat transfer of CO_2 at supercritical pressures in a vertical circular tube. Exp Therm Fluid Sci 2010;34:1162–71. https://doi.org/10.1016/j.expthermflusci.2010.04.005.

[16] Bae YY, Kim HY, Kang DJ. Forced and mixed convection heat transfer to supercritical CO_2 vertically flowing in a uniformly-heated circular tube. Exp Therm Fluid Sci 2010;34:1295–308. https://doi.org/10.1016/j.expthermflusci.2010.06.001.

[17] Gupta S, Saltanov E, Mokry SJ, Pioro I, Trevani L, McGillivray D. Developing empirical heat-transfer correlations for supercritical CO 2 flowing in vertical bare tubes. Nucl Eng Des 2013;261:116–31. https://doi.org/10.1016/j.nucengdes.2013.02.048.

[18] Li Z, Lu J, Tang G, Liu Q, Wu Y. Effects of rib geometries and property variations on heat transfer to supercritical water in internally ribbed tubes. Appl Therm Eng 2015;78:303–14. https://doi.org/10.1016/j.applthermaleng.2014.12.067.

[19] Shen Z, Yang D, Mao K, Long J, Wang S. Heat transfer characteristics of water flowing in a vertical upward rifled tube with low mass flux. Exp Therm Fluid Sci 2016;70:341–53. https://doi.org/10.1016/j.expthermflusci.2015.09.021.

[20] Li Z, Wu Y, Tang G, Zhang D, Lu J. Comparison between heat transfer to supercritical water in a smooth tube and in an internally ribbed tube. Int J Heat Mass Transf 2015;84:529–41. https://doi.org/10.1016/j.ijheatmasstransfer.2015.01.047.

[21] Li Z, Tang G, Wu Y, Zhai Y, Xu J, Wang H, et al. Improved gas heaters for supercritical CO_2 Rankine cycles: Considerations on forced and mixed convection heat transfer enhancement. Appl Energy 2016;178:126–41. https://doi.org/10.1016/j.apenergy.2016.06.018.

[22] Gu J, Zhang Y, Wu Y, Li Z, Tang G, Wang Q, et al. Numerical study of flow and heat transfer of supercritical water in rifled tubes heated by one side. Appl Therm Eng 2018;142:610–21. https://doi.org/10.1016/j.applthermaleng.2018.07.017.

[23] Yang D, Pan J, Zhou CQ, Zhu X, Bi Q, Chen T. Experimental investigation on heat transfer and frictional characteristics of vertical upward rifled tube in supercritical CFB boiler. Exp Therm Fluid Sci 2011;35:291–300. https://doi.org/10.1016/j.expthermflusci.2010.09.011.

[24] Yang Y, Bai W, Wang Y, Zhang Y, Li H, Yao M, et al. Coupled simulation of the combustion and fluid heating of a 300 MW supercritical CO_2 boiler. Appl Therm Eng 2017;113:259–67. https://doi.org/10.1016/j.applthermaleng.2016.11.043.

[25] Yang DL, Tang GH, Fan YH, Li XL, Wang SQ. Arrangement and three-dimensional analysis of cooling wall in 1000 MW S–CO_2 coal-fired boiler. Energy 2020;197:117168. https://doi.org/10.1016/j.energy.2020.117168.

[26] Fan YH, Yang DL, Tang GH, Sheng Q, Li XL. Design of S–CO_2 coal-fired power system based on the multiscale analysis platform. Energy 2021;240:122482. https://doi.org/10.1016/J.ENERGY.2021.122482.

[27] Duda P, Taler J. A new method for identification of thermal boundary conditions in water-wall tubes of boiler furnaces. Int J Heat Mass Transf 2009;52:1517–24. https://doi.org/10.1016/j.ijheatmasstransfer.2008.08.013.

[28] E.W. Lemmon, M.L. Huber, M.O. McLinden. Reference fluid thermodynamic and transport properties (REFPROP) 2007.

[29] Kline N, Feuerstein F, Tavoularis S. Onset of heat transfer deterioration in vertical pipe flows of CO_2 at supercritical pressures. Int J Heat Mass Transf 2018;118:1056–68. https://doi.org/10.1016/j.ijheatmasstransfer.2017.11.039.

[30] Sun E, Xu J, Li M, et al. Connected-top-bottom-cycle to cascade utilize flue gas heat for supercritical carbon dioxide coal fired power plant. Energy Convers Manag 2018;172:138–54. https://doi.org/10.1016/j.enconman.2018.07.017.

Viser Technology Pte. Ltd.
Mechanical Engineering Science
DOI: 10.33142/mes.v3i2.6728

Research Article Open Access

Influence of Recirculated Flue Gas Distribution on Combustion and NOx Formation Characteristics in S-CO_2 Coal-fired Boiler

Peipei WANG, Mingyan GU*, Yao FANG, Boyu JIANG, Mingming WANG, Ping CHEN

School of Energy and Environment, Anhui University of Technology, Ma'anshan, 243002, China

***Corresponding Author:** Mingyan Gu, Ma'anshan, 243002, China, gumy@ahut.edu.cn*

Abstract:
Supercritical carbon dioxide (S-CO_2) Brayton power cycle power generation technology, has attracted more and more scholars' attention in recent years because of its advantages of high efficiency and flexibility. Compared with conventional steam boilers, S-CO_2 has different heat transfer characteristics, it is easy to cause the temperature of the cooling wall of the boiler to rise, which leads to higher combustion gas temperature in the furnace, higher NO_X generation concentration. The adoption of flue gas recirculation has a significance impact on the combustion process of pulverized coal in the boiler, and it is the most effective ways to reduce the emission of NO_X and the combustion temperature in the boiler. This paper takes 1000MW S-CO_2 T-type coal-fired boiler as the research target to investigate the combustion and NO_X generation characteristics of S-CO_2 coal-fired boilers under flue gas recirculation condition, the influence of recirculated flue gas distribution along the furnace height on the characteristics of NO_X formation and the combustion of pulverized coal. The results show that the recirculated flue gas distribution has the great impact on the concentration of NO_X at the boiler outlet. When the bottom recirculation flue gas rate is gradually increased, the average temperature of the lower boiler decreases and the average temperature of the upper boiler increases slightly; The concentration of NOx at the furnace outlet increases.

***Keywords:** S-CO_2 boiler; Pulverized coal combustion; NO_X emission; Flue gas recirculation; Recirculated flue gas distribution*

1 Introduction

In 2020, China's CO_2 emissions reached about 9.894 billion tons, with the power industry being the largest source of carbon emissions. With the proposal and advancement of the carbon peaking and carbon neutrality goals, it is necessary to raise the efficiency of coal-fired systems power generation to reduce CO_2 emissions from coal-fired systems power generation. In recent years, China has vigorously developed clean renewable energy power generation, such as solar energy and wind power. However, the peak shaving effect of thermal power also makes a significant contribution in ensuring China's power system safety.

The traditional coal-fired boiler uses water vapor as the working medium, the power generation efficiency can reach 47%. Continuing to improve the efficiency of power generation will make a higher demand on the material of the cooling wall, thereby greatly increasing the cost of power generation [1]. Previous studies have found that for the traditional steam boiler 33MPa/620℃ ultra-supercritical unit, if the power generation efficiency is further improved from 47%, the boiler water wall temperature should reach 700℃. The expense of boiler materials will increase greatly. Therefore, countries all over the world are actively trying to increase technological innovation and explore new roads to raise the productivity of coal-fired boilers [2-3]. Many scholars have great interest in Supercritical carbon dioxide (S-CO_2) Brayton power cycle power generation technology. It has attracted people's attention because of its many advantages, such as compact system structure, high cycle efficiency and low cooling pipe corrosion. In recent years, more and more research results on S-CO_2 coal-fired power generation systems have continued to emerge at home and abroad, including the design optimization of Brayton cycle system, the structure of the boiler furnace, the heat transfer surface and the cooling wall arrangement, etc. [4-6]. And in-depth studies on cooling wall layout, combustion heat transfer characteristics and the layout of the internal heat exchange tubes of S-CO_2 boiler combined with coal-fired power generation have also been rapidly carried out [7-9].

Moullec et al have developed various conceptual designs of S-CO_2 coal-fired cycle systems with a power generation efficiency of 47.8% [10-11], while the maximum power generation efficiency of steam coal-fired boilers

Received on October 26, 2021; Accepted on December 16, 2021

with the same capacity is 45.4%. Zhang et al [12] have designed several S-CO_2 Brayton cycle coal-fired boilers. The research results indicate that compared with boilers with the same parameters, for the system parameters of 31 MPa/ 600 ℃/ 620 ℃, the maximum power generation efficiency can be increased from 45.96% to 50.71%. Zhou et al also have carried out the optimization design of the S-CO_2 Brayton cycle, and realized that the energy efficiency of 1000MW S-CO_2 coal-fired power plant was increased to 45.4% under the maximum operating parameter of 605 ℃/603/274 bar, which was about 3.5% higher than that of traditional ultra-supercritical units [13].

However, previous studies have found that, compared with traditional furnace, S-CO_2 with a higher temperature enters the boiler, so the entire cooling wall in the furnace has a higher temperature accordingly, then the local high temperature zone of combustion will cause the temperature of the water wall to rise more than 700 ℃ [14-17], which will significantly affect the NO_X generation and the combustion of pulverized coal in the furnace. Local over-temperature of water wall in S-CO_2 coal-fired boilers will also affect its operating efficiency.

Flue gas recirculation can effectively reduce the formation of NO_X, and is also an effective way in reducing the local high temperature in furnace. Zhou et al [18] have proposed the method of combining flue gas recirculation and expanding the size of furnace, which can increase the heat transfer area while ensuring the pulverized coal ignition and combustion, to achieve stable combustion and avoid local over-temperature of the cooling wall. Because of the complex combustion process of pulverized coal in the boiler, the aerodynamic and combustion characteristics in the furnace will be changed after flue gas recirculation, which will directly affect the NO_X generation characteristics in the furnace. There are many ways to inject circulating flue gas into the furnace, such as injecting it after mixing it with air or setting up a flue gas injection inlet separately. All these ways would have different effects on the process of pulverized coal combustion.

In order to investigate the combustion characteristics of S-CO_2 coal-fired boilers and control the generation and emission of NO_X, this paper takes T-type 1000MW S-CO_2 coal-fired boiler as the research object [19], and analyze in detail the influence of the distribution ratio of recirculating flue gas injected into the furnace at different positions on the characteristics of combustion and the generation of NO_X in the boiler to provide theoretical basis and guidance for the structural design and optimal combustion of S-CO_2 coal fired boilers and realization of low emissions of NO_X.

2 1000 MW T-type S-CO_2 Boiler Parameters

The boiler structure adopted in this paper is shown in Figure 1. It is divided into cold ash hopper, small furnace chamber, large furnace chamber and horizontal flue area. Since this paper focuses on the pulverized coal combustion characteristics and generation of NOx in the boiler, the effects of super-heater and re-heater in the horizontal flue are not considered in the simulation process, and the air preheater and economizer are also ignored. The total height of the boiler is 71.56m, the height of the cold ash hopper is 10.189m, the size of the small furnace chamber is 23.961m × 34.22m×15.67m, the height of the transition section of the large and small furnace chambers is 4m, and the size of the large chamber is 16.01m × 41.06m × 18.8m.

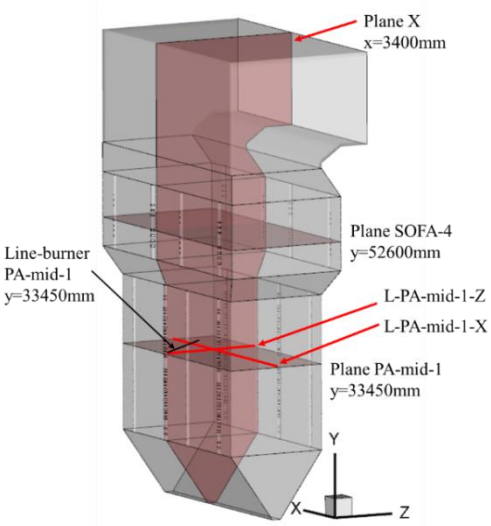

(a) The S-CO_2 boiler structure

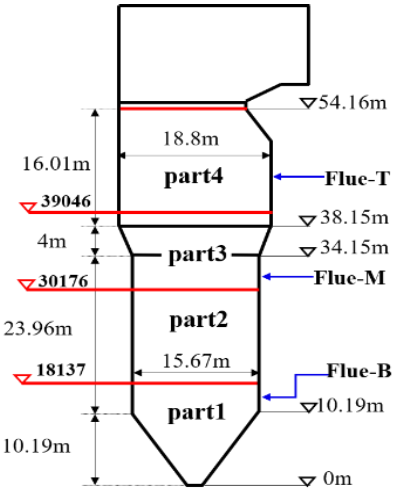

(b) The partition layout of boiler cooling wall

Figure 1 Schematic configuration of 1000MW T-type S-CO_2 boiler

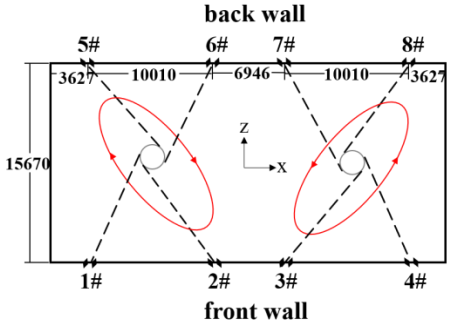

Figure 2 The arrangement of the burner nozzles in 1000MW S-CO_2 boiler

The arrangement of the burner nozzles on the

horizontal section is shown in Figure 2. The arrangement of burners is designed as a reverse double tangential circle combustion system with a total of 8 columns of burners arranged on the front and rear walls of the furnace, each column includes flue gas recirculation nozzles, over-fire air nozzles, secondary air nozzles, primary air nozzles. All air and pulverized coal are sprayed vertically along the nozzle to form two reverse double tangent circles.

The specific positions of flue gas recirculation nozzles, over-fire air nozzles, secondary air nozzles and primary air nozzles on the furnace wall are shown in Figure 3. As can be seen from Figure 1, the main combustion zone of the boiler is divided into upper and lower parts. There are 18 layers of primary air nozzles in total, divided into two layers. 8 layers are set in the upper main area of combustion, 10 floors are set in the lower main area of combustion. There are 12 layers of secondary air nozzles, and the upper and lower parts of the main combustion area have 6 layers each. The secondary air nozzles at the top and bottom of the upper and lower main combustion zones is half of the area of other secondary air nozzles. The secondary air nozzles and the primary air nozzles are arranged alternately. Two layers of bottom flue gas recirculation nozzles are arranged below the secondary air nozzles in the main combustion zone, and two layers of middle flue gas recirculation air nozzles are also arranged above the main combustion zone. Above the middle flue gas recirculation air nozzles, 4 layers of over-fire air nozzles and 3 layers of top flue gas recirculation air nozzles are arranged.

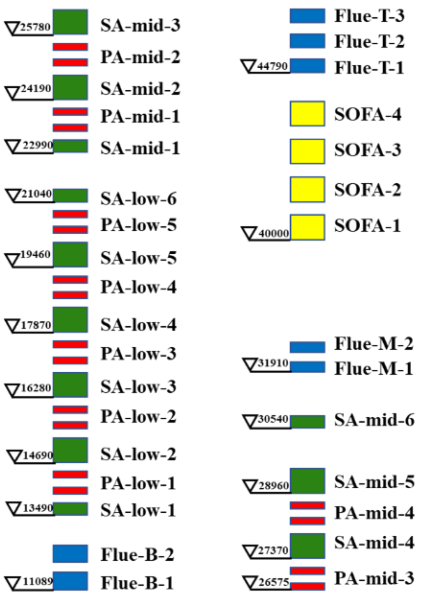

Figure 3 Burner nozzle distributions along the height of the furnace

3 Mathematical Model and Simulation Parameters

3.1 Numerical Models

The general control equation for three-dimensional steady-state turbulent heat and mass transfer commonly used for numerical calculations of flow and heat transfer is in the form of [20-21]:

$$\frac{\partial(\rho u\varphi)}{\partial x}+\frac{\partial(\rho v\varphi)}{\partial y}+\frac{\partial(\rho w\varphi)}{\partial z}=\frac{\partial}{\partial x}(\Gamma\frac{\partial\varphi}{\partial x})+\frac{\partial}{\partial y}(\Gamma\frac{\partial\varphi}{\partial y})+\frac{\partial}{\partial z}(\Gamma\frac{\partial\varphi}{\partial z})+S \quad (1)$$

In the formula: φ is a generic variable, which can represent velocity, temperature, component mass concentration, etc.; ρ is the generalized density; S is the generalized source term; Γ is the generalized diffusion coefficient.

The turbulent flow model is used to numerically simulate the turbulent flow in the S-CO_2 boiler furnace adopting the Realizable k-ε model. Particle moving model is adopted in particles random trajectory model. The radiation model uses the P_1 radiation model, and the absorption coefficient calculated by the WSGGM model. The coal volatilization analysis adopts a two parallel competitive reaction model to describe the volatilization rate. The uniform combustion of volatile matter of pulverized coal was calculated by finite rate/vortex dissipation model. The reaction rate of char depends on the diffusion rate of oxygen on the surface of char and the chemical kinetic rate calculated by the diffusion kinetic model. Thermal NO_X is simulated by extended Zeldovich Mechanism. For fuel-based NO_X calculations, HCN and NH_3 are currently widely accepted nitrogen-containing intermediates. The nitrogen in char generates NO_X in high-temperature combustion. The simultaneous reaction also includes the reduction of NO.

3.2 Simulation Conditions

In the simulation, the temperature of primary air powder is 593K, the temperature of secondary and over-fire air is 673K, and the temperature of circulating flue gas is 633k when flue gas recirculation is adopted. According to the conceptual design of the 1000MW S-CO_2 coal-fired boiler, the wall temperature is 50～100K higher than that of S-CO_2 working medium. Since the temperature of the working medium in each part of the water wall tube on the furnace wall does not change that much, the wall temperature of each part is set to be constant, and the average of inlet and outlet temperature of the working medium in each part of the water wall tube is added by 50K, and the emissivity of wall is 0.7. The parameters used are shown in below.

Table 1 1000MW S-CO_2 Coal-fired Boiler Operating Parameters

	Primary air ratio	Secondary air ratio	Over-fire air ratio
mass flow rate ratio (%)	19	56	25
the temperature of inlet (K)	593	695	695
Coal flowrate (t/h)		296.59	
excess air coefficient		1.2	

S-CO_2 temperature (K)	part1		part2		part3		part4	
	inlet	outlet	inlet	outlet	inlet	outlet	inlet	outlet
	796	852	796	852	835	883	837	884

Table 2 shows the composition analysis of bituminous coal. The size of pulverized coal particle is given according to rosin Rammler distribution and the detailed particle size data of bituminous coal are shown in the below.

Table 2 Composition analysis and diameter distribution of bituminous coal

Proximate analyses (%, ar)	Volatile	Fixed carbon	Ash	Moisture	
	26.27	49.38	8.8	15.55	
Ultimate analyses (%, ar)	C	N	H	O	S
	61.7	1.12	3.67		0.6
Calorific value of coal (kJ/kg, ar)			23400		
diameter distribution of pulverized coal (μm)	The minimum size		The maximum size		The mean size
	5		250		60

3.3 Solution Methods

The calculation problem between velocity and pressure is solved by SIMPLE algorithm and the first-order upwind scheme is used. It is considered that the simulation process converges when the absolute residual of several important parameters is less than 10^{-5}.

3.4 Grid Independence Test

Firstly, the grid independence test is carried out for four groups of grid domains: 3.53 million, 3.08 million, 2.61 million, 2.45 million. Figure 4 is a distribution of area-weighted average temperature with furnace height. The results shown that, there is no significant difference in temperature distribution between 3.08 million and 3.53 million grid cells. However, there is a great temperature differences between the main combustion regions of the 2.61 million and 3.08 million grids. And the simulation results presented are obtained with the grid domains of 3.08 million.

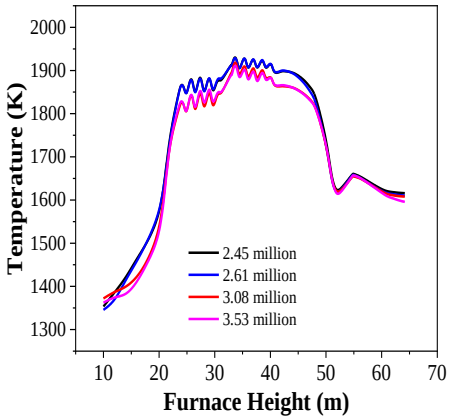

Figure 4 Area-Weighted Average Temperature Distribution with Furnace Height under Different Grid Systems

3.5 Model Validation

In order to further study the characteristics of pollutant emission and combustion of S-CO_2 coal-fired boiler, it is necessary to verify the numerical model. Because there are no S-CO_2 boiler entities and experiments, The development of steam boiler has been very mature. A traditional steam boiler with equal power is selected as experimental verification.

Table 3 Model verification results

	NO_X concentration (mg/m^3)	Burnout rate (%)	Outlet temperature (K)
Simulation results	307	98.9	1444
Measured value	272	98.8	
Simulation results from Literature [22]	270	98.8	1427

Table 3 shows the comparison between the numerical simulation results and the measured data, and the outlet NOx concentration as well as the burn rate are also given. Due to the different working fluids in the simulation and experiment, the concentration of NOx is also different. In the case of very low NOx concentrations, the predicted burn rate is consistent with the experimental date. The results show that the total relative error of the model is less than 10%, which verifies the reliability of the model. The simulation results are in good agreement with the measured data of the actual industrial steam boiler. Therefore, the simulation results of S-CO_2 coal-fired boilers are reasonable, indicating that the current models and methods can predict the flow, heat transfer, combustion and NOx generation characteristics of S-CO_2 boilers with good accuracy.

4 Results and Analysis

Recirculated flue gas is provided with three injection positions in the height direction of the furnace. The influence of recirculated flue gas distribution ratios on the characteristics of NOx generation and combustion of S-CO_2 coal-fired boiler with double furnace was studied when the flue gas recirculation rate was 27%. Table 4 shows the simulated conditions under different flue gas circulation distribution ratios.

The location of the cross sections intercepted in the data analysis of this chapter is shown in Figure 1.

Table 4 Simulation conditions under different recirculated flue gas distribution

	Flue gas circulation distribution ratios		
	Bottom flue gas nozzle	Middle flue gas nozzle	Top flue gas nozzle
Case 1	0%	45%	55%
Case 2	10%	40%	50%
Case 3	20%	35%	45%
Case 4	30%	30%	40%
Case 5	40%	25%	35%

4.1 The Distribution of Velocity

Figure 5 depicts the velocity distribution on the cross section in the furnace under different flue gas circulation distribution ratios. Through observation, it can be seen that the cold ash hopper to the horizontal flue, there is primary air, secondary air, over-fire air and circulating flue gas in turn. As can be seen from Figure 5(a), due to the double tangential combustion arrangement, two large symmetrical velocity zones appear in the over-fire air zone in the large furnace and the main combustion zone in the small furnace respectively. It can be observed from Figure 5(b) that the three high-speed zones respectively appear in the direction of the nozzles downward and those upward in the main combustion zone in the small furnace as well as the direction of the over-fire air nozzles. When the bottom recirculated flue gas increasing, the velocity in the lower main combustion zone in the small furnace increases, and the velocity in the over-fire zone in the large furnace and the upper main combustion zone in the small furnace decreases. It can be observed from Figure 5(c) that there are also two reverse tangential circles in the height direction of the furnace, and the velocity in the direction of airflow injection is higher. The results show that the high-speed zones are mainly distributed near the small furnace burner, while other areas such as cold ash hopper and the over-fire zone in the large furnace are low-speed zones.

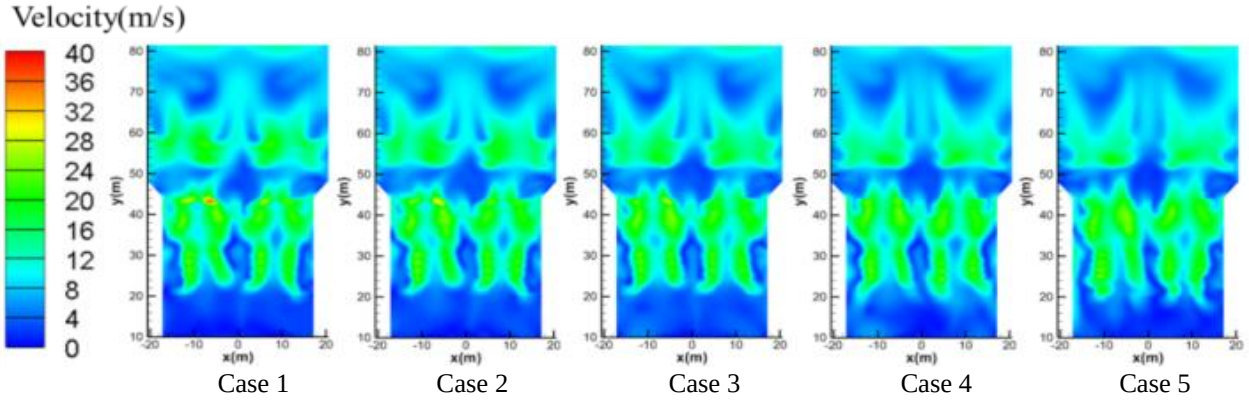

Case 1 Case 2 Case 3 Case 4 Case 5

(a) Gas velocity distributions (Z=0m)

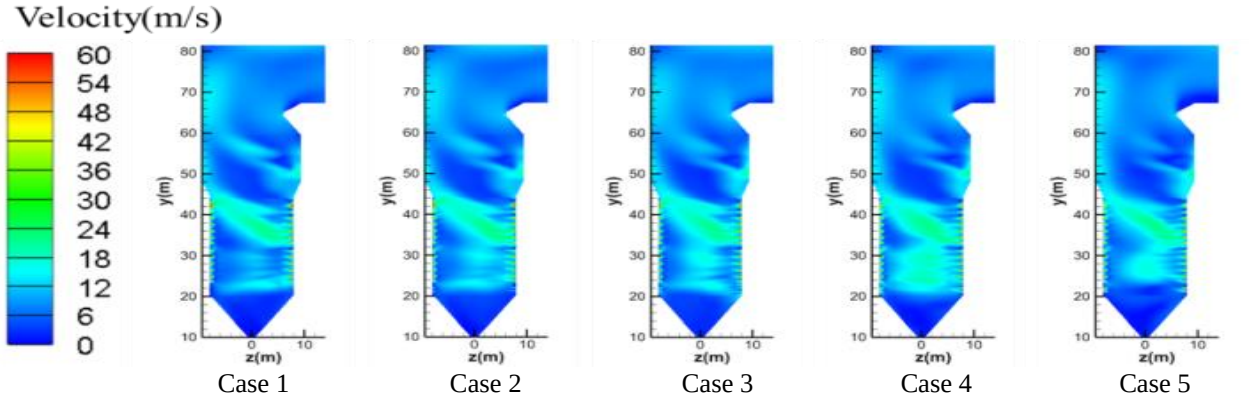

Case 1 Case 2 Case 3 Case 4 Case 5

(b) Gas velocity distributions (X=3.4m)

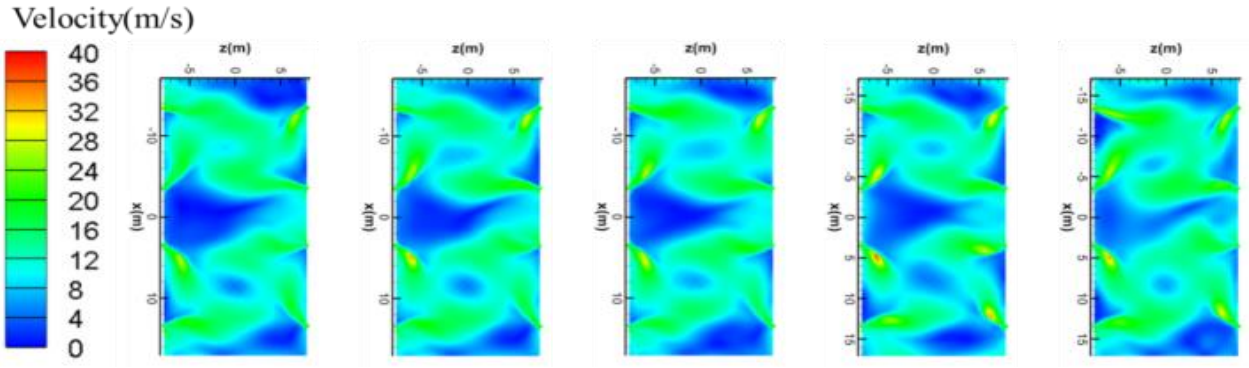

Case 1 Case 2 Case 3 Case 4 Case 5

(c) Gas velocity distributions (Y=33.45m)

Figure 5 Gas velocity distributions at different recirculated flue gas distribution

Figure 6 shows the variation of the average gas velocity along the furnace height at different recirculated-flue gas distributions. With the bottom recirculated-flue gas increasing, the flue gas flow rate

gradually increases at the bottom of the small furnace while the flue gas flow rate decreases in the large furnace. In the cold ash hopper region, the gas flow rate is relatively low. From the lower small furnace to the upper large one, the gas velocity gradually increases with the furnace height. For the lower small furnace, the gas velocity in the lower and upper burners tends to increase with furnace height in a fluctuating trend due to the combustion of pulverized coal. However, in the upper large furnace, because of the expansion of the cross-sectional size of the furnace, the gas velocity decreases again, and for the injection of a large amount of air from the over-fire air nozzles, the gas velocity increases with the furnace height.

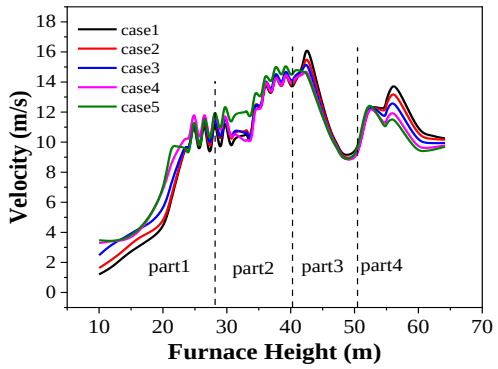

Figure 6 Area-weighted gas velocity along furnace height

4.2 Gas Temperature Distribution

The temperature distribution on different sections of the furnace under different flue gas circulation distribution ratios are shown in Figure 7. It can be seen that a high temperature zone in the furnace is mainly near the primary air nozzles, and the flame center is in the lower part of the main combustion area in the small furnace. With the increase of recirculated flue gas at the bottom flue gas nozzles, the gas temperature in the furnace gradually decreases. Especially the gas temperature in the cold ash hopper is extremely low. This is because the injection of recirculating flue gas increases the gas flow rate around the flue gas nozzles, which delay the ignition time of pulverized coal and increases the ignition distance. In addition, due to the high CO_2 concentration in the recirculating flue gas, the specific heat increases, which requires more heat. On the other hand, the recirculating flue gas reduces the oxygen concentration in the furnace and delays the ignition time, thus reducing the flame temperature near the burner. In addition, with the increase of recirculating flue gas volume at the bottom nozzles, the airflow velocity in the small furnace increases and the residence time of pulverized coal in the main combustion zone is shortened, thus weakening the combustion efficiency and intensity and reducing the burning temperature in the main combustion zone.

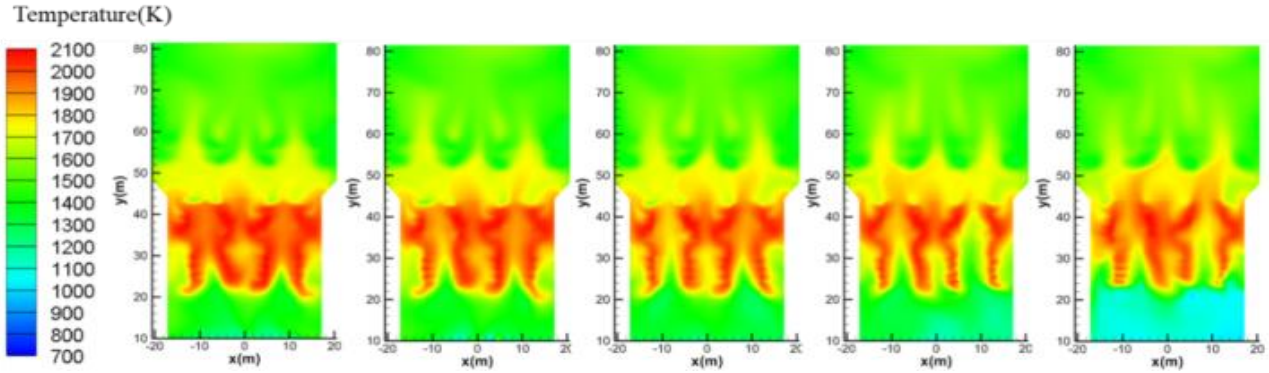

Case 1 Case 2 Case 3 Case 4 Case 5

(a) Gas temperature distributions (Z=0)

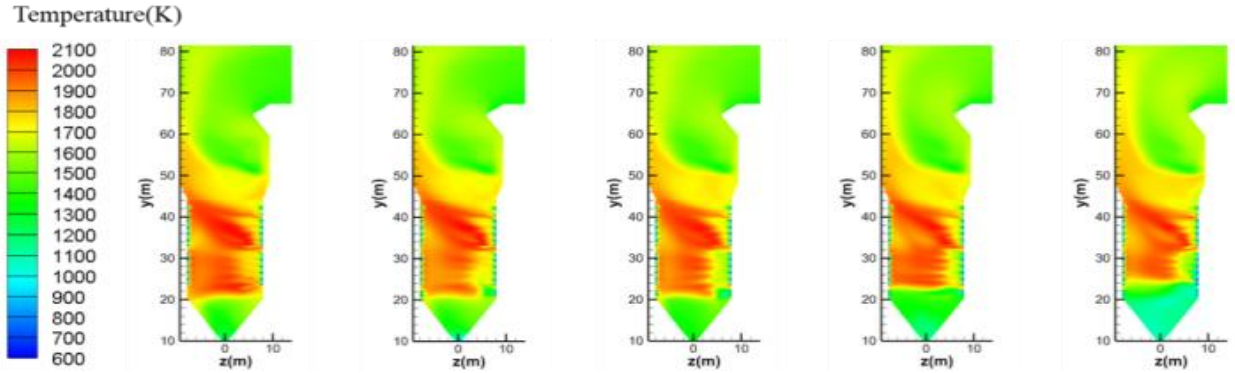

Case 1 Case 2 Case 3 Case 4 Case 5

(b) Gas temperature distributions (X=3.4m)

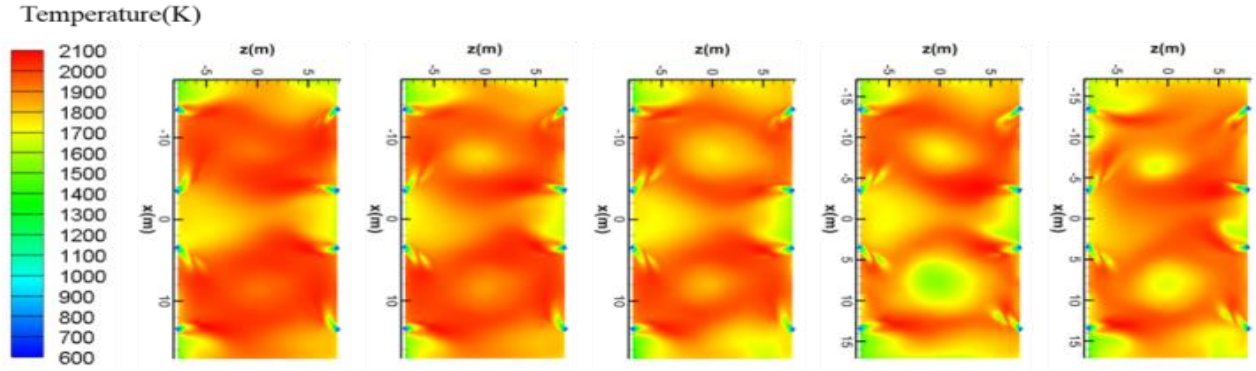

Case 1 Case 2 Case 3 Case 4 Case 5

(c) Gas temperature distributions (Y=33.45m)

Figure 7 Gas temperature distributions at different recirculated flue gas distribution

For the upper furnace area, the flue gas temperature is obviously low because the upper recirculating flue gas is injected above the over-fire air. In addition, the temperature distribution of each section is consistent with the velocity distribution. In the vicinity of the cold ash hopper, Near the cold ash hopper, the injected flue gas prevents pulverized coal from entering the cold ash hopper for combustion since the bottom flue gas nozzles are set below the bottom burner. Moreover, the recirculating flue gas alters the combustion conditions and the ignition and reduces the combustion intensity. Furthermore, the upward movement of the high-temperature gas also concentrates the combustion of pulverized coal in the center of the small furnace, thus further reducing the gas temperature in the cold ash hopper. A pattern of double tangential circles can be clearly seen from Figure 7(c). Since the pulverized coal is mainly burned in these areas, the temperature in the burner area is relatively high. In addition, the gas temperature in the small furnace is higher than that in the large furnace. When reaching the top of the burner area in the small furnace, the flue gas has the highest temperature. In the over-fire air zone, the gas temperature in the furnace is further reduced due to the injection of over-fire air.

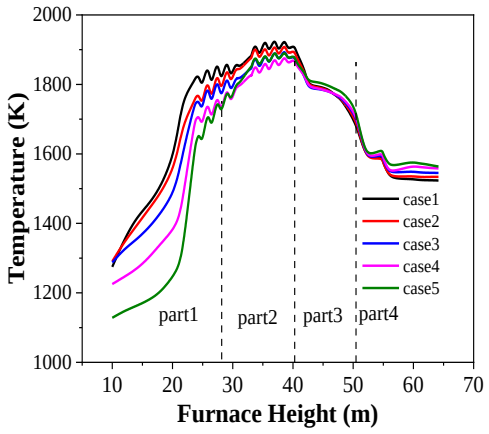

Figure 8 Area-weighted gas temperature distribution

Figure 8 shows the change of the average temperature of flue gas along the furnace height at different recirculated flue gas distribution ratios. The maximum temperature occurs in the main combustion area of the small furnace. In the case of S-CO_2 boiler, the physical properties of CO_2 are different from water. The temperature of the working medium in the S-CO_2 coal-fired boiler is higher, the heat transfer coefficient is lower than that of the steam boiler. When the pulverized coal is injected from the burner, under the action of the high-temperature airflow, the pulverized coal particles are rapidly heated. Due to flue gas circulation, the gas flow velocity in the furnace increases, and the upward movement of particles is more concentrated. In addition, the wall temperature of S-CO_2 boiler is about 200K higher than that of the steam boiler, and the higher wall temperature of Part3 of the S-CO_2 boiler is also one of the reasons for the higher temperature appeared near the Part3.

For different recirculated flue gas distributions, the overall trend of flue gas temperature distribution in the boiler is consistent, but for different areas, the temperature changes greatly. When the increase of the bottom flue gas circulation distribution ratio, the average temperature decreases in the small furnace and increases in the large furnace. This is because with the increase of the bottom flue gas circulation distribution ratio, the gas in the bottom circulating flue gas nozzles is injected with more CO_2. It has a higher specific heat, absorbs more heat and reduces the furnace temperature. When the circulating flue gas enters the furnace, due to the high specific heat of the cold flue gas, the combustion intensity of the pulverized coal is weakened, so the average temperature in the furnace is reduced as a whole, which strongly inhibits the generation of thermal NOx, and the high flue gas circulation distribution ratio at the bottom increases the circulating flue gas volume at the bottom, shortens the residence time of the pulverized coal, and slows down its ignition.

In the process of pulverized coal combustion, along the furnace height, the temperature distribution shows an increasing trend. With the continuous consumption of oxygen, the combustion intensity of pulverized coal decreases, and the temperature in the furnace decreases after reaching the peak value. In addition, the volume of the large furnace is bigger than that of the small one,

which reduces the average thermal load, gradually lowering the average temperature in it during the combustion process. Through comparison, it can be seen that the average temperature of the section is the highest at 38.69 meters. In case1 it's 1926K, in case2, 1912K, in case3, 1897K, in case4, 1894K, and in case5, 1879K, with a maximum difference of 47K.

4.3 Concentration Distribution

Figure 9 shows the variation of cross-sectional average O_2 concentration along furnace height at different recirculated flue gas distributions. With the increase of the bottom recirculated flue gas, the O_2 concentration in the large furnace and the lower part of the small one gradually increases. In the lower part of the small furnace, the O_2 concentration increases due to the increase in the flow of recirculating flue gas at the bottom; in the small furnace, the concentration of O_2 in the main combustion area fluctuates, this is due to the continuous introduction of pulverized coal and combustion air in the main combustion zone, and the strong combustion of pulverized coal causes the oxygen to be quickly consumed, which is consistent with the temperature distribution in the boiler; when in the large furnace, the O_2 concentration increases due to the injection of over-fire air, and the unburned pulverized coal from the small furnace reacts with the air, consuming some oxygen and causing the O_2 concentration to decrease.

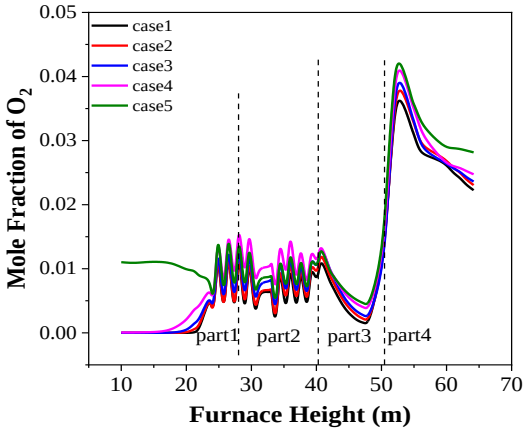

Figure 9 Area-weighted concentrations of O_2

Figure 10 shows the variation of CO average concentration with furnace height at different recirculated flue gas distribution ratios. We can see that the CO concentration increases first with the increase of furnace height, and reaches the highest concentration in the main combustion area. Then it decreases along the height, and increases again, and finally decreases along the height, reaching the lowest at the outlet. With the increase of the bottom recirculated flue gas, the CO concentration decreases significantly in the lower part of the furnace, and then decreases slightly in the upper part. The reason is that when the increase of the recirculation distribution ratio of bottom flue gas, a large amount of flue gas with high specific heat will be generated, which needs to absorb a large amount of heat. Therefore, it will slow down the combustion rate of pulverized coal, reduce its combustion intensity, increase the incomplete combustion degree of pulverized coal particles, and reduce the CO concentration. When the bottom recirculated flue gas ratio is 0, that is working condition case1, the highest CO concentration appears in the main combustion area at Y=29.19 m. However, when the ratio of the bottom recirculated flue gas gradually increases, the highest CO concentration also appears at Y=29.19 m, and the concentration gradually decreases. Obviously, due to the staged combustion of air, the small furnace is in an oxygen-poor environment, and the pulverized coal is not fully burned in the small furnace, which causes the local high CO concentration. With the increase of the recirculated flue gas ratio at the bottom, the amount of recirculated flue gas supplied in the small furnace increases, and the amount of oxygen entering the small furnace also increases, making the peak value of CO concentration gradually decrease.

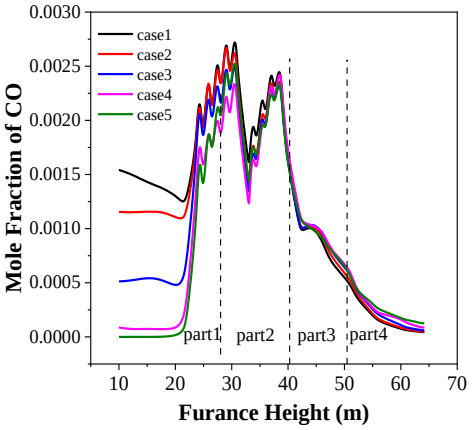

Figure 10 Area-weighted concentrations of CO

Figure 11 shows the NO concentration distribution on different sections in the furnace at different recirculated flue gas distribution ratios. It can be seen from the figure that the maximum NO concentration occurred in the small furnace. A large amount of pulverized coal particles are burned near the central area of the boiler, which releases volatile N, so NO concentration is relatively higher here. In the center of the boiler, combustion of pulverized coal particles also produced NO, resulting in an increase in NO concentration.

Through comparative observation, it can be seen more clearly that the NO emission concentration of S-CO_2 boilers with low recirculated flue gas distribution ratio at the bottom is uniformly reduced as a whole, and NO emissions are greatly improved. The overall decrease of O_2 concentration and the overall increase of CO_2 concentration in the furnace as well as the decrease of furnace temperature also play an important role in the reduction of fuel NO in the furnace, which is also the reason why NO emissions are greatly improved.

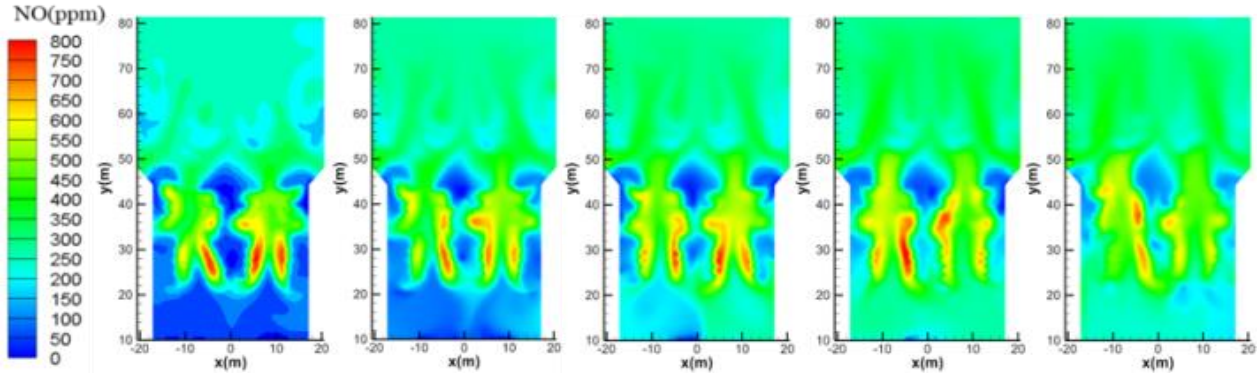

Case 1 Case 2 Case 3 Case 4 Case 5

(a) NO mole fraction distributions (Z=0m)

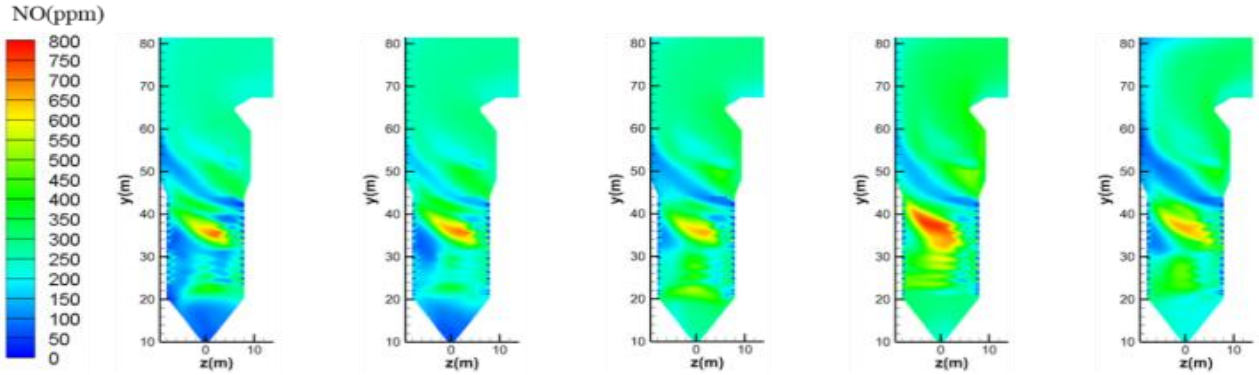

Case 1 Case 2 Case 3 Case 4 Case 5

(b) NO mole fraction distributions (X=3.4m)

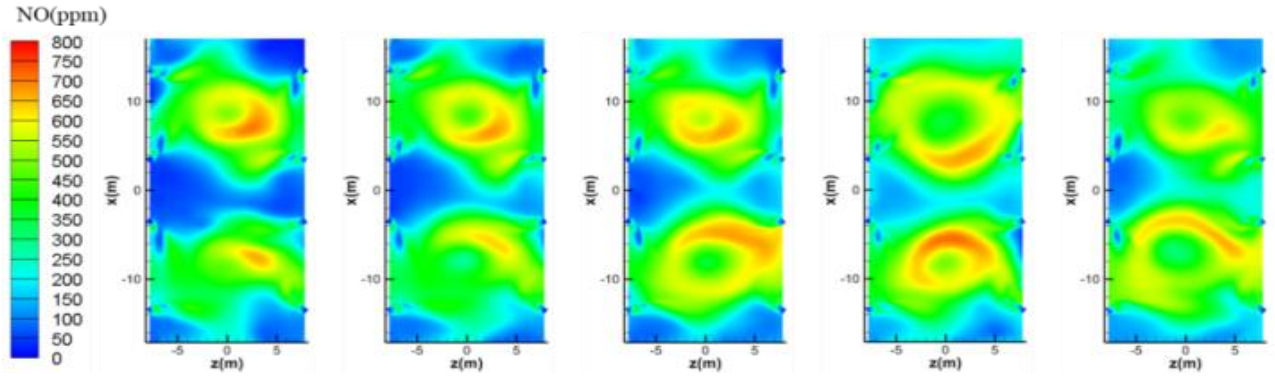

Case 1 Case 2 Case 3 Case 4 Case 5

(c) NO mole fraction distributions (Y=33.45m)

Figure 11 NO mole fraction distributions at different recirculated flue gas distribution ratios

With the increase of the bottom recirculated flue gas, the NO concentration shows a trend of increasing first and then decreasing. The NO concentration in the ash hopper is relatively low. Combined with O_2 concentration distribution, it can be found that with the increase of the circulation distribution ratio of the bottom flue gas, the nozzles are in an oxygen-poor state, which places the combustion reaction in an oxidizing atmosphere, thus reducing the NO emissions reduction effect. In the whole furnace, the concentration of NO at the outlet of the furnace is high due to the large excess air coefficient.

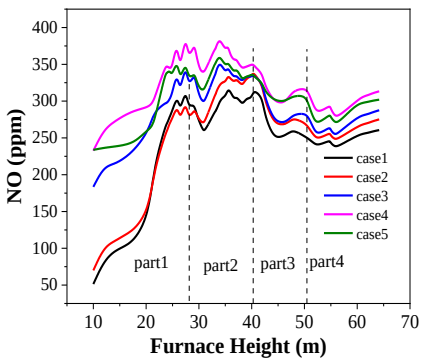

Figure 12 Area-weighted concentrations of NO

Figure 12 shows the variation of the average concentration of NO with the furnace height at different recirculated flue gas distribution ratios. We can see from the figure, the maximum concentration of NO is located in the furnace. It can be seen from the CO distribution (Figure10) that the NO distribution trend is opposite to that of CO. In places with higher CO concentration, the corresponding NO concentration is lower due to the strong reducing atmosphere. When the raise of the bottom flue gas recirculation distribution ratio, NO concentration first increases and then decreases. When the bottom flue gas recirculation distribution ratio was relatively high, NO concentration showed an upward trend, and NO production was the highest at case4. This is because under this condition, the recirculated flue gas brings in a part of oxygen, which increases the oxygen concentration in the main combustion area of the lower part of the staged combustion, resulting in the increase of NO production. However, when the recirculated flue gas distribution ratio continues to increase, the combustion in the furnace is unstable, the pulverized coal combustion conditions are not improved due to the decrease of the temperature in the furnace, resulting in the decrease of pulverized coal combustion rate and the decrease of the NO concentration.

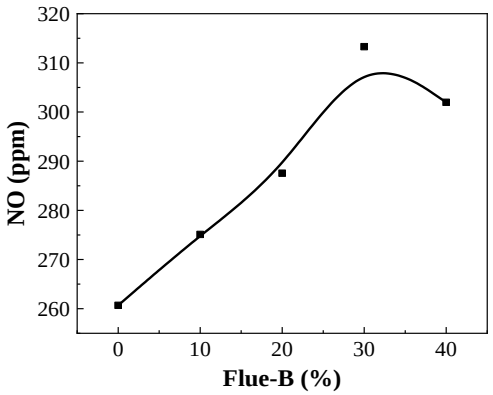

Figure 13 Area-weighted concentrations of NO at furnace outlet

Figure 13 shows the average concentration of outlet NO at different recirculated flue gas distribution ratios. We can see from the figure, the distribution ratio of recirculated flue gas has a great influence on the generation of combustion NO. When the upper, middle and lower distribution ratio is 55:45:0, the outlet NO concentration is 261ppm; When the distribution ratio is 50:40:10, the outlet NO concentration is 275ppm; When the ratio is 45:35:20, the concentration is 313ppm; When the ratio is 35:25:40, the concentration is 302ppm. Among them, when the distribution ratio of recirculated flue gas is 40:30:30, the outlet NO concentration is the highest, 313ppm. When the bottom flue gas circulation distribution ratio is 0-30%, the O_2 concentration at the bottom of the furnace increases, as the distribution ratio increases, promoting volatilization analysis and char combustion in the combustion process, which is beneficial to NO generation; When the bottom recirculated flue gas ratio is further increased, the combustion in the furnace is unstable and the furnace temperature decreases, which is not conducive to the combustion process and reduces NO generation to a certain extent.

4.4 Comparison of Ignition Temperature of Pulverized Coal

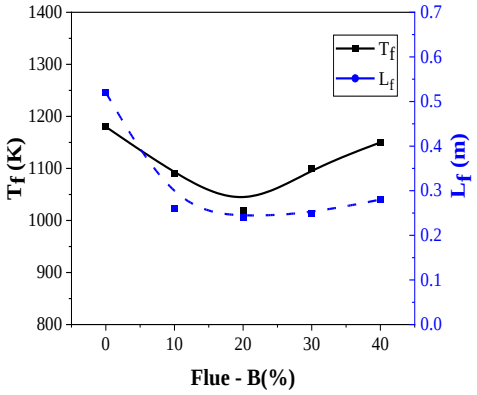

Figure 14 Comparison of ignition distance and ignition temperature at different bottom recirculated flue gas ratios

The pulverized coal carried by the primary air is sprayed into the furnace from the burner, the temperature of the coal particles increases quickly because of the heating of high gas temperature and radiation. When a certain temperature is reached, the pulverized coal starts to burn. The ignition distance L_f and ignition temperature T_f of pulverized coal are obtained along the injection direction Line-burner of the primary air nozzle PA-mid-1 in figure 1. Here, the ignition temperature T_f of the pulverized coal is obtained according to the method of literature [23]. For the temperature distribution along burner central line, calculate the first derivative of the temperature function, and the temperature corresponding to the maximum value of the derivative is the ignition temperature. Figure 14 gives the comparison of the ignition distance and ignition temperature of different recirculated flue gas distribution ratios. We can see from the Figure 14, with the increase of the bottom recirculated flue gas ratio, the ignition temperature and distance first decrease and then increase. The highest ignition temperature of case1 is 1180K, and the ignition distance is 0.52m. The lowest ignition temperature of case3 is 1020K, and the ignition distance is 0.24m. Compared with case1, the ignition temperature is reduced by 160K and the ignition distance is shortened by 0.28m.

5 Conclusion

In the paper, the numerical simulation software ANSYS FLUENT is used to carry out detailed numerical simulation on the generation characteristics of NO and combustion of a T-type 1000MW S-CO_2 coal boiler under the different condition of flue gas recirculation distribution ratios. The effects of recirculated flue gas distribution on the generation characteristics of NO and combustion

characteristics are investigated. The results show that:

(1) With the increase of the bottom recirculated flue gas ratio, the outlet NO concentration increases. When the bottom recirculated flue gas ratio is 30%, the outlet NO reaches the maximum, and then decreases if the bottom recirculated flue gas ratio continues to increase;

(2) With the increase of the bottom recirculated flue gas ratio, the average temperature in the lower furnace decreases, which is conducive to reducing the maximum temperature of the cooling wall;

(3) With the bottom recirculated flue gas ratio increases, the ignition distance and ignition temperature of pulverized coal decreases; when the bottom recirculated flue gas ratio is over 20%, the ignition temperature increases and the ignition distance increases slightly.

Author Contributions: Peipei Wang: Software, Data curation, Writing - original draft. Mingyan Gu: Writing - review & editing, Methodology. Yao Fang: Data curation. Boyu Jiang: Investigation. Mingming Wang: Investigation. Ping Chen: Writing - review & editing.

Conflict of Interest: The authors declare that they have no known competing financial interests or personal relationships that could have appeared to influence the work reported in this paper.

Acknowledgement: This paper is supported by the National Key R&D Program of China (2017YFB0601805).

References

[1] CAO Shuang, LIU Xiulong, ZHANG Ming,et al.Experimental study of organic Rankine cycle power generation system under various operating conditions[J]. CHEMICAL INDUSTRY AND ENGINEERING PROGRESS, 2018, 37(01):88-95.

[2] Si N, Zhao Z, Su S,et al. Exergy analysis of a 1000 MW double reheat ultra-supercritical power plant. Energy Conversion and Management 2017, 147:155- 65.

[3] Wu Y, Zhang M, Xie X,et al. Hot deformation characteristics and processing map analysis of a new designed nickel-based alloy for 700℃ A-USC power plant. Journal of Alloys & Compounds 2016, 656:119-31.

[4] XU Jinliang, LIU Chao, SUN Enhui,et al. Review and perspective of supercritical carbon dioxide power cycles[J]. THERMAL POWER GENERATION, 2020(10):1-10[2020-10-27].

[5] MOISSEYTSEV A, SIENICKI J J. Dynamic control analysis of the AFR-100 SMR SFR with a supercritical CO_2 cycle and dry air cooling Part I: Plant control optimization[C]//Proceedings of the 2018, 26th International Conference on Nuclear Engineering, London, England, July 22-26, 2018.

[6] MECHERI M, MOULLECLE Y L. Supercritical CO_2 Brayton cycles for coal-fired power plants[J]. Energy, 2016, 103: 758-771.

[7] Liao G, Liu L, Jiaqiang E,et al. Effects of technical progress on performance and application of supercritical carbon dioxide power cycle: A review[J]. Energy Conversion & Management, 2019, 199(Nov.):111986.1-111986.23.

[8] Milani D, Luu MT, McNaughton R,et al. Optimizing an advanced hybrid of solar-assisted supercritical CO_2 Brayton cycle: a vital transition for low-carbon power generation industry. Energy Conversion and Management 2017, 148:1317- 31.

[9] Halimi B, Suh K Y. Computational analysis of supercritical CO_2 Brayton cycle power conversion system for fusion reactor. Energy Conversion and Management 2012, 63:38–43.

[10] Le Moullec Y. Conceptual study of a high efficiency coal-fired power plant with CO_2 capture using a supercritical CO_2 Brayton cycle. Energy 2013, 49:32-46.

[11] Mecheri M, Le Moullec Y. Supercritical CO_2 Brayton cycles for coal-fired power plants. Energy 2016, 103:758-71.

[12] Zhang Y, Li H, Han W,et al. Improved design of supercritical CO_2 Brayton cycle for coal-fired power plant. Energy 2018, 155:1-14.

[13] Zhou J, Zhang C, Su S,et al. Exergy analysis of a 1000 MW single reheat supercritical CO_2 Brayton cycle coal-fired power plant. Energy Conversion and Management 2018, 173: 348-358.

[14] Yang Y, Bai W, Wang Y, et al. Coupled simulation of the combustion and fluid heating of a 300 MW supercritical CO_2 boiler. Applied Thermal Engineering 2017, 113:259-267.

[15] Cui Y, Zhong W, Xiang J,et al. Simulation on coal-fired supercritical CO_2 circulating fluidized bed boiler: Coupled combustion with heat transfer. Advanced Powder Technology, 2019, doi:10.1016/j.apt.2019.09.010.

[16] Bai W, Zhang Y, Yang Y,et al. 300 MW boiler design study for coal-fired supercritical CO_2 Brayton cycle. Applied Thermal Engineering 2018, 135:66–73.

[17] Liu X, Zhong W, Li P,et al. Design and performance analysis of coal-fired fluidized bed for supercritical CO_2 power cycle. Energy 2019, doi:10.1016/j.energy.2019.03.170.

[18] Jing Zhou, Meng Zhu, Sheng Su,et al. Numerical analysis and modified thermodynamic calculation methods for the furnace in the 1000MW supercritical CO_2 coal-fired boiler[J]. Energy,2020,212.

[19] Jing Zhou. Key issues and practical design for cooling wall of supercritical carbon dioxide coal-fired boiler[J]. Energy, 2019.

[20] Numerical calculation of flow and heat transfer: Study and discussion on some problems [M]. Science Press, 2015.

[21] Bo Yu, Jingfa Li, Dongliang Sun. Practical Training of Numerical Heat Transfer[M]. 2018.

[22] Zhou H, Mo G Y, Si D B,et al. Numerical Simulation of the NO_X Emissions in a 1000 MW Tangentially Fired Pulverized-Coal Boiler: Influence of the Multi-group Arrangement of the Separated over Fire Air[J]. Energy & Fuels, 2011, 25(5):2004-2012.

[23] Zhou J, Zhu M, Xu K,et al. Key issues and innovative double-tangential circular boiler configurations for the 1000 MW coal-fired supercritical carbon dioxide power plant[J]. Energy, 199.

Publisher: Viser Technology Pte. Ltd.

URL: www.viserdata.com

Add.:21 Woodlands Close, #08-18,

Primz Bizhub SINGAPORE (737854)